Search for Supersymmetry in the Hadronic Channel with Data from the CMS Experiment

Dissertation
zur Erlangung des Doktorgrades
des Department Physik
der Universität Hamburg

vorgelegt von Jan Thomsen
aus **Hamburg**

Hamburg 2012

Gutachter derDissertation:	Prof. Dr. Peter Schleper Dr. Isabell Melzer-Pellmann
Gutachter der Disputation:	Prof. Dr. Johannes Haller Dr. Thomas Schörner-Sadenius

Datum der Disputation: 27.4.2012

Vorsitzender des Prüfungsausschusses:	Dr. Georg Steinbrück
Vorsitzender des Promotionsausschusses:	Prof. Dr. Peter Hauschild
Dekan des Fachbereichs Physik:	Prof. Dr. Heinrich Graener

Abstract

The CMS experiment at the LHC has taken data from proton-proton collisions at the center of mass energy of 7 TeV. This data is used to search for new physics with an analysis based on large missing transvere energy and high energetic jets. The Standard Model background is estimated with high precision using data-driven estimation methods. The prediction of the background from $t\bar{t}$ and W + jet events with non-identified electrons and muons from the W-decay is descussed in detail in this analysis.

No excess over the Standard Model expectation could be found in the data. The results are interpreted with the CL_S-method within the constraint minimal supersymmetric Standard Model (cMSSM). A lower limit on the squark mass of 1100 GeV can be set.

Zusammenfassung

Proton-Proton-Kollisionsdaten mit einer Schwerpunktsenergie von 7 TeV wurden vom CMS-Experiment am LHC aufgenommen. Mit Hilfe dieser Daten wird nach neuer Physik gesucht. Die Suche basiert auf einem starken Ungleichgewicht der gemessenen Impulse und hochenergetischen Jets. Der Standard Model Untergrund wird mit hoher präzisiondurch aus Daten bestimmt. Die Methode zur vorhersage von $t\bar{t}$ und W + jet Ereignissen bei denen das Elektron oder Muon aus dem W-Zerfall nich identifiziert werden, wird detailiert diskutiert.

Es gibt in den Daten keinen Überschuss gegenüber der Standard Modell Erwartung. Die Resultate werden mit der CL_S-Methode in dem constraint minimal supersymmetric Standard Modell (cMSSM) interpretiert. Squarkmassen unter 1100 GeV können durch diese Analyse in diesem Modell ausgeschlossen werden.

Contents

1

Introduction

The Standard Model (SM) of particle physics has been extremely successful in describing the data of nearly all experiments over a huge energy range from a fraction of an electron Volt (eV) up to the TeV scale. It has also shown a large predictive power. Most remarkable is the experimental confirmation of the predicted W and Z vector bosons in the early 1980s. Precision measurements at LEP [1] at CERN have tested the electroweak theory to the 10^{-3} level, in some cases even much more precisely. With the finding of the predicted top-quark in 1995 all SM particles are experimentally confirmed except for the higgs boson. The search for this particle is one of the main tasks of the two multi-purpose experiments on the Large Hadron Collider (LHC) [2], ATLAS [3] and CMS [4].

Apart from the missing higgs particle, there are other shortcomings of the SM. Gravity is not included in this model and, although several experiments have shown that there is a large amount of cold dark matter in the universe [5] [6], there is no candidate for this within the SM. The SM also cannot explain the large difference between the amount of matter and anti-matter in the universe. There are other, more subtle reasons to believe that the SM is only a low energy approximation of a more fundamental theory. The number of free parameters in the SM is quite large and there is no understanding why there are exactly three generations of particles, why the charge of an electron exactly equals the charge of the proton or why the masses of neutrinos are of much smaller values than other particles. To keep the higgs mass reasonably small a high degree of fine-tuning of the parameters of the SM would be necessary.

There are several theories available that can solve some of these shortcomings - usually by introducing new particles. The most promising extension of the SM is supersymmetry (SUSY) that relates fermions - the matter particles in the SM - with boson - the force carriers in the SM. This extension introduces a supersymmetric partner to each SM particle and therefore doubles the amount of particles. As no SUSY particles with the mass of their SM partners have been found, SUSY has to be a broken symmetry. This extension of the SM allows to solve most of the shortcomings of the SM, especially if the masses of the superpartners are at the TeV scale. As the LHC has taken data for more than a year with a center of mass energy of 7 TeV, it is of great interest to look for SUSY particles within the LHC data. In this thesis the minimal supergravity (mSUGRA) framework is studied, where the SUSY breaking is mediated through gravity. Some basic assumptions motivated by Grand Unification Theories are made in the mSUGRA framework that reduce the large amount of free parameters to just 5 parameters in addition to the parameters of the SM.

An all-hadronic analysis on the data taken by the CMS experiment is presented that looks for SUSY particles. This search is particlularly difficult because the cross section of SUSY prosseses is very small for larger SUSY masses, leading to a small signal to background ratio. There are several background processes to the signature of signal events. To be as sensitive as possible the uncertainties on these backgrounds need to be reduced. In this thesis the background from $t\bar{t}$ and W + jet events with an electron or muon from the W-decay that is not identified by the experiment, is predicted from data. This is one of the four major background processes. The other being QCD multijet events, events with a Z-boson that decays into neutrinos and $t\bar{t}$ and W + jet events, where the W-boson decays into a tau-lepton that decays hadronically. As no excess over the SM prediction can be observed, it is only possible to set exclusion limits on the SUSY parameter space. This analysis is able to set the world's best direct limits on the mSUGRA parameter space, excluding a huge fraction of the so far most promising regions.

In the second and third chapter the SM and SUSY is reviewed with a discussion of the shortcomings of the SM and how SUSY solves these problems. A focus is set on production and decay channels at accelerators. In chapter four

the experiment is discussed and the reconstruction of physics objects with a focus on jet reconstruction is discussed in chapter five. The analysis strategy is presented in chapter six, followed by a discussion of the data driven background estimation in chapter seven. In chapter eight all data-driven background predictions are combined and a limit on the mSUGRA parameter space is set, before summarising the analysis in chapter nine.

2

The Standard Model

The modern theory of particle physics, known as the Standard Model (SM), describes all elementary particles and forces - except gravity - that we know about. It is extremely successful in its predictions and has been tested with very high precision at various experiments at particle accelerators such as the LEP [1], the Tevtron [7] and the LHC [2]. There are however strong indications that the SM is only a low energy approximation of a more fundamental theory. The SM can be divided into three parts: Fermions as fundamental matter particles, bosons as carrier of the fundamental forces and the Higgs mechanism, which allows particles to gather mass. The review and formulas presented here is based on [8] [9] [10] and follows closely my previous work in [11].

2.1 The Fermion Sector

This part of the SM describes all spin 1/2 particles, called fermions. Each fundamental force within the SM couples to a charge. These charges define in which interactions the fermions participate and how strong the couplings to these forces are. All fermions take part in the weak interaction [1] and only the neutrinos do not carry an electrical charge. If fermions interact strongly, they are called quarks and carry a charge called colour. Fermions that are colour-neutral are called leptons. The nature of the strong force, which will be discussed later, is

[1] As explained later the weak force couples only to left-handed particles and right-handed anti-particles.

the reason why quarks always form bound, colour-neutral states called hadrons, while leptons are observed as free particles. If these hadrons consist of a quark and an anti-quark they are called mesons. Hadrons consisting of three quarks are called baryons such as the long lived neutron and the stable proton, which has an experimental lower limit on its lifetime of $2.1 \cdot 10^{29}$ years [12].

There are three generations of fermions. Corresponding to each fermion in the first generation there are two particles in the second and third generation with the same quantum numbers but considerably higher masses. Neutrinos in higher generations do not necessarily have higher masses. To every fermion there is also an antiparticle with the same mass, lifetime and spin, but opposite charge.

Fermions are grouped into left-handed doublets and right-handed singlets with Chirality[1] -1 and 1 respectively. An overview of all fermions together with the bosons discussed in the next section is given in Tab. 2.1.

2.2 The Boson Sector

All forces in the SM are described by renormalisable[2] gauge field theories. These forces are conveyed by spin 1 particles, which are called gauge bosons. The electromagnetic and weak forces are described by the electroweak theory, based on a $U(1)_Y$ x $SU(2)_L$ Lie group. Strong interactions are described by Quantum Chromodynamics, based on a $SU(3)_C$ symmetry group. The concept of gauge theories is explained exemplary on Quantum Electrodynamics (QED) $U(1)_{EM}$.

2.2.1 Quantum Electrodynamics (QED)

In quantum field theories a fermion and its anti-particle are described by the spinor fields Ψ and $\overline{\Psi}$. The Lagrangian of a free particle is:

[1] A particle has positive helicity if the spin measured in the direction of the momentum is positive. Chirality is a Lorenz invariant definition that is identical to helicity in the relativistic approximation, i.e. the mass energy of a particle is small compared to its kinetic energy.

[2] Infinities in the calculation of higher order diagrams are absorbed into constants such as the coupling constants. By this the remainder of the equations remain finite, but the constants become dependent on the energy at which they are probed and are called running constants.

$$L_{Dirac} = \overline{\Psi} i\gamma^\mu \partial_\mu \Psi - m\overline{\Psi}\Psi, \tag{2.1}$$

where the first part describes the kinetic energy and the second part corresponds to its mass. Gauge interactions between fermions are introduced by requiring local gauge invariance. Noether's Theorem [13] states that invariance under a global $U(1)$ phase transition of the form:

$$\Psi \to \Psi e^{-i\alpha} \tag{2.2}$$

leads to conservation of the charge e and the current J^μ:

$$J^\mu = e\overline{\Psi}\gamma^\mu\Psi. \tag{2.3}$$

Local gauge transformations depend on the space-time location x and have the form:

$$\Psi \to \Psi e^{-i\alpha(x)}. \tag{2.4}$$

The Lagrangian (2.1) is not invariant under such a transformation. To restore this invariance, a gauge field A_μ is introduced and the partial derivative ∂_μ is substituted by the covariant derivative D_μ, with

$$D_\mu = \partial_\mu - ieA_\mu. \tag{2.5}$$

If A_μ transforms like:

$$A'_\mu = A_\mu - \frac{1}{e}\partial_\mu \alpha(x), \tag{2.6}$$

the Lagrangian becomes local gauge invariant and has the form:

$$L = \overline{\Psi} i\gamma^\mu \partial_\mu \Psi - m\overline{\Psi}\Psi + e\overline{\Psi} i\gamma^\mu \Psi A_\mu. \tag{2.7}$$

The last term is the interaction term between the Photon A_μ and the fermion. It has the form expected from the correspondence principle replacing the classical current $J = (\rho, \vec{j})$ by the conserved current J^μ and field $A = (\Phi, \vec{A})$ by A_μ.
To get the complete Lagrangian the kinetic energy of the photon, i.e. the energy

stored in the potential of its electromagnetic field, has to be included. With the antisymmetric force tensor $F_{\mu\nu} = \partial_\mu A_\nu - \partial_\nu A_\mu$ the full EM-Lagrangian can be written as:

$$L = \overline{\Psi} i\gamma^\mu \partial_\mu \Psi - m\overline{\Psi}\Psi + e\overline{\Psi} i\gamma^\mu \Psi A_\mu - \frac{1}{4} F^{\mu\nu} F_{\mu\nu}. \tag{2.8}$$

There can be no mass term for the photon of the type $mA_\mu A^\mu$, because it would not be gauge invariant. Thus it remains massless.

2.2.2 Quantum Chromodynamics (QCD)

In the 1970s experimental data hinted to a degree of freedom in the quark sector that had not been known before. The prediction of the measurement of the ratio $R = \frac{e^+e^- \rightarrow \text{ hadrons}}{e^+e^- \rightarrow \mu^+\mu^-}$ for example did not agree with data by a factor of three. This could be accounted for by introducing the color charge. This charge of the strong interaction is similar to the familiar electric charge only that there are three different color states: red, green and blue[1]. This leads to the choice of a $SU(3)_C$ gauge group, where the index C stands for colour and is introduced to avoid confusions with the flavor $SU(3)$ group that gives the structure to the bound quark states. The concept of QCD is the same as in QED, but the more complicated structure of $SU(3)_C$ leads to some qualitatively different phenomenology.

Since there are eight generators in this group, there are also eight gauge bosons. These are called gluons and carry a color charge themselves due to the non-abelian structure of $SU(3)_C$. By this, additional gauge boson self-interactions with 3-gluon and 4-gluon vertices are possible. As gluons are bosons and carry a charge and anti-charge, the force is not shielded as in QED where the vacuum polarisation from electron-positron pairs reduces the force with distance. Instead the anti-shielding in QCD leads to the increasing strength of the strong force with distance and is the reason why quarks always form bound states. The residual

[1]The names were given, because these colours behave similar when they are added, e.g. together they give a neutral "white"

force[1] between hadrons keep the nuclei together, but the strength of this residual force decreases rapidly with distance.

2.2.3 Electroweak Theory

Experiment [14] showed that the weak force couples only to left-handed particles and right-handed antiparticles. Therefore, the weak current has the form:

$$J^{\mu}_{weak} W_{\mu}, \tag{2.9}$$

with

$$J^{\mu}_{weak} = \overline{\Psi}_{a,L} \gamma^{\mu} \Psi_{b,L} = 1/2 \overline{\Psi}_{a} (\gamma^{\mu} - \gamma^{\mu} \gamma^{5}) \Psi_{b}. \tag{2.10}$$

The term in brackets has the form vector - axial vector (V-A) and is responsible for the parity[2] violation.

Experiments show that the bosons involved in weak interactions can carry an electromagnetic charge leading to the suggestion that the electromagnetic and the weak force are related and that they can be formulated in a combined way.

Weak interactions can be described by a gauge theory based on $SU(2)$ and as the interaction couples only to left-handed particles it is written $SU(2)_L$. $SU(2)$ has three generators and therefore three gauge bosons W_{1-3}. To include electrodynamics a larger group is needed and the simplest expansion with respect to the number of gauge bosons is $SU(2)_L$ x $U(1)_Y$. The hypercharge is defined as:

$$Y = 2(Q - I_3), \tag{2.11}$$

with I_3 being the z-component of the weak isospin charge:

$$I_i = \frac{1}{2} \tau_i, \tag{2.12}$$

and τ_i being the Pauli matrices. Y is the generator of $U(1)_Y$ instead of the electric charge in $U(1)_{EM}$.

The covariant derivative in this theory is:

[1] This effect is quite similar to the Van der Waals-force in electromagnetism that is due to the polarization of each molecule.

[2] Parity is the operation of space inversion.

$$D_\mu = \partial_\mu - ig_1 \frac{Y}{2} B_\mu - ig_2 T_i W_{i,\mu}, \tag{2.13}$$

with $T_i = \frac{\tau_i}{2}$ for left-handed particles and $T_i = 0$ for right-handed particles. Since the Pauli matrices do not commutate, there is a cross-product in the kinetic energy term of the SU(2)-bosons leading to three- and four-boson vertices similar to QCD. However, there is no confinement in electroweak interaction. The fields $W_{1,2}$ mix to form the charged $W^\pm$ gauge bosons. They correspond to the fields $W^\pm = \frac{W_1 \pm iW_2}{\sqrt{2}}$. The photon and the Z-boson are orthogonal linear combinations of the fields B and W_3. The coefficients can be described as a sine and a cosine of an angle of rotation. This angle is called the Weinberg angle ϑ_W and is measured to be about $28°$[1] [15].

$$A_\mu = \cos\vartheta_W B_\mu + \sin\vartheta_W W_{3,\mu} \tag{2.14}$$

$$Z_\mu = -\sin\vartheta_W B_\mu + \cos\vartheta_W W_{3,\mu} \tag{2.15}$$

The photon does not couple to the neutrino and the coupling to the electromagnetic field is e. This leads to:

$$g_1 = \frac{e}{\cos\vartheta_W} \tag{2.16}$$

$$g_2 = \frac{e}{\sin\vartheta_W} \tag{2.17}$$

The coupling constants of the weak interaction are larger than for electrodynamics. The reason why weak interactions have a small cross-section and a short range is the mass of the weak gauge bosons. This mass is experimentally confirmed, even though a simple mass term would not be gauge invariant and is not present in the SM Lagragian. The Higgs mechanism through which gauge invariant terms for boson masses become possible is subject of the next chapter.

The left-handed nature of the weak force has important implications on the kinematics in proton-proton events with a $W^\pm$-boson at the LHC. Not only are W^+ and W^- preferably polarised left-handed along their flight direction, but also

[1] at the Z-mass. It varies with energy.

are the leptons from a W^--decay preferably emitted in direction of flight, while it is the opposite direction for leptons from W^+-decays [16].

2.3 Electroweak Symmetry Breaking

As stated in the last chapter, there has to be a mechanism that gives masses to the vector bosons without destroying gauge invariance. This Higgs-mechanism breaks the $SU_L(2)$ x $U_Y(1)$ symmetry in such a way, that the $U_{EM}(1)$ symmetry remains unbroken and the photon remains massless. $SU(3)_C$ also remains unbroken.

Just as in ferromagnetism, where the rotation symmetry breaks below the Curie-temperature, the Lagrangian possesses a symmetry that is not possessed by the minimal of the potential. The simplest way to produce such a spontaneous symmetry breaking is to introduce a Higgs field, that is a complex scalar $SU(2)_L$ doublet:

$$\Phi = \begin{pmatrix} \Phi^+ \\ \Phi^0 \end{pmatrix}, \text{ with } Y = +1. \tag{2.18}$$

The electric charges, indicated by the indices, follow from the assigned hypercharge and the weak isospin charge. The globally gauge invariant Lagrangian for Φ is given by:

$$L_\Phi = (\partial^\mu \Phi)^\dagger (\partial_\mu \Phi) - \mu^2 \Phi^\dagger \Phi - \lambda (\Phi^\dagger \Phi)^2, \lambda > 0. \tag{2.19}$$

With the last two terms representing the potential, that is called "Mexican hat" potential when $\mu^2 < 0$, because of its form. With $\mu^2 > 0$ the potential would have an absolute minimum at $\Phi^+ = \Phi^0 = 0$ and therefore cannot break symmetry. In the interesting case with $\mu^2 < 0$ the lowest energy state, i.e. the vacuum expectation value, is $\frac{v}{\sqrt{2}}$, with $v = \sqrt{-\mu^2/\lambda}$. Now, the Lagrangian (2.21) has to be made locally gauge invariant under electroweak transformations by exchanging ∂_μ by $D_\mu = \partial_\mu - ig_1 \frac{Y}{2} B_\mu - ig_2 (\frac{\vec{\tau}}{2} \vec{W})_\mu$. The extra terms in the covariant derivative operator lead not only to cubic and quartic interaction terms between the Higgs and the gauge fields and between the Higgs itselves, but also to new mass terms. These masses are given by:

$$\frac{1}{4}v^2 g_2^2 W^{+\dagger\mu} W_\mu^{-\dagger} + \frac{1}{8}v^2(g_1 B^\mu - g_2 W_3^\mu)(g_1 B_\mu - g_2 W_{3\mu}) \tag{2.20}$$

Changing the B and W_3 fields to Z and A yields:

$$M_W = \frac{1}{2}v g_2,\ M_Z = \frac{1}{2}v\sqrt{g_1^2 + g_2^2} \quad \text{and} \quad M_A = 0. \tag{2.21}$$

The ratio between the W and the Z boson masses given by:

$$M_W = M_Z \cos\theta_W \tag{2.22}$$

This has been confirmed experimentally [17]. The Higgs mass is given by:

$$M_H = \sqrt{-2\mu^2}, \tag{2.23}$$

and is not predicted by the SM as μ is a free parameter. The Higgs particle is the only particle in the SM that has not yet been experimentally observed with a sufficient confidence level, but experiments at LEP excluded the Higgs for masses below 114 GeV and CMS has recently extended the excluded Higgs masses between 127 GeV and 600 GeV [18]. Higgs masses above 600 GeV are disfavoured by fits to the electroweak precision data, so that the Higgs is expected to have a mass between 114 GeV and 128 GeV, if it exits. CMS, ATLAS and the Tevatron see an excess of events in their data hinting towards a Higgs mass around 124 GeV, but the excess is not yet strong enough to claim a discovery.

The Higgs mechanism can also produce fermion masses. A simple Dirac mass term $m\overline{\Psi}\Psi$ can be transformed in the following way:

$$m\overline{\Psi}\Psi = m\overline{\Psi}(P_R + P_L)\Psi = m\overline{\Psi}P_R^2\Psi + m\overline{\Psi}P_L^2\Psi = m\overline{\Psi_L}\Psi_R + m\overline{\Psi_R}\Psi_L \tag{2.24}$$

Ψ_L is a doublet, while Ψ_R is a singlet under $SU(2)$, they cannot be combined to produce an invariant mass term. Using the Higgs doublet, the term can be modified to:

$$L_{\text{Yuk}} = \lambda_\Psi[(\overline{\Psi_L}\Phi)\Psi_R + \overline{\Psi_R}(\Phi^\dagger\Psi_L)], \tag{2.25}$$

with λ_Ψ being a coupling constant. Here, the inner parenthesis is a product of two isospinors. Doing this for all fermions of the standard model gives:

$$L_{\text{Yuk}} = \lambda_e \overline{\Psi_L} \Phi e_R + \lambda_u \overline{q_L} \overline{\Phi} u_R + \lambda_d \overline{q_L} \Phi d_R + h.c. + 2^{\text{nd}} \quad \text{and} \quad 3^{\text{rd}} \quad \text{Families} \tag{2.26}$$

where

$$\Psi_L = \begin{pmatrix} \nu_e \\ e_L \end{pmatrix} q_L = \begin{pmatrix} u_L \\ d_L \end{pmatrix} \Phi = \begin{pmatrix} \Phi^+ \\ \Phi^0 \end{pmatrix} = \begin{pmatrix} 0 \\ v + H(x) \end{pmatrix} \tag{2.27}$$

$$\overline{\Phi} = i\sigma_2 \Phi^* = \begin{pmatrix} \Phi^{0*} \\ -\Phi^0 \end{pmatrix}. \tag{2.28}$$

This creates the mass term $m_a = \lambda_a \frac{v}{\sqrt{(2)}}$, where a can be any charged lepton or quark. The couplings to the Higgs field are proportional to $\frac{\lambda_a}{\sqrt{2}} = \frac{m_a}{v}$. These Yukawa couplings do not arise from gauge-symmetry requirements. They describe the mass generation in a convenient way, but do not explain the values of masses and why there is such a large difference between them.

Neutrino masses are not discussed in this thesis. If neutrinos are dirac-particles and not majorana-particles, which are their own antiparticles, the mass term can be constructed in the same way as for the other fermions.

2.4 Particle Content of the Standard Model

A summary of all confirmed SM particles and their quantum numbers is given in Tab.(1.1). The Higgs boson is not included as it still needs experimental proof. One of the main goals of the Large Hadron Collider (LHC), which will be discussed in detail in chapter 4.2, is to find the Higgs boson to complete the finding of the SM particles.

All fundamental particles are considered point like.

2.5 Success and Problems of the Standard Model

The SM of particle physics described in this chapter has been extremely successful in describing a huge amount of data over an energy range from a fraction of an

Fermions (Spin=1/2)						
	Generation			**Quantum number**		
	I	II	III	Y	Q	I_3
Leptons	$\begin{pmatrix} \nu_e \\ e \end{pmatrix}_L$	$\begin{pmatrix} \nu_\mu \\ \mu \end{pmatrix}_L$	$\begin{pmatrix} \nu_\tau \\ \tau \end{pmatrix}_L$	$\begin{pmatrix} -1 \\ -1 \end{pmatrix}$	$\begin{pmatrix} 0 \\ -1 \end{pmatrix}$	$\begin{pmatrix} \frac{1}{2} \\ -\frac{1}{2} \end{pmatrix}$
	e_R	μ_R	τ_R	-2	-1	0
Quarks	$\begin{pmatrix} u \\ d' \end{pmatrix}_L$	$\begin{pmatrix} c \\ s' \end{pmatrix}_L$	$\begin{pmatrix} t \\ b' \end{pmatrix}_L$	$\begin{pmatrix} \frac{1}{3} \\ \frac{1}{3} \end{pmatrix}$	$\begin{pmatrix} \frac{2}{3} \\ -\frac{1}{3} \end{pmatrix}$	$\begin{pmatrix} \frac{1}{2} \\ -\frac{1}{2} \end{pmatrix}$
	u_R	c_R	t_R	$\frac{4}{3}$	$\frac{2}{3}$	0
	d'_R	s'_R	b'_R	$-\frac{2}{3}$	$-\frac{1}{3}$	0

Gauge Bosons (Spin=1)				
	Interaction	**Quantum number**		
electromagnetic	Gamma (γ)	0	0	0
weak	Z^0	0	0	0
weak	$W^\pm$	0	± 1	± 1
strong	$g_{1\ldots8}$	0	0	0

Table 2.1: The particles of the SM. The Higgs boson (spin=0) is not included as its existence is still not verified in experiment.

electron volt to about 1 TeV. It has also made a number of predictions that have been confirmed experimentally. The discovery of W and Z bosons in the early 1980s for example confirmed the electroweak theory in a spectacular way.

Precision measurements at the LEP collider at CERN have tested the electroweak theory to the 10^{-3} level, in some cases like the magnetic moment of the electron the tests are even more precise by many orders of magnitude.

There are some obvious shortcomings of the SM, though. Gravity is not included in this theory and fermion masses are not predicted by the SM. Neutrino masses are set to zero although neutrino oscillations [19] strongly suggest that this is not the case. A variety of observations in cosmology strongly suggest the existence of cold dark matter in the universe [5] [6] for which there is no candidate in the SM. While there are mechanisms in the SM that can lead to an asymmetry between matter and anti-matter these are not strong enough to explain the large asymmetry observed.

There are also aesthetic considerations that the SM is only a "low" energy approximation of a more fundamental theory: The number of free parameters, most of them masses and mixing angles, is quite large. There is no understanding why there are exactly three generations in the SM. There is no reason within the SM why the magnitude of the charge of an electron is exactly the same as the charge of the proton. The three gauge coupling constants vary with energy (running coupling) and come quite close at the GUT scale around 10^{16} GeV (GUT stands for Grand Unified Theory), but they do not meet in one point if only SM particles are taken into account. This would be desirable for constructing a GUT theory, which could explain the equality of charges.

A very interesting problem of the SM is the Hierarchy Problem, because it hints to the scale where some new physics should reveal itself. The radiative corrections lead to corrections to all non-zero masses. Usually these corrections increase logarithmic, but for the Higgs boson mass the corrections are much more severe. The corrections due to fermion and boson loops to the Higgs mass are in leading order [20, 21]

$$(\delta m_H^2)_{Fermion} = \frac{\lambda_F^2}{16\pi^2}(-2\Lambda^2 + 6m_F^2 \ln\frac{\Lambda}{m_F} + ...) \tag{2.29}$$

$$(\delta m_H^2)_{Boson} = \frac{\lambda_S}{16\pi^2}(\Lambda^2 - 2m_S^2 \ln \frac{\Lambda}{m_S} + ...) \tag{2.30}$$

Λ is the cut-off parameter, which can be thought of as the energy up to which the theory is still valid. In the SM the correction due to fermion loops clearly dominate. Taking the cut-off parameter as the GUT scale or the Planck scale [1], where gravitational effects become important, this would give corrections many times larger than the Higgs mass itself. It is generally possible to limit these corrections within the standard model by other terms, but the parameters have to be "fine-tuned" to an extremely high degree. In order to bring Λ to the GUT scale the Lagrangian mass parameter m_H^2 needs to be fine-tuned to one part of $10^{34} \approx \left(\frac{m_W}{m_\Lambda}\right)^2$. This does certainly not seem to be a natural approach.

[1]The Planck scale is about 10^{19} GeV. This value assumes that the laws and dependencies of gravity are still valid on short distances.

3

Supersymmetry

Supersymmetry (SUSY) is a symmetry between bosons and fermions. In supersymmetric models every SM particle has a partner which differs in spin by 1/2. In this chapter the concept of supersymmetry is described. As supersymmetry solves several problems of the SM, it is one of the most favoured physics models beyond the SM. The chapter starts with explaining these solutions, motivating the assumption of many hypothetical particles searched for in the analysis presented in this thesis. The review and formulas presented here is based on [22] [21] and follows closely my previous work in [11].

3.1 Concept

Supersymmetry relates bosons and fermions with each other. A fermion can be transformed into a boson and a boson into a fermion under the supersymmetry transformation operator Q. These spinors fulfill the anticommutation relation:

$$\left\{Q_a, \overline{Q_b}\right\} = 2(\gamma^{\mu}_{ab})P_{\mu}, \tag{3.1}$$

where P_μ is the Poincaré group generator of spacetime translations.

Generators with this anticommutation relation can be combined with the Poincaré symmetry, adding an exception to the Coleman-Mandula theorem from the 1960s that stated that this is only possible by a direct product.

The operator P^2 is still a Casimir operator, which means that it commutes with all the generators of the group. Therefore, all particles in one supermultiplet,

i.e. two particles that are related by a supersymmetry transformation, have the same mass. They also have to have the same electric and color charge. The square of the Pauli-Lubanski pseudovector W^2, that corresponds to the spin the same way as P^2 to the mass is no longer a Casimir invariant. The spin of particles in one supermultiplet can therefore differ.

The fact, that two superpartners have the same mass is disturbing, though, as there is no integer spin particle with the same mass and charge as for example the electron. Therefore, supersymmetry must be a broken symmetry. A breaking mechanism will be discussed in the next section.

As left- and right-handed fermions have different gauge transformations, there are two scalars for each fermion called sfermions. These sfermions form together with the SM fermions chiral supermultiplets. It seems strange to give sfermions a chirality, since they do not have spin. It refers to "the partner to a left- or right-handed fermion". The superpartner of the SM gauge bosons are spin 1/2 "gauginos" that have also two helicity states. These gauge-bosons and gauginos form a gauge or vector supermultiplet.

In the SM, baryon- and lepton-numbers are conserved. In supersymmetric theories it is possible to construct renormalisable operators that do not conserve these numbers, but are still consistent with SM gauge symmetries and supersymmetry. However, terms that violate lepton- and baryon-conservation cannot both be large to comply with the experimental lower limit on the lifetime of the proton of more than $2.1 \cdot 10^{29}$ years [12]. With the introduction of R-parity conservation these terms are assumed to be zero. R-parity is defined by:

$$R = (-1)^{3(B-L)+2S}, \tag{3.2}$$

where B and L are baryon- and lepton-numbers, respectively, and S is the spin. All SM particles have positive R-parity, while their superpartners have negative R-parity. Therefore, there can be no mixing between SM particles and sparticles. Furthermore, the lightest supersymmetric particle (LSP) has to be stable, if R is conserved. This is assumed for this analysis.

3.2 Solutions to Standard Model Problems

In the last chapter the problem of the large corrections to the Higgs mass was shown in Eq. 2.29 and Eq. 2.30. If there are two superpartners to each fermion - one for the left- and one for the right-chiral state - with $\lambda_F^2 = \lambda_S$ the quadratic dependence on the cut-off parameter Λ vanishes leaving only a logarithmic dependence:

$$\delta m_H^2 \propto (m_S^2 - m_F^2) \ln \frac{\Lambda}{m} \tag{3.3}$$

This reduces the corrections to a logarithmic dependence. Still the mass-difference between the supersymmetric partners enter the calculation leading to the suggestion that these particles should not be very heavy [1]. This makes searches for supersymmetry at the LHC with a current center of mass energy of 7 TeV especially interesting.

The large amount of cold dark matter in the universe can not be accounted for within the SM. In most SUSY models R-parity conservation is assumed, which implies that supersymmetric particles can only decay into SM particles plus an odd number of supersymmetric particles. Therefore, the lightest supersymmetric particle (LSP) is stable and if it is only weakly interacting it is a natural dark matter candidate.

The number of baryons in the universe dominates over that of anti-baryons. Baryon asymmetry implies CP-violation. Although CP violation has been proven to exist within the SM, the size of this effect is much too small to account for the asymmetry. In supersymmetric models there are several possible interactions that can lead to CP violation and therefore can explain the baryon asymmetry.

In the SM infinities in higher order corrections are included in the constants such as the gauge couplings, leading to an energy dependence. This is called renormalisation. With increasing energy the three gauge couplings come close to each other, but only if supersymmetric particles at the TeV scale are included in the higher order calculations they meet at the GUT scale[2], as can be seen in

[1] This is especially true for the stop which has a large yukawa-coupling

[2] The scale depends on the physics at shorter distances not yet explored by experiments. Assuming only a supersymmetric SM this value is around 10^{16} GeV.

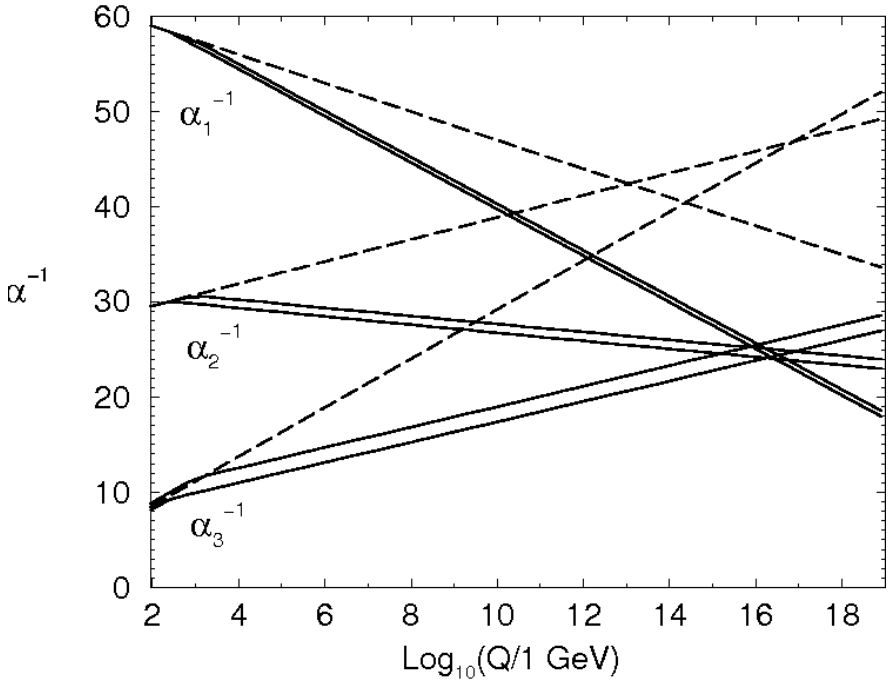

Figure 3.1: *Renormalisation group evolution of the inverse gauge couplings $\alpha_i^{-1}(Q)$ in the Standard Model (dashed lines) and the MSSM(solid lines). In the MSSM case, the sparticle mass thresholds are varied between 250 GeV and 1 TeV, and $\alpha_3(m_Z)$ between 0.113 and 0.123. Two-loop effects are included. [21] [23]*

Fig. 3.1. While there is no strong argument why they need to meet this hints to a more fundamental theory with less free parameters.

The most obvious shortcoming of the SM is the failure to include gravity. If supersymmetry is a local symmetry, the associated massless gauge field is the gravitino, the superpartner of the graviton. SUSY therefore provides a natural framework in which to unify gravity with the strong, weak and electromagnetic force. While there are still non-renormalisable parts in the supergravity Lagrangian that are beyond the scope of this thesis, it certainly justifies to interpret searches for SUSY particles within the framework of supergravity models.

3.3 Minimal Supersymmetric Model

There is a large amount of possible supersymmetric theories. All models considered in this analysis are based on the Minimal Supersymmetric Model (MSSM), which is a direct supersymmetrisation of the SM, except for the facts that a second Higgs doublet field has to be introduced and that R-parity is conserved. It is "minimal" with respect to the amount of new, yet undiscovered, (s)particles.

The SM Higgs doublet is replaced by two doublets of left-chiral superfields:

$$\Phi = \begin{pmatrix} \Phi^+ \\ \Phi^0 \end{pmatrix} \rightarrow \widehat{H_u} = \begin{pmatrix} \widehat{h_u^+} \\ \widehat{h_u^0} \end{pmatrix} \quad \text{and} \quad \widehat{H_d} = \begin{pmatrix} \widehat{h_d^-} \\ \widehat{h_d^0} \end{pmatrix} \tag{3.4}$$

$\widehat{H_u}$ has still $Y = +1$ and can only give mass to the up-type quarks. Unlike in the SM the second Higgs doublet with $Y = -1$ is needed[1] to give mass to the particles with $T_3 = -1/2$, i.e. down-type quarks and charged leptons.

The Lagrangian for the MSSM consists of three terms:

$$L_{MSSM} = L_{gauge} + L_F + L_{soft} \tag{3.5}$$

With assumed minimality the gauge part is completely determined by requiring gauge-invariance and super-symmetry and has the following form [22]:

$$\begin{aligned} L_{gauge} &= \sum_i (D_\mu S_i)^\dagger (D^\mu s_i) + \frac{1}{2} \sum_i \overline{\Psi_i} \gamma^\mu D_\mu \Psi_i \\ &+ \sum_{\alpha,A} \left[\frac{1}{2} \overline{\lambda_{\alpha A}} (\gamma^\mu D_\mu \lambda)_{\alpha A} - \frac{1}{4} F_{\mu\nu\alpha A} F^{\mu\nu}_{\alpha A} \right] \\ &- \sqrt{2} \sum_{i,\alpha,A} \left(S_i^\dagger g_\alpha t_{\alpha A} \overline{\lambda_{\alpha A}} \frac{1-\gamma^5}{2} \Psi_i + h.c. \right) \\ &- \frac{1}{2} \sum_{\alpha,A} \left[\sum_i S_i^\dagger g_\alpha t_{\alpha A} S_i + \xi_{\alpha A} \right]^2 , \end{aligned} \tag{3.6}$$

S_i are the scalar components of the i^{th} chiral superfield, while Ψ_i are the fermionic components as in the SM Lagrangian 2.8. $F_{\mu\nu\alpha A}$ represents the SM

[1] $\widehat{h_u^{0\dagger}}$ would be a right-chiral superfield and is not allowed in the superpotential.

gauge bosons and $\lambda_{\alpha A}$ are the spin 1/2 superpartners. The first two lines of equation 3.6 contain all gauge-invariant kinetic energy terms. These terms completely determine how all particles couple to gauge bosons. The third line describes the interactions of gauginos with the scalar and fermion components of chiral superfields. $t_{\alpha A}$ are the matrix representations of the gauge group generators. The last term describes quartic couplings of scalar matter fields.

All other couplings are included in L_F, that can be derived from the superpotential. This superpotential is in renormalisable theories an at most cubic polynomial of superfields. It has in the MSSM the following form:

$$\hat{f} = \mu \hat{H}_u^a \hat{H}_{da} + \sum_{i,j=1,3} \left[(\mathbf{f}_u)_{ij} \epsilon_{ab} \hat{Q}_i^a \hat{H}_u^b \hat{U}_j^c + (\mathbf{f}_d)_{ij} \hat{Q}_i^a \hat{H}^{da} \hat{D}_j^c + (\mathbf{f}_e)_{ij} \hat{L}_i^a \hat{H}^{da} \hat{E}_j^c \right] \quad (3.7)$$

The indices a and b are $SU(2)$ doublet indices and show the contraction needed to make this Lagrangian $SU(2)_L$ invariant. $\mathbf{f}_{ij}$ are 3 x 3 Yukawa coupling matrices for the three generations. L_F has the form:

$$L_F = -\sum_i \left| \frac{\partial \hat{f}}{\partial \hat{S}_i} \right|^2_{\hat{S}=S} - \frac{1}{2} \overline{\Psi}_i \left[\left(\frac{\partial^2 \hat{f}}{\partial \hat{S}_i \partial \hat{S}_j} \right)_{\hat{S}=S} \frac{1-\gamma^5}{2} + \left(\frac{\partial^2 \hat{f}}{\partial \hat{S}_i \partial \hat{S}_j} \right)^\dagger_{\hat{S}=S} \frac{1+\gamma^5}{2} \right] \Psi_j. \quad (3.8)$$

The first term is the F-term contribution to the scalar potential and describes scalar masses and interactions. The second includes the mass terms of all SM fermions and their Yukawa couplings.

3.3.1 Supersymmetry Breaking

Supersymmetry is a broken symmetry. So far, there is no understanding of how this breaking actually takes place. The common approach is to assume that supersymmetry is broken in a "hidden sector", that is essentially decoupled from the physics at the "low" energy scale [O(1 TeV)], where we can test it. The effects of SUSY breaking is only transferred to our world by messenger interactions. Because of this ignorance it is only possible to introduce L_{Soft} containing all possible soft SUSY breaking operators by hand. "Soft" means here that these terms are

consistent with all desired symmetries and do not lead to the reappearance of the quadratic divergences in the one-loop corrections to the Higgs mass.

This leads to a total of 178 free parameters. Without the heavily suppressed tri-linear interaction c-matrix terms it is still a total of 124 parameters[1]. It is very hard to make phenomenological analysis with such a huge parameter space. There are some models that reduce the amount of free parameters severely. The minimal supergravity model, as one of them, will be described in the next section.

First electroweak symmetry breaking in the MSSM model will be discussed.

3.3.2 Electroweak Symmetry Breaking

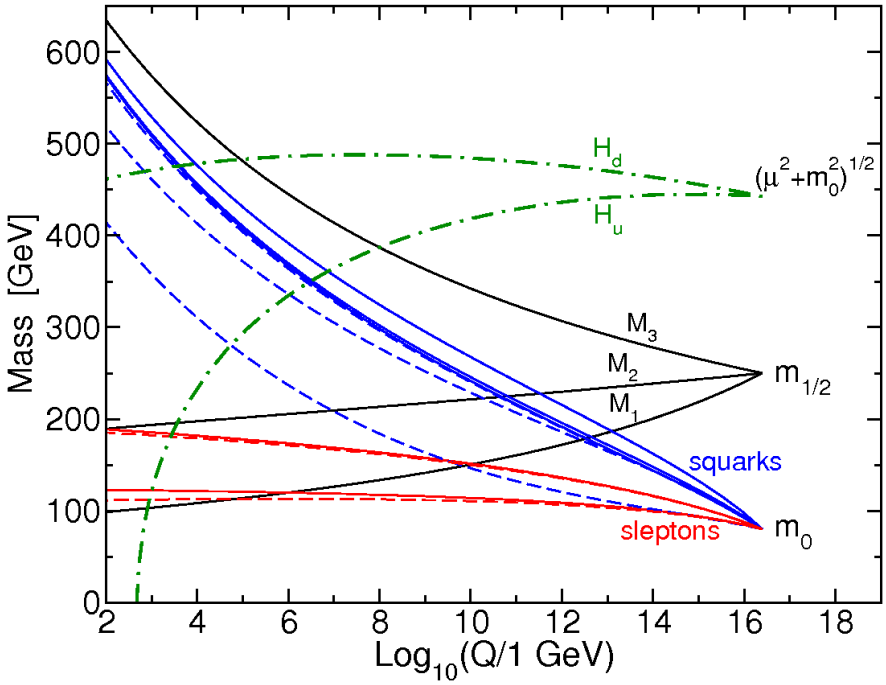

Figure 3.2: *RG evolution of scalar and gaugino mass parameters in the MSSM with typical minimal supergravity-inspired boundary conditions imposed at* $Q_0 = 2.5 \cdot 10^{16}$ *GeV. The parameter* $\mu^2 + m_{H_u}^2$ *runs negative, provoking electroweak symmetry breaking.[21]*

[1]This includes the 19 SM parameters (without neutrino masses). Often only the 105 MSSM parameters are mentioned.

With two Higgs fields there are two vacuum expectation values $\langle h_u^0 \rangle \equiv v_u$ and $\langle h_d^0 \rangle \equiv v_d$. The sum of the two is fixed by a relation very similar to equation 2.21 of the SM. It is given by:

$$v^2 = (v_u^2 + v_d^2) = \frac{2M_Z^2}{g_1^2 + g_2^2}. \tag{3.9}$$

The only free parameter is the ratio between those two:

$$\tan\beta = \frac{v_u}{v_d}. \tag{3.10}$$

Similar to the SM electroweak symmetry breaking, the scalar potential in the MSSM cannot have its minimum at $v_u = v_d = 0$. By the minimisation condition of the potential, $B\mu$ and the value, but not the sign of μ, can be fixed in terms of β, m_{H_u}, m_{H_d} and M_Z, by:

$$B\mu = \frac{\left(m_{H_u}^2 + m_{H_d}^2 + 2\mu^2\right)\sin 2\beta}{2} \quad \text{and} \tag{3.11}$$

$$\mu^2 = \frac{m_{H_d}^2 - m_{H_u}^2 \tan^2\beta}{(\tan^2\beta - 1)} - \frac{M_Z^2}{2}. \tag{3.12}$$

B being the bilinear coupling.

When the symmetry is broken, five physical Higgs bosons develop by mixing of the two doublets. There are two charged Higgs bosons $H^\pm$, two neutral and CP-even bosons h^0 and H^0 and one neutral CP-odd A^0. The masses of these particles can be calculated at tree level:

$$m_A^2 = B\mu(\cot\beta + \tan\beta), \tag{3.13}$$

$$m_{H^\pm}^2 = m_A^2 + M_W^2 \tag{3.14}$$

and

$$m_{h,H}^2 = \frac{1}{2}\left[\left(m_A^2 + M_Z^2\right) \mp \sqrt{\left(m_A^2 + M_Z^2\right)^2 - 4m_A^2 M_Z^2 \cos^2 2\beta}\right] \tag{3.15}$$

According to the last equation h^0 is lighter than the Z boson. Taking radiative corrections into account this still gives an upper limit to m_{h^0} of about 130 GeV. The experimental hints towards a Higgs mass below this value are therefore an encouraging sign.

Using renormalisation group equations (RGE) to calculate $m_{H_u}^2$ and $m_{H_d}^2$ the electroweak scale shows, that m_{H_u} decreases stronger than m_{H_d} with the scale. In fact, calculations show that m_{H_u} turns negative as can be seen in Fig. 3.2 and automatically produces electroweak symmetry breaking . As the electroweak symmetry breaking does not occur at tree level, this mechanism is called radiative electroweak symmetry breaking.

3.4 Particle Content in the Model of Minimal Supergravity

As stated above, the supersymmetry breaking is assumed to take place in a hidden sector. This sector couples to the observable world only via messenger interactions and theories are grouped by the kind of these interactions. As gravity couples to energy, it is a messenger in all theories. Only if this is not swamped by other effects, these theories are called gravity-mediated. In all of these models, supersymmetry is a local symmetry and includes a massless spin-2 graviton that couples to the energy-momentum tensor for matter just as in general relativity. Therefore these models imply (super)gravity. Again, these theories have to be a "not quite so low" energy approximation of a even more fundamental theory, maybe superstring theory, as there are some non-renormalisable parts in the supergravity Lagrangian. This was also the case in Fermi's description of the weak interaction, which also turned out to be a low energy approximation.

In minimal[1] supergravity (mSUGRA) models the large amount of free parameters in the MSSM is extremely reduced. If one assumes gauge coupling unification or makes some simple assumptions on the gauge kinetic function, there are only 5 free parameters[2] left. These are:

$$m_0, m_{1/2}, A_0, \tan\beta, sign(\mu). \tag{3.16}$$

[1]The minimal comes from the minimal (flat) choice for the Kähler metric. Only with this a common scalar mass is obtained.

[2]in addition to the SM parameters

At the GUT scale m_0 is the common mass for all scalars, i.e. sleptons, squarks and higgs bosons. The mass of all gauginos at the GUT scale is $m_{1/2}$. A_0 is the trilinear scalar coupling between the higgs and two sfermoins. μ is the higgsino mass parameter. The sign of μ has a rather small impact on the particle spectrum and except for the masses of the third generation, the effect of A_0 is rather small as well.
The renormalisation group equation (RGE) can be used to calculate the values at other energy scales. After symmetry breaking, particles with the same electric charge, color and spin can mix. Similar to the mixing mechanisms that led to the photon and Z boson, gauge eigenstates are rotated to give the physical mass eigenstates.

The colour-neutral gauginos and higgsinos mix to form four neutral neutralinos χ^0_{1-4} and four charged charginos $\chi^\pm_{1,2}$. They are ordered according to their masses, beginning with the lightest. At the electroweak scale, the gaugino mass parameters for the bino, wino and gluino are approximately 0.4 $m_{1/2}$, 0.8 $m_{1/2}$ and 2.7 $m_{1/2}$, respectively. The lightest neutralino is bino like, the second lightest is wino like, as well as the lighter charginos. The heavier particles are higgsino like. This gives the following rule of thumb [21]:

$$m_{\widetilde{\chi}^0_2} \approx m_{\widetilde{\chi}^\pm_1} \approx 2m_{\widetilde{\chi}^0_1} \approx 0.8 m_{1/2} \tag{3.17}$$

$$m_{\widetilde{\chi}^0_4} \approx m_{\widetilde{\chi}^0_3} \approx m_{\widetilde{\chi}^\pm_2} \approx O(|\mu|) \tag{3.18}$$

The masses for the sfermions and squarks are given by the following formulas [24] [25].

$$m^2_{\widetilde{l}_L} \approx m_0^2 + 0.49 m^2_{1/2} - 0.27 \cos 2\beta M_Z^2 \tag{3.19}$$

$$m^2_{\widetilde{l}_R} \approx m_0^2 + 0.15 m^2_{1/2} - 0.23 \cos 2\beta M_Z^2 \tag{3.20}$$

$$m^2_{\widetilde{\nu}} \approx m_0^2 + 0.49 m^2_{1/2} + 0.5 \cos 2\beta M_Z^2 \tag{3.21}$$

$$m^2_{\widetilde{u}_L} \approx m_0^2 + 5 m^2_{1/2} + 0.35 \cos 2\beta M_Z^2 \tag{3.22}$$

$$m^2_{\widetilde{u}_R} \approx m_0^2 + 4.5 m^2_{1/2} + 0.15 \cos 2\beta M_Z^2 \tag{3.23}$$

$$m^2_{\widetilde{d}_L} \approx m_0^2 + 5 m^2_{1/2} - 0.42 \cos 2\beta M_Z^2 \tag{3.24}$$

$$m^2_{\tilde{d}_R} \approx m_0^2 + 4.4 m_{1/2}^2 - 0.07 \cos 2\beta M_Z^2 \tag{3.25}$$

This approximation does not hold for SUSY-partners of heavy fermions. The masses for the stop are more complicated, as mixing between left and right states appear due to the large Yukawa coupling. This leads usually to the fact that the lighter stop will be the lightest squark and the lightest τ will be the lightest slepton. The missing coupling to the weak charge by right handed particles leads to lighter "right handed" sparticles. Generally squarks are heavier than sleptons because of the large radiative corrections from loops involving gluinos. By increasing $m_{1/2}$ not only all masses are increased, but also the mass-differences of left and right states are increased.

3.5 Production and Decay of Supersymmetric Particles at the LHC

If R-parity is assumed to be conserved, sparticles are always produced in pairs. Therefore a high center of mass energy is needed to produce the heavy sparticles. To cope with this, the Large Hadron Collider (LHC), that is described in detail in the next chapter, is operating with a center of mass energy $\sqrt{s} = 7$ TeV and is planed to be upgraded to the design center of mass energy of $\sqrt{s} = 14$ TeV in 2013. Usually the pair and associated production of squarks and gluinos are expected to be dominant, since they take part in the strong interaction. The last section showed that they are the heaviest superparticles for large parameter space regions, though. The cross section for their production may therefore be kinematically suppressed. This is the reason why the production rate strongly decreases, when $m_{1/2}$ - and for squark production also m_0 - increases as can be seen in figure 3.3. The total SUSY cross section in the cMSSM for $\sqrt{s} = 7$ TeV is shown in FIg. 3.4.

A general feature of supersymmetric decays with conserved R-parity is that the lightest supersymmetric particle (LSP) is stable and as it is usually expected to be only weakly interacting, it leaves the experiment undetected. There are always two such particles and they can lead to an imbalance of the transverse

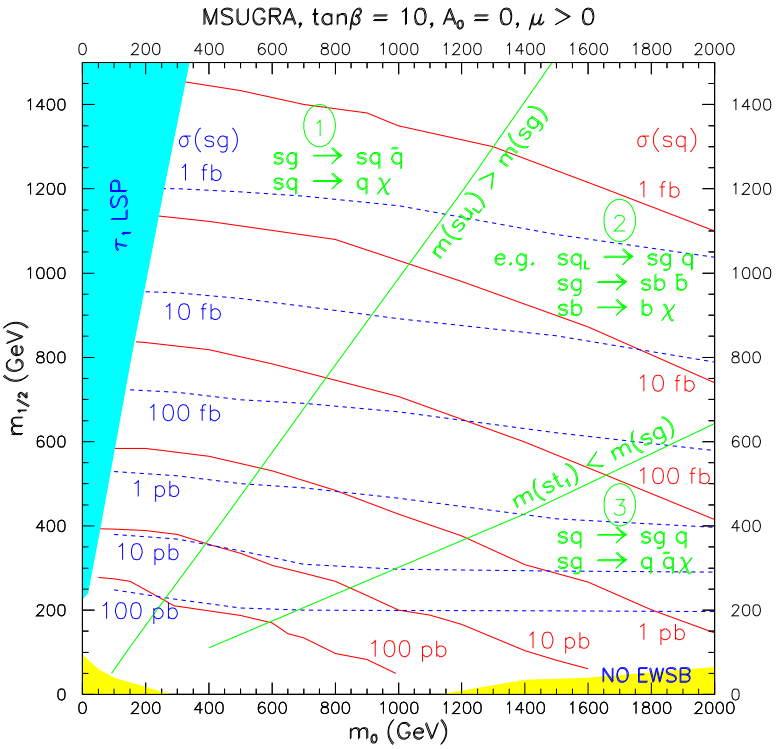

Figure 3.3: Cross sections for gluinos (dotted lines) and squarks (solid red lines) shown for the parameter space at the $m_{1/2}$ vs. m_0 plane with $\tan\beta = 10$, $A_0 = 0$ and $\mu > 0$ for $\sqrt{s} = 14$ TeV [24].

momentum of the visible particles. Large missing transverse energy is therefore present in most supersymmetric events.

Two cases have to be distinguished, depending on which particle is lighter, the lightest squark or the gluino. If $m_{\widetilde{g}} > m_{\widetilde{q}}$, the gluinos decay in the following way:

$$\widetilde{g} \to q + \overline{\widetilde{q}}_{L,R} \quad \text{, or} \quad \widetilde{g} \to \overline{q} + \widetilde{q}_{L,R} \tag{3.26}$$

the squarks decay in one of the following ways:

$$\widetilde{q}_{L,R} \to q + \widetilde{\chi}_i^0 \tag{3.27}$$

$$\widetilde{q}_L \to q' + \widetilde{\chi}_j^{\pm} \tag{3.28}$$

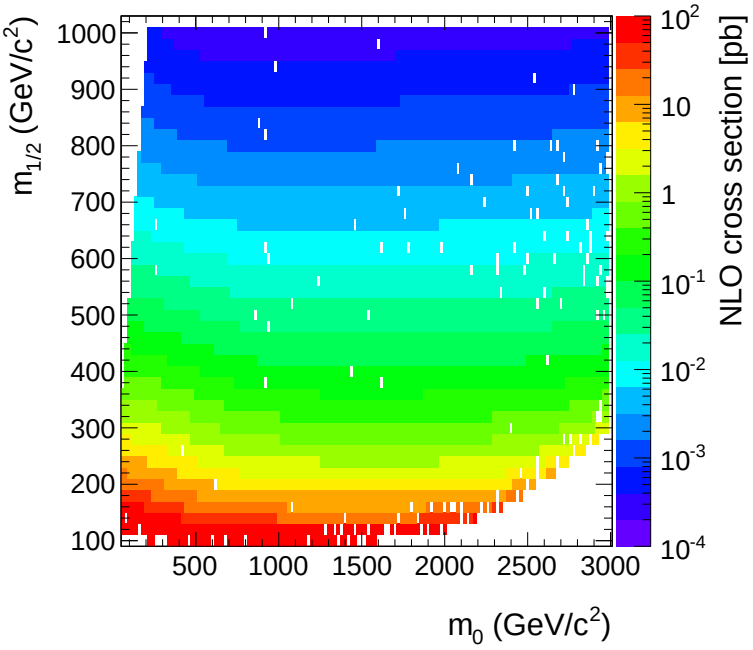

Figure 3.4: NLO cross section for the cMSSM for $\sqrt{s} = 7$ TeV. No cross section is calculated in regions where the stau is the LSP and in regions where there is no electroweak symmetry breaking.

with $i = 1, 2, 3, 4$ and $j = 1, 2$; as long as the decays to the heavier gauginos are kinematically allowed. If $m_{\tilde{q}} > m_{\tilde{g}}$, the squarks decay as:

$$\tilde{q}_{L,R} \to q + \tilde{g} \tag{3.29}$$

the gluinos decay via virtual squarks to:

$$\tilde{g} \to q + \overline{q} + \tilde{\chi}_i^0 \tag{3.30}$$

$$\tilde{g} \to q + \overline{q}' + \tilde{\chi}_j^{\pm} \tag{3.31}$$

$$\tilde{g} \to g + \tilde{\chi}_i^0 \tag{3.32}$$

again with $i = 1, 2, 3, 4$ and $j = 1, 2$, as long the heavier gauginos are kinematically allowed. If q denotes a up like quark, than q' denotes a down like quark and vice versa. All quarks and gluons are reconstructed as jets in the detector. They often have high energy and are present in all supersymetric events. The charginos and neutralinos decay further, but since this analysis is not sensitive to these specific decays including for example leptons, this will not be discussed further.

3.6 Constraints on the Parameter Space

The experiments at the LHC can directly access large parameter space regions for the first time, but there are already a number of constrains from other experiments. Limits on m_0 and $m_{1/2}$ from the LEP or the Tevatron experiments will be displayed when the results of this analysis is presented. As these limits are less stringent than the limits set with the analysis discussed here, these limits are not discussed further.

As A_0 and the sign of μ do not have such a strong influence on the mSUGRA models, there are no strong limits on them and they will not be discussed further. $\tan\beta$ is important to calculate the Yukawa couplings. As β appears in the denominator of the Yukawa couplings of up and down quarks respectively, $\tan\beta$ has to lie between [21]:

$$1.2 < \tan\beta < 65, \tag{3.33}$$

to keep them reasonably small. For the presentation of the results a default value of $\tan\beta = 10$ is used.

Indirect bound as for example bounds from the dark matter density measurements are not taken into account here. However, the region in parameter space, where the LSP is the charged stau, wich is disfavoured by cosmology and the region where no radiative electroweak symmetry breaking would occur is highlighted when the results are presented as well as in Fig.3.3.

4

The Experiment

4.1 The Large Hadron Collider

The Large Hadron Collider (LHC) [2] [26] [27] is a proton-proton accelerator at CERN in the tunnel of the former Large Electron Positron Collider (LEP) [1] with a circumference of 27 km. The first proton beams were circulated succesfully on 10th September 2008, but 10 days later operation was stopped due to a serious incident with a superconducting connection between magnets, leading to a break of the liquid helium containment. Operation has restarted in mid-November 2009. The first proton beams had an energy of 450 GeV per particle leading to a center of mass energy of$\sqrt(s) = 900$ GeV. On 30th March 2010 the first collisions with $\sqrt{s} = 7$ TeV took place. This is half the design center of mass energy of 14 TeV, which will not be accessable before the planned upgrade in 2014. In 2012 the center of mass energy is planned to be increased to 8 TeV. The instant luminosity, which is a measure of how often collisions between paticles occur, is still increasing. While the total dataset of the 7 TeV run in 2010 corresponds to an integrated luminosity of about 36 pb^{-1} of good quality data, about 5 fb^{-1} has been collected in 2011. On 21st April 2011 a world record was broken with a peak luminosity of $4.67 \cdot 10^{32}\text{cm}^{-2}\text{s}^{-1}$.

Beside the Compact Muon Solenoid (CMS) [4], that will be described in detail in this chapter, there are three other experiments. ATLAS [3] [28] is a multi-purpose detector similar to CMS, LHCb concentrates on the CP-violation in b-physics and ALICE is designed to investigate the quark-gluon plasma produced

in heavy ion collisions, which took place for the first time at the LHC on 8th November 2010.

4.2 The Compact Muon Solenoid

The two main goals of the CMS [4] scientific program is to find the Higgs boson and to look for physics beyond the standard model with supersymmetry being the most promising candidate. Further topics are top-physics, electroweak physics and QCD. To achieve these goals the CMS detector has to identify the emitted particles and measure their momentum as precisely as possible. To measure the momentum of charged particles a very strong magnetic field of about 3.8 Tesla is applied and the curvature of the tracks of the particles measured. To make use of the measurement of the transverse momentum balance, which is very important in most searches for physics beyond the standard model, there has to be a good coverage detecting also particles that are emitted in forward direction rather close to the beampipe. The variable to measure the angle towards the beampipe is the pseudorapidity η, defined as:

$$\eta = -\ln\left(\tan\frac{\theta}{2}\right) \tag{4.1}$$

It has the advantage over the angle θ that the difference between the pseudorapidity of two particles is in the relativistic limit [1] independent of the Lorenz boost along the beam axis, i.e. Lorenz invariant.

The total detector is shown in figure 4.1. It is cylindrical and has a length of 30m, a radius of 7.5 m and a total weight of 12500 t. The larger sub-detectors are, starting from the collision center to the out most detector:

- the inner tracker with the silicon pixel vertex detector and silicon strip detectors,
- the electromagnetic crystal calorimeter,
- the hadronic metal-scintillator calorimeter,

[1] pseudorapidity is in the relativistic limit equivalent to rapidity, which is a Lorenz invariant.

- the superconducting solenoid coil,
- the muon system consisting out of drift tubes (DT), cathode strip chambers (CSC) and resistive plate chambers (RPC)

These subdetectors are discussed below in more detail.

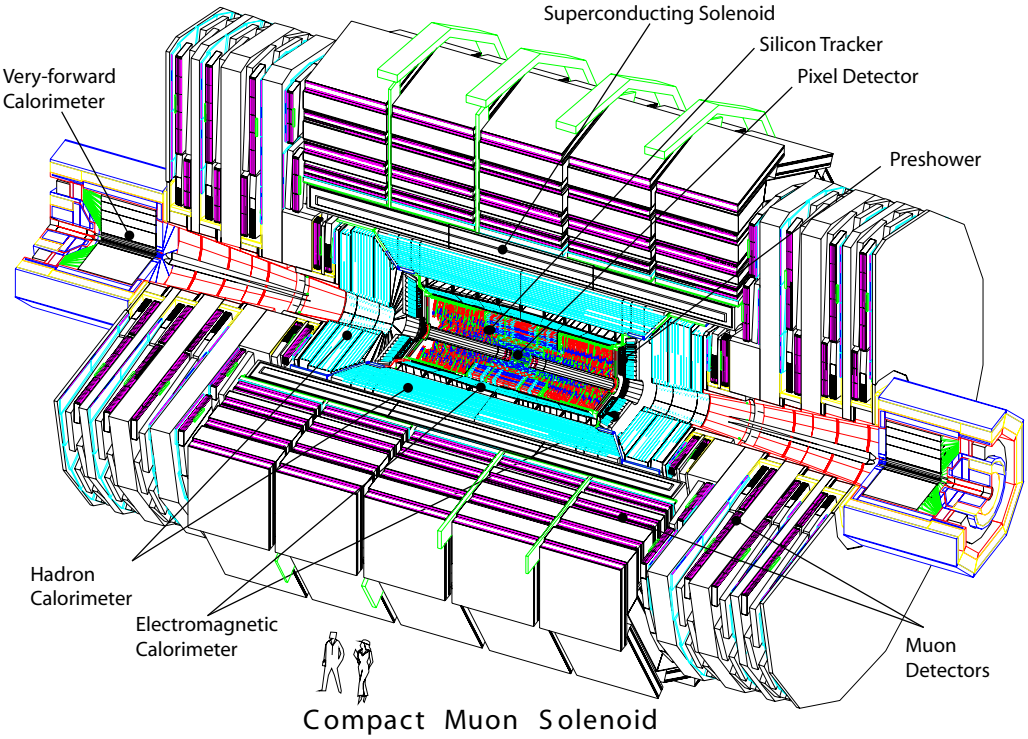

Figure 4.1: The CMS Experiment with labels on all major components [4].

4.2.1 The Inner Tracker

Charged particles deposit a signal in the silicon sensors of the inner tracker. These sensors allow a fast and precise reconstruction of these hits. These hits can than be fitted to reconstruct tracks of charged particles.

The tracker consists of two parts. Closest to the interaction point is the pixel detector. It has a high granularity, which is necessary because of the high particle flux. The high resolution of the pixel sensor also gives a high resolution to

the vertex reconstruction of 25μm and 20μm in X or Y and Z, respectively [29], allowing the recognition of secondary vertices that can be used to identify jets originating from b-quarks due to the lifetime of the b-quark. Also vertices from additional, usually soft, interactions in one bunch-crossing, called pileup interactions, can be distinguished and therefore a good estimate on the level of pileup in data is possible. The pixel detector consists of about 55 million pixels and has a total area of about 1 m^2.

Outside of the pixel detector is the silicon strip detector. It consists of about 9.6 million strips with a total area of about 200 m^2, providing a coverage up to $|\eta| < 2.4$. Over 99% of the sensors of the inner tracker are in operation.

The tracks of charged particles are bend in the strong magnetic field. This allows to reconstruct the transverse momenta of charged particles, i.e. the momentum projected on the transverse detector plain:

$$p_T = 0.3 \frac{GeV}{c \cdot T \cdot m} \cdot B \cdot \rho \tag{4.2}$$

where ρ is the radius of the bent track and B is the magnetic field.

The track reconstruction efficiency is about 95% for pions in the central region declining to about 85% in the endcap region for pions with a p_T between 1 GeV and 100 GeV. Muons have a reconstruction efficiency of about 99 % if their transverse momentum is larger than 1 GeV [30].

Due to the strong focus on the tracker in the CMS design and the high magnetic field the CMS tracker has a very good resolution of the transverse momentum of charged particles. For high energetic particles of about 100 GeV up to an $|\eta|$ range of 1.6 the resolution is about 1-2 %, decreasing towards higher $|\eta|$ values [4]. Multiple scattering is responsible for about 30% of the resolution. For particles with a lower transverse momentum the resolution is even better, dominated by multiple scattering.

4.2.2 The Electromagnetic Calorimeter

The electromagnetic calorimeter (ECAL) of CMS is made out of 61200 lead tungstate ($PbWO_4$) scintillating crystals in the barrel up to $|\eta| < 1.479$ and 7324 crystals in each of the endcaps at the pseudorapidity $1.479 < |\eta| < 3.0$.

Lead tungstate crystals are chosen because they can be read out very fast, are radiation hard and have short radiation ($X_0 = 0.89$ cm)[1] and Moliere (2.2 cm)[2] legths, which is necessary to make the detector small enough to fit together with the inner tracker and the hadronic calorimeter inside the coil. The drawback of this material is a rather low light yield. Therefore photomultipliers are used to detect the light emmited by the crystals.

The crystals in the barrel region each cover 0.0174 in $\Delta\Phi$ and $\Delta\eta$ at the front face and have a length of 230 mm ($= 25.8X_0$) while the crystals in the endcap cover 28.6 x 28.6 mm^2 at the front face with a length of 220 mm ($= 24.7X_0$). Lead tungstate is very dense and therefore heavy. The ECAL barrel alone weights 67.4 t. A preshower device is used at the endcaps to improve the identification of electrons and photons.

The energy resolution can be parametrised as:

$$\left(\frac{\sigma}{E}\right)^2 = \left(\frac{S}{\sqrt{E}}\right)^2 + \left(\frac{N}{E}\right)^2 + C^2 \tag{4.3}$$

where σ is the standard derivation of a Gaussian fit. The energy is measured in GeV. The first term is the stochastic term measured in the test beam to be $S = 2.8\%$, the second term is due to noise with $N = 0.12$ and the last, constant term has a value of $C = 0.3\%$ and is due to calibration errors and systematic effects [4].

The response of a calorimeter is defined as the measured energy divided by the true energy. The ECAL has a different response for electrons and hadrons. The ratio between the response of electrons and hadrons $e/h \approx 1.6$. Only ECAL cells above a certain threshold and their neighboring cells are read out to reduce the effect of noise. This is called selective readout.

The ECAL generally works as expected, but the readout for a few crystals is broken [31]. In most cases the trigger information is still available, though.

[1]The radiation length is the distance, after which an electron has only 1/e of its original energy left.

[2]Inside one Moliere radius 90% of the energy is deposited.

4.2.3 The Hadronic Calorimeter

The hadronic calorimeter (HCAL) consists of four parts. The hadron barrel (HB) is the central part of the HCAL with $|\eta| < 1.4$. It consists of 2304 towers with a segmentation of $\Delta\eta \times \Delta\Phi = 0.087 \times 0.087$. The absorber material has to be non-magnetic, with an absorption length as short as possible. Is was chosen to be mostly brass[1] (5.05 cm thick for each of the inner 8 layers, 5.65 cm for the remaining 6 layers). Only the first and the last layer is made out of stainless steel for structual reasons. In between these layers and in front of and behind the steel is a scintillator with a thickness of 3.7 mm, except for the first layer directly behind the ECAL, that is 9 mm thick. As the space inside the solenoid coil is very limited and high energetic jets may not deposit their entire energy, there are also scintillators outside the coil, which has $1.4/\sin\theta$ interaction lenghts. This is called the hadron outer (HO) detector. This is, however, not used in the jet reconstruction for the data used in this thesis, as the level of noise is not sufficiently small. The third part is the hadron endcap (HE), located in the pseudorapidity region between 1.3 and 3.0. The material used is only brass (78 mm thick) and scintillator (3.7 mm thick). The five towers closest to the center have about the same segmentation in η and Φ as inside the barrel. To higher $|\eta|$-values the $\Delta\Phi$ segmentation is $10\,^\circ$, which is only half as fine as inside the barrel. The η segmentation changes from $\Delta\eta = 0.087$ to $\Delta\eta = 0.7$ for $|\eta| > 1.6$. Closer to the beam, at $3.0 < |\eta| < 5.0$ the hadron forward (HF) detector is located. This part is made out of steel absorbers and radiation hard quartz fibres. It is located 11 m from the interaction point and is constructed out of 18 wedges. The increased coverage helps to use the transverse momentum balance.

The HCAL is like the ECAL a non-compensating calorimeter with $e/h \approx 1.4$. Only calorimeter cells above a threshold are read out to reduce the effect of noise. This is called zero suppression.

4.2.4 The Solenoid

The magnet is a key element in the CMS design. The 12.9 m long superconducting solenoid is 1.8 m thick and has an inner diameter of 5.9 m. The use of the strong

[1] 70% copper and 30% zinc

field of about 3.8 Tesla was motivated by the momentum resolution for charged tracks. The solenoid coil is the main part in the CMS experiment as its choice dictates the size and therefore the whole design of the calorimeters. The current used to provide this field is 19.5 kA, resulting in a total stored energy of 2.7 GJ.

4.2.5 The Muon System

Muons are very penetrating as they are minimal ionizing particles and pass therefore even through the solenoid with only minimal loss of energy. The muon system covers the area $|\eta| < 2.4$ and can be divided into a central and two forward parts. In both parts of the system four stations are installed. They are separated by the iron return yoke, that also serves as an absorber for bremsstrahlung photons, electron positron pairs and hadron punch-through. In the central part with $|\eta| < 1.2$, muon rates are rather small. Therefore, drift tube (DT) chambers are used as a tracking device. In the endcaps muon rates are higher, which has led to the choice of cathode strip chambers (CSC). In both parts resistive plate chambers (RPC) are used as well. Compared to the other technologies, they do have a poor position resolution, but a very good time resolution needed for the L1 trigger.

For low energetic muons the measurement is dominated by the inner tracker. For higher energetic muons, where multiple scattering and energy loss can be neglected, a combination of the measurements of the tracker and the outer muon system gives a long lever arm that improves the measurement of the curvature of tracks. This gives not only a better resolution for the momentum measurement, but also increases the probability to determine the charge of muons.

The muon momentum scale is measured to a precision of 0.2% with muons from Z decays. The transverse momentum resolution varies from 1% in the barrel to 6% in the endcaps for muons below 100 GeV and better than 10% in the barrel for muons up to 1 TeV [32].

4.2.6 The Trigger

The design beam crossing interval for proton-proton collisions is 25 ns, corresponding to a frequency of 40 MHz with several collisions at each crossing at the high instant luminosity reached. Considering the large amount of information

coming from the various subsystems, not all data can be stored. As the high luminosity is needed for rare processes, the only solution is to find and to save the interesting data only. This is done by the trigger in two steps. The Level 1 (L1) trigger is there to quickly filter the more interesting results based on a preliminary event reconstruction. Only the fast components are used in the decision taken, and the reconstruction techniques are less exact for speed reasons. The trigger looks for interesting signatures, such as high p_T jets, photons or leptons, high jets multiplicities or a large $\not{E}_T$. It needs to reduce the frequency of events to about 50 kHz [33]. As this is still too much to record, the High Level Trigger (HLT) filters these events further. Here more sophisticated reconstruction algorithms are used, now with higher thresholds. This reduces the event rate that is written to the mass storage devices to about 150 Hz [33]. The trigger thresholds depend on the instant luminosity and therefore need to be adjusted. With the current luminosity these thresholds become quite large and specific cross triggers, with cut on more than one physics object, are put in place to reduce the rate sufficiently.

5

Experimental Signatures of Particles

In this chapter the objects used in the analysis will be discussed with special focus on jet reconstruction and correction. An alternative approach for jet corrections using tracks of charged particles is presented. As discussed in chapter 4.2, the resolution of the tracker is much better than the resolution of the calorimeters up to high energies. This is the reason why the inclusion of tracker information can improve the jet resolution considerably. In the following the detector response of isolated tracks will be compared to the fitted response of tracks inside jets to verify that a measured track response can be used for the correction of jets.

At the end of this chapter the particle flow algorithm is presented that also makes use of tracker information. The aim of this algorithm is to reconstruct every particle in the event - even within jets. This algorithm is used in the remainder of the analysis.

5.1 Signals of Particles

Particles will interact with the detector components in the following way:

- Photons will not interact with any detector component until they transform to an electron-positron pair, leading to an electromagnetic shower.

This happens in the tracker with 50% probability, but usually the dominant energy deposition of the shower is produced in the electromagnetic calorimeter. The leakage in the HCAL is negligible. All kinematic properties of the photon are reconstructed from the ECAL cluster.

- Electrons will leave a single track in the tracker pointing to the part of the electromagnetic calorimeter, where the energy is deposited via an electromagnetic shower in the same way as for photons. The track gives a better resolution on the kinematic variables up to more than 100 GeV. The electron will also radiate bremsstrahlung photons. The ECAL clustering, and in particular the building of superclusters (clusters of clusters), is designed to take into account the Φ spread due to the bremsstrahlung energy [34]

- Muons are minimal ionizing particles. They will leave a track in the tracker, but only about 5 GeV energy will be deposited in the calorimeter. They are the only particles that will reach and interact with the muon system. They can therefore be identified with high efficiencies.

- Jets originate from gluon radiation or quarks. As described previously in section 2.2.2, these particles cannot be observed as free particles. It is energetically favourable to create particle anti-particle pairs to form colour-neutral bound states. This process is called hadronisation. These bound states are emitted close to each other as jets in the direction of the originating particle.

  As they consist to some extend out of charged particles, they will leave a signal in the inner tracker and in the electromagnetic calorimeter, but usually most of the energy will be deposited in the hadronic calorimeter. If a jet has a lot of energy, it is possible that the shower extends behind the hadron calorimeter. This is referred to as "punch-trough" and is one of the main sources of jet mismeasurements at high energies.

  More details on the signal of jets will be discussed later in this chapter.

- Taus can decay leptonically or hadronically. The tau decays always to an odd number of charged particles and therefore tracks. If a high energetic

tau decays hadronically, the resulting jet will be rather narrow, but specific tau identification is not used in this thesis.

- Weakly interacting particles like neutrinos or neutral LSPs will leave no signal in the detector. An estimate for the p_T of such particles can still indirectly be obtained from the transverse energy balance of all energy measured in the detector $\overrightarrow{\not{E}_T}$.

$$\overrightarrow{\not{E}_T} = -\sum_{\mathrm{i}} \overrightarrow{E_{T,i}} \tag{5.1}$$

5.2 Jets and Jet Energy Corrections using Tracks

As most of the energy in the detector is deposited in jets, a precise measurement of their kinetic properties is most important. This is especially true for the analysis described in this thesis as it is a hadronic SUSY search with high energetic jets and missing transverse momentum as most important signatures.

Standard calorimeter jets are a cluster of energy within the calorimeters around an area of large energy deposits. Several clustering algorithms are used in high energy physics such as the sis-cone or the anti-kt-algorithm [35]. These algorithms need to make sure that the resulting jet observarals measured are infrared- and collinear-save [35]. As the CMS calorimeter is non-compensating, i.e. has a different response for electrons and hadrons, the response of a typical jet varies with p_T and η. The jet response R is defined as:

$$R^{\mathrm{jet}} = \frac{p_T^{\text{jet measurement}}}{p_T^{\text{jet truth}}} \tag{5.2}$$

The dependence of the mean R^{jet} on p_T and η can be seen for simulated data in Fig. 5.1. The standard approach is to determine correction factors as a function of p_T and η to get an average jet response of unity. As there is one correction factor to make the response flat as a function of η and one to bring the absolute sale to unity this approach is called the factorised approach in the

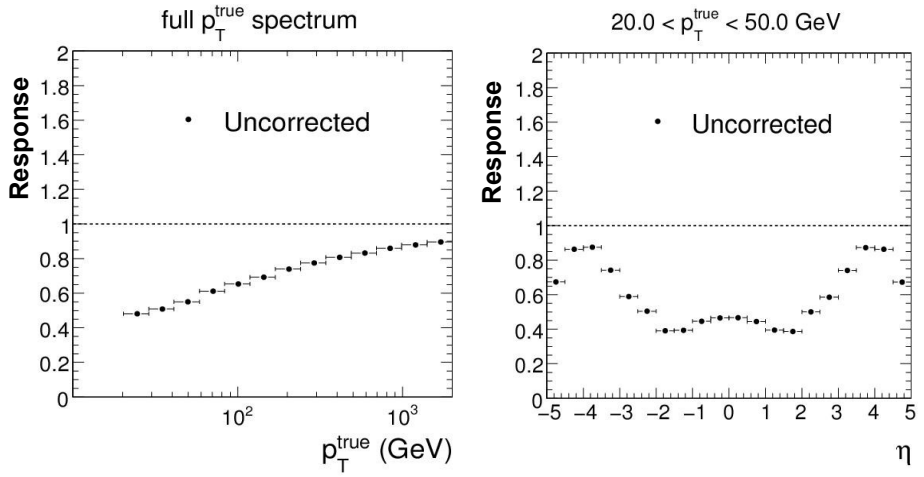

Figure 5.1: Jet response as a function of p_T^{truth} (left) and η^{truth} (right) for uncorrected jets.

following [1] However, such an approach can not improve the jet resolution within one bin.

Typically, the mean fractions of the jet transverse momentum carried by the charged hadrons, photons and neutral hadrons are 65%, 25% and 10% , respectively [36]. These values differ strongly on a jet to jet basis. Photons have intrinsically a very high energy resolution as electromagnetic showers contain very many particles and thus fluctuate far less than hadronic showers. Neutral hadrons can interact with the tracker or the ECAL, but usually deposit most of their energy in the HCAL leading to a hadronic shower with an intrinsically worse resolution. Charged hadrons behave similarly, but they leave a track in the inner tracker that can be measured with high precision.

The basic idea of a jet correction with tracks is to use the measurement of the tracker for the charged hadrons inside the jet and thereby improve the jet resolution considerably. The standard algorithm at CMS that uses this correction

[1] Additional correction factor such as e.g. an optional flavour correction can be included as well.

is the jet plus track (JPT) algorithm [37]. In this algorithm the jet measured by the calorimeres only is corrected by adding the track p_T of the tracks insinde the jet and subtracting the expected calorimeter response of the particles belonging to these tracks. The expected calorimeter response is measured from events with isolated tracks. This algorithm is able to correct jets with several low energetic particles different to a jets of the same energy from few high energetic particles. These jets have different response R^{jet} due to the non-linearity of the calorimeter.

The jet-flavour distinguishes jets originating from gluons, light quarks and heavy quarks. Due to different fragmentation properties of the corresponding jets and the non-linearity of the calorimeter the jet response of gluons, light and heavy quarks differs by up to 10%. The JPT algorithm reduces the dependence on the flavour of the jet.

In the following an alternative approach is discussed that uses a fit to determine the calorimeter response of charged particles inside jets together with a correction factor for the neutral component of the jet.

5.2.1 Alternative Jet plus Track Correction

The transverse momentum of a jet measured in the calorimeter p_T^{Calo} can be written as:

$$p_T^{Calo} = R^0 p_T^{0,true} + R^{\pm} p_T^{\pm,true}, \tag{5.3}$$

where $p_T^{0,true}$ and $p_T^{\pm,true}$ are the true transverse momentum carried by neutral and charged particles, respectively. R^0 and $R^{0\pm}$ are the responses of the total neutral component of the jet and the responses for individual charged particles, respectively.

With the approximation that tracks are measured with perfect momentum resolution the neutral component of the jets can be written as:

$$p_T^{0,true} = \frac{1}{R^0} \cdot (p_T^{Calo} - R^{\pm} p_T^{tracks}) \tag{5.4}$$

Only tracks that enter the calorimeter within the jet conus are taken into account. As the response of electrons is well calibrated, electrons do not need to

be corrected for. As a good part of electrons come from photon conversion, only tracks that originate from the vertex are taken into account.

If the response of the neutral component of the jet is approximated to be dependent of p_T and η only, the total jet energy can be improved by using:

$$p_T^{Corr}(p_T^{Calo}, p_T^{tracks}) = C^0(p_T, \eta) \cdot (p_T^{Calo} - R^{\pm} p_T^{track}) + p_T^{track,Vertex} \tag{5.5}$$

with $C^0 = 1/R^0$. The tracks that are added to the jet are only those tracks that are within the jet conus at the vertex. Charged particles that are bent outside the track conus are therefore taken into account in the jet correction, while the jet is cleaned from the contribution of charged particles that end up in the jet conus even though they are emmited in a different direction. As the track p_T is proportional to the radius of the curvature, the track resolution decreases with increasing energy while the energy resolution in the calorimeter improves with energy. High energetic mis-measured tracks can lead to a severe mis-correction of the jets. Therefore, no tracks above 100 GeV are taken into account for the correction. [1]

The parameters $C^0(p_T, \eta)$ and $R^{\pm}$ in the formulas above need to be determined in order to get a jet correction. C^0 is parametrised similar to the relative correction of the standard CMS jet correction [38] as:

$$C^0(p_T) = X_1 + \log(p_T/\text{GeV}) \cdot (X_2 + \log(p_T/\text{GeV}) \cdot X_3) \tag{5.6}$$

and is calculated for 42 different η regions each corresponding to 2 towers for most of the detector. The free parameters X_{1-3} will be determined by the fit described below. The response of charged hadrons is parametrised as proposed by Groom [39]. The response is calculated using the expected π^0-fraction f_{π^0}. With the assumtion that the photons from e.g. neutral pion decay have a response of unity and hadrons have a response of h/e the total response is:

$$R^{\pm} = \frac{1 + (e/h - 1) f_{\pi^0}}{e/h} \tag{5.7}$$

[1] A more elegant way would be to weight the correction with tracks according to the resolution $w = \frac{\sigma^2_{calo}}{\sigma^2_{calo} + \sigma^2_{track}}$, but no strong effect was seen as the track resolution is vastly superior for low p_T and the correction with tracks is smaller for high p_T tracks.

The value e/h is used as a free parameter in the fit. The expected π^0-fraction is parametrised as:

$$f_{\pi^0} = 1 - (A \cdot E_{track})^{B-1} \tag{5.8}$$

With A and B being the last free parameter in thel fit. These parameters are determined for 3 $|\eta|$-regions, with the $|\eta|$-values of the edges being 0.88, 1.74.

The true transverse jet energy is found by comparing it to the transverse energy of a photon in events where an isolated photon is back to back with a jet. The following cuts are made to ensure a clean event topology:

- $p_T^\gamma > 40GeV$
- $\Delta\Phi$ btween Φ^{jet} and $(\Phi^\gamma - \pi) < 0.15$
- p_T of second leading jet < 5 GeV

Balancing two jets against each other can also be used to calibrate the jets, but such events cannot set the absolute scale of the jet energy corrections. In the following only simulated photon-jet events are used.

The Fit

To construct a χ^2-function that allows to find an unbiased estimation of the best parameters for the correction function first the mean expected measurement of the jet p_T^{Exp} has to be found from the photon transverse energy for each event. This is done by numerically solving:

$$p_T^{Corr}(p_T^{Exp}, p_T^{tracks}) - p_T^\gamma = 0 \tag{5.9}$$

The parameters for the p_T^{Corr} as defined in Eq. 5.5, that is in average closest to p_T^γ can be found by minimising the χ^2-function[1]:

[1]Note that this form of the χ^2-function with the expected measurement is necessary as other χ^2-functions can introduce a bias to the measurement as described in detail in [40]. This is only the final result if the uncertainty does not depend on the parameters found.

$$\chi^2 = \sum_i^{Nevt} \left(\frac{p_{T,i}^{Exp} - p_{T,i}^{Calo}}{\sigma(p_T^{Exp})} \right)^2 \tag{5.10}$$

The uncertainty of the jet is parametrised as:

$$\sigma^2(p_T^{Exp}) = P_1^2 + P_2^2 \cdot (p_T^{Exp}/\mathrm{GeV}) + P_3^2 \cdot (p_T^{Exp}/\mathrm{GeV})^2 \tag{5.11}$$

P_1, P_2 and P_3 being constants calculated for 5 different $|\eta|$ regions from Monte Carlo simulation. For the central region with $|\eta| < 0.8$ these are $P_1 = 4.44$, $P_2 = 1.11$ and $P_3 = 0.03$ [1]. The main difference towards higher $|\eta|$ values is a smaller stochastic term P_2, because the energy is higher if the transverse energy is the same. This is the dominant uncertainty for most jets.

As the σ of the expected measurements depends on the parameters used in the correction, an additional term has to be added to the χ^2-function [2]. The free parameters described above are therefore found by minimising:

$$\chi^2 = \sum_i^{Nevt} \left(\ln(\sigma^2(p_{T,i}^{Exp})) + (\frac{p_{T,i}^{Exp} - p_{T,i}^{Calo}}{\sigma(p_{T,i}^{Exp})})^2 \right) \tag{5.12}$$

This minimalisation is performed using LVMini [42], which is suitable for determining a high number of free parameters in an unbinned maximum likelihood fit with an acceptable memory consumption.

5.2.2 Performance

To test the performance of this jet correction, simulated jets that pass through the detector simulation and reconstruction are corrected with this approach. These corrected jets are then compared to the true jet energy that is available for simulated events. In the following, the jet response $\overline{R}$ is defined as the mean of the Gauss-fit on the distribution of R^{jet} as defined in Eq. 5.2. The jet resolution $\sigma(R)$ is the width of this fit divided by $\overline{R}$ to make the resolution independent of the jet

[1] These numbers correspond to the MC sample studied. More recent uncertinty functions for data taken can be found in [41]

[2] This term is present in all χ^2-functions, but can be ignored if it does not depend on the parameters to be optimised.

energy scale. $\overline{R}$ and $\sigma(R)$ for jets in a QCD sample corrected with the approach discribed above are shown in figure 5.2 in comparison to uncorrected jets, the standard factorised approach denoted as L2L3 and the standard correction using Tracks [37] denoted as JPT.

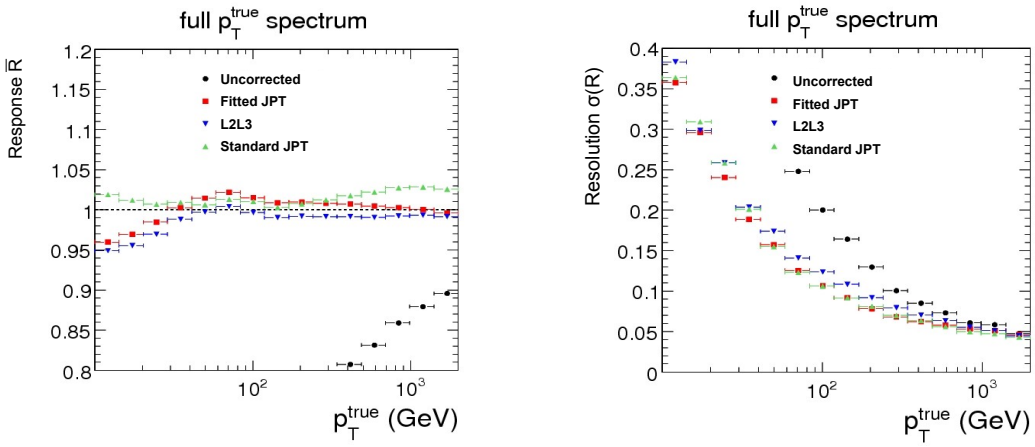

Figure 5.2: Jet response (left) and resolution (right) for uncorrected jets (black), jets corrected with the fitted track correction discussed in the text (red), jets corrected with the standard JPT algorithm (green) and jets corrected with the standard factorised approach (blue).

It can be seen that all corrections are able to get the response to unity within 5% (3% for jets with $p_T > 30$GeV). The resolution of track corrected jets is superior to standard corrections with slight improvements from the fit presented here [1]. It should be noted that the studies presented here do not take recent developements into account. While the qualitative statements remain true, more recent jet energy response and resolution measurements should be taken from [41].

As a cross check that the response of charged particles $R^{\pm}$ used in the correction has a physical meaning, it is compared to the measurements of the response of isolated pions [37] without HCAL zero suppression or ECAL selective readout, discussed in chapter 4.2. This readout was chosen for comparison because these thresholds are expected to be passed insinde jets and because this is the charged particle response used in the standard JPT algorithm. This comparison is shown

[1] At energies below 30 GeV the gauss fit does not perfecltely resemple the resolution distribution. In particular the performence of the standard JPT algorithm is slightly underestimated.

in figure 5.3. It can be seen that both measurements of the track response agree well except for very low track p_T. This difference can be explained due to the difference in the remainder of the correction. As the global correction parameter C^0 and the response of charged particled $R^{\pm}$ is fitted simultaneously, there is a correlation between both. The difference in the track response is countered by an opposite difference in the global correction parameter for low energies. Other differences are other charged particles than pions in the jet and the different environment due to the high energy density inside jets. Due to the overlap of measurements from different particles in the calorimeter and because of the different readout (zero suppresion and selective readout) the effect of noise can differ between both measurements, especially at low track p_T. As the corrections is applied to tracks inside jets this is an advantage of the method using the global fit. It can be said, that the use of track responses measured from isolated tracks works well for tracks with $p_T > 5$ GeV.

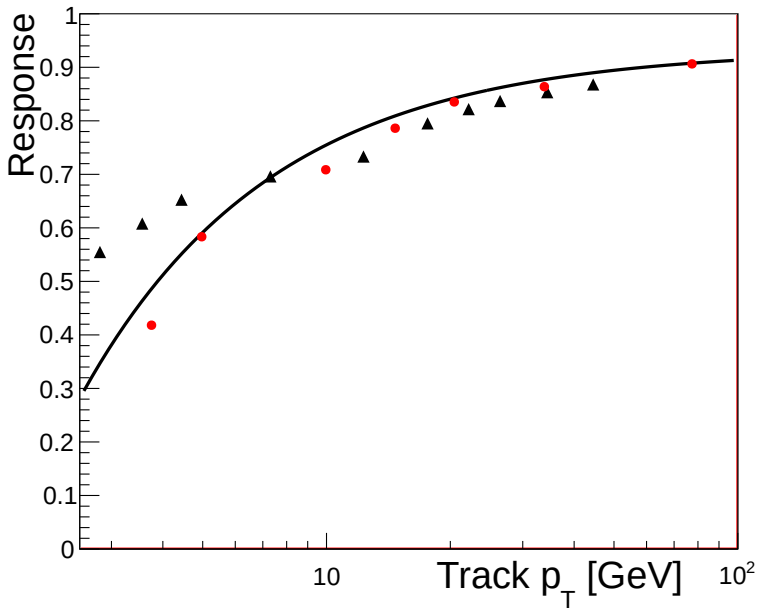

Figure 5.3: Central calorimeter response of charged particles as measured with isolated pions (triangles) taken from 5.2 and $R^{\pm}$ from the fit. The functional form is indicated by the line, a binned cross check is indicated by red cdots.

To check that the functional parametrisation for the track response assumed in Eq. 5.7 and Eq. 5.8 is a good choice, the track response is also fitted in bins of track p_T. The result is also shown in Fig. 5.3 and good agreement between the binned results and the functional form can be observed.

The fitted value for e/h is an effective value that combines the HCAL and the ECAL. Furthermore this parameter is correlated to other parameters in the response of charged particles. Therefore this value is not be compared to the measured values of e/h for the HCAL and ECAL from test beam measurement.

5.3 The Particle Flow Algorithm

The best resolution with jets can be obtained if all particles within a jet are identified and their energies are corrected accordingly. This is done within the particle flow (PF) algorithm and in the following all objects are reconstructed with this algorithm if not stated otherwise. The anti-kt algorithm is used to cluster jets.

The general concept is very similar to the aproach described above. The main difference is that the tracks are linked to clusters of ECAL and HCAL energy in the calorimeter. With this information it is not only possible to identify electrons and photons in the jets, but also to avoid over-subtraction of calorimeter energy linked to a track. More information can be found in the publication [36].

5.4 Summary of the Jet Energy Corrections

It has been shown that the use of jet energy corrections is crucial in for an analysis relying on jet measurements. While a simple correction factor that depend only on the p_T and η of the jet is capable of correcting jets to the correct jet energy scale, the resolution of the jet energy measurements can be improved severly with the additional information of precisely measured tracks inside the jet. To further improve the jet measurement, the full granularity of the calorimeter is used to reconstruct single particles insinde the jets with the particle flow algorithm. The non-Gaussian tails in the jet energy resolution of PF jets are shown to be under control [43]. These studies have led to the conclusion of useing PF jets in this

thesis unless stated otherwise. However, with the increased instant luminosity at the LHC additional interactions in one buch crossing make it increasingly difficult to reconstruct every particle in the event and the reconstruction-time per event has already increased considerably. It is therefore important to maintain the simpler jet correction methods, at least to cross check the results aquired with the particle flow algorithm.

6

Search Strategy

6.1 Introduction

An earlier version of the analysis discussed in this thesis on the data taken in 2010 is accepted at JHEP [44]. A more recent version on the data discussed here is also public [45].

The aim of this analysis is to discover new physics on the base of a transverse momentum imbalance and high energetic jets. This is a typical signature of supersymmetric events as discussed in chapter 3.5, but all theories with heavy particles that decay finally to a dark matter candidate will show this signature. The two most important search variables are H_T and $\not{H}_T$ as defined blow:

$$H_T = \sum_{\text{Jets}} |\vec{p_T}| \tag{6.1}$$

$$\not{H}_T = | - \sum_{\text{Jets}} \vec{p_T}| \tag{6.2}$$

Cuts on other event properties are used to ensure good data quality and to reduce the Standard Model background. These cuts are chosen in a way that a good signal efficiency is maintained. As some Standard Model background will still pass all cuts, this background needs to be understood properly. Data-driven techniques to estimate this background will be described in the next chapter. The analysis aims to be as generic as possible in order to be sensitive to a large

region of SUSY parameters and other models beyond the standard model without loosing sensitivity.

The main difference between the analysis on the data taken in 2010 and this analysis is the strongly increased integrated luminosity by a factor of nearly 50 for most of the analysis. On average, there are also more interactions in one bunch crossing known as pile-up interactions.

6.2 Search Selections

This search starts with a loose baseline selection, where the data itself and the background estimation methods described later can be studied and compared to simulation. On top of this selection there are so called "evolved" selections that focus on the tails of the H_T and $\not{H}_T$ distribution.

6.2.1 Baseline Selection

The baseline selection is defined by the following requirements:

- At least three Particle Flow (PF) jets with $p_T > 50$ GeV and $|\eta| < 2.5$. This cut removes di-jet events and some of the electroweak background. It keeps a good signal efficiency because of the usually long decay chains in supersymmetric events.

- $H_T > 350$ GeV, with H_T defined as the scalar sum of the p_T of all PF jets with $p_T > 50$ GeV and $|\eta| < 2.5$ This cut also reduces electroweak background. As discussed in chapter 3.5 the signal efficiency is high for this cut in most of the parameter space. As this variable is used to trigger the events, it is necessary to cut hard on the offline reconstructed variable to ensure a good trigger efficiency.

- $\not{H}_T > 200$ GeV, with $\not{H}_T$ defined as the magnitude of the vectorial sum of the p_T of all jets with $p_T > 30$ GeV and $|\eta| < 5$. The jet definition is looser compared to the one used for the H_T definition because ignored jets in the region $2.5 < |\eta| < 5.0$ would potentially produce large $\not{H}_T$. This cut

reduces all Standard Model background strongly, especially QCD events. In supersymmetry this momentum imbalance comes from the LSPs.

While $\not\!\!E_T$ shows a better performance than $\not\!\!H_T$, it is not used because the prediction of the QCD background discussed in 7.7.2 can only predict $\not\!\!H_T$, but not $\not\!\!E_T$. Furthermore $\not\!\!H_T$ is more similar to the variable used to trigger the event and it is less affected by pile-up.

- The angle in ϕ between $\not\!\!H_T$ and the leading three jets $|\Delta\phi(J_{1,2},\not\!\!H_T)| > 0.5$ and $|\Delta\phi(J_3,\not\!\!H_T)| > 0.3$, vetoing transverse alignment between one of the first three jets and the vector used to calculate $\not\!\!H_T$ as defined above. This cut is introduced to remove most of the QCD mismeasured events, where $\not\!\!H_T$ aligns to one of the leading jets - mostly the next-to leading jet. The cut on $\Delta\phi$ at 0.5 was chosen to be equal to the jet size used, while the cut at 0.3 was chosen smaller to retain signal efficiency.

- Veto on isolated particle flow muons and electrons. A veto on leptons (e,μ) with loose identification and isolation definition is used to remove most of the $t\bar{t}$ and V+jets events. Global muons, that are reconstructed from a combination of the measurements in the inner tracker and the muon system, are required to have $p_T \geq 10$ GeV and $|\eta| < 2.4$. The tracker and global track needs to be of good quality and to match to the primary vertex within $200\mu m$ transversely and 1 cm longitudinally, and to be isolated. The particle-flow-based relative isolation variable is defined as:

$$\mathrm{Iso}_{\mathrm{rel}} = \frac{p_T^{\pm,had} + e_T^{0,had} + e_T^{0,EM}}{p_T} < 20\%, \tag{6.3}$$

  with $p_T^{\pm,had}$ as the sum of the p_T of all PF charged hadrons in a cone with the Radius $R = 0.3$. Similarly $e_T^{0,had}$ and $e_T^{0,EM}$ are the sum of the p_T of all PF neutral hadrons and photons in the same conus, respectively.

  Electrons similarly should have $p_T \geq 10$ GeV and $|\eta| < 2.5$ (excluding for the position of the superclusters the transition region $1.4442 < |\eta| < 1.566$) and be attached to a good-quality GSF (Gaussian sum filter) track [46]. The cuts on the distance to the primary vertex in the event and the isolation are the same as for muons.

This cut has been tightened compared to the publication on 2010 data [44] as the radius of the isolation cone was decreased from 0.4 to 0.3. This was done because the electroweak background became more important compared to QCD due to the increased cuts on $\not{H}_T$. This radius is also more suitable for the multi-jet environment and the higher pile-up present in data taken in 2011.

If not stated otherwise, distributions shown are for this selection.

6.2.2 Evolved Selections

To be more sensitive within the SUSY parameter space, three evolved search regions are defined. All evolved selections start with the baseline selection. The additional cuts for the three final, overlapping selections are:

(a) Medium H_T & $\not{H}_T$: H_T >500, $\not{H}_T$ >350 GeV

(b) High H_T: H_T >800, $\not{H}_T$ >200 GeV

(c) High H_T & $\not{H}_T$: H_T >800, $\not{H}_T$ >500 GeV

The limits calculated in the analysis are based on these selections because of the much better signal to background ratio, even though the statistical uncertainties of the data driven background estimation methods for these selections are increased compared to the baseline selection. In the final chapters of this thesis a multi-channel limit setting is presented that uses exclusive search regions.

Generally, in the mSUGRA (minimal super gravity) or cMSSM (constraint minimal supersymetric model) described in chapter 3, the selections with high cuts on $\not{H}_T$ are better suited for searches for SUSY with small m_0 and high $m_{1/2}$, because the squark is lighter than the gluino and the squark can decay directely or via a short cascade into the LSP (see Eq. 3.27). In this channel there are few objects that carry the energy and therefore the LSPs are usually more energetic and $\not{H}_T$ is higher. At high m_0 and small $m_{1/2}$, the squark is heavier than the gluino and the gluino decays dominantly via a three body decay into two quarks and the LSP (see Eq. 3.30). More energy is deposited via the quark-jets leading to an on average higher H_T and smaller $\not{H}_T$.

6.3 Triggering and Cleaning of the Data

The analysis is a "hadronic" analysis using only jets. The events are triggered with the H_T-$\not\!\!H_T$ cross-trigger. So far the jets on trigger level are calorimeter jets only, as the Particle Flow reconstruction takes too much time for a trigger decision [1] The use of different jet reconstruction algorithms, different quality cuts and different correction factors lead to differences in the p_T between the trigger level jets and jets produced with a full offline reconstruction. At the trigger level, the calculation of H_T includes jets with corrected jet $p_T > 40$ GeV and $|\eta| < 3$. These jets are required to pass basic quality cuts. Jets with corrected $p_T > 30$ GeV and $|\eta| < 3$ are included in the trigger-level $\not\!\!H_T$ computation. These are not required to pass the quality cuts to avoid fake $\not\!\!H_T$ created by too tight quality cuts, which remove also a fraction of real jets [47]. Due to the strongly increasing instant luminosity in the beginning of data taking in 2011, the trigger-threshold had to be adjusted several times as listed in table 6.1. The total integrated luminosity collected with these triggers adds up to 1.14 fb^{-1}.

To verify that the trigger is still fully efficient, trigger turn-on curves have been calculated. This is shown in Fig. 6.1. While this plot shows a rather soft turn-on due to the different jet reconstruction, it is clearly visible that the baseline selection with $H_T > 350$ GeV and $\not\!\!H_T > 200$ GeV is triggered with full efficiency. The two turn-on curves versus $\not\!\!H_T$ for different run ranges look very similar indicating stability of the trigger efficiency over time.

To find and reject sources of fake $\not\!\!H_T$, standard CMS cleaning procedures are applied and events with high $\not\!\!H_T$ in simulation and data were studied to construct additional filters. The filters listed in the following are used to suppress such events:

- At least one good vertex with the number of degrees of freedom > 4, vertex z-position ≤ 24 cm and radial distance to the beam-pipe $\rho < 2$ cm. This cut removes collisions from displaced satellite bunches and other beam-related background [48].

[1] The use of Particle Flow techniques at trigger level have been studied in detail recently to allow a better reconstruction at trigger level.

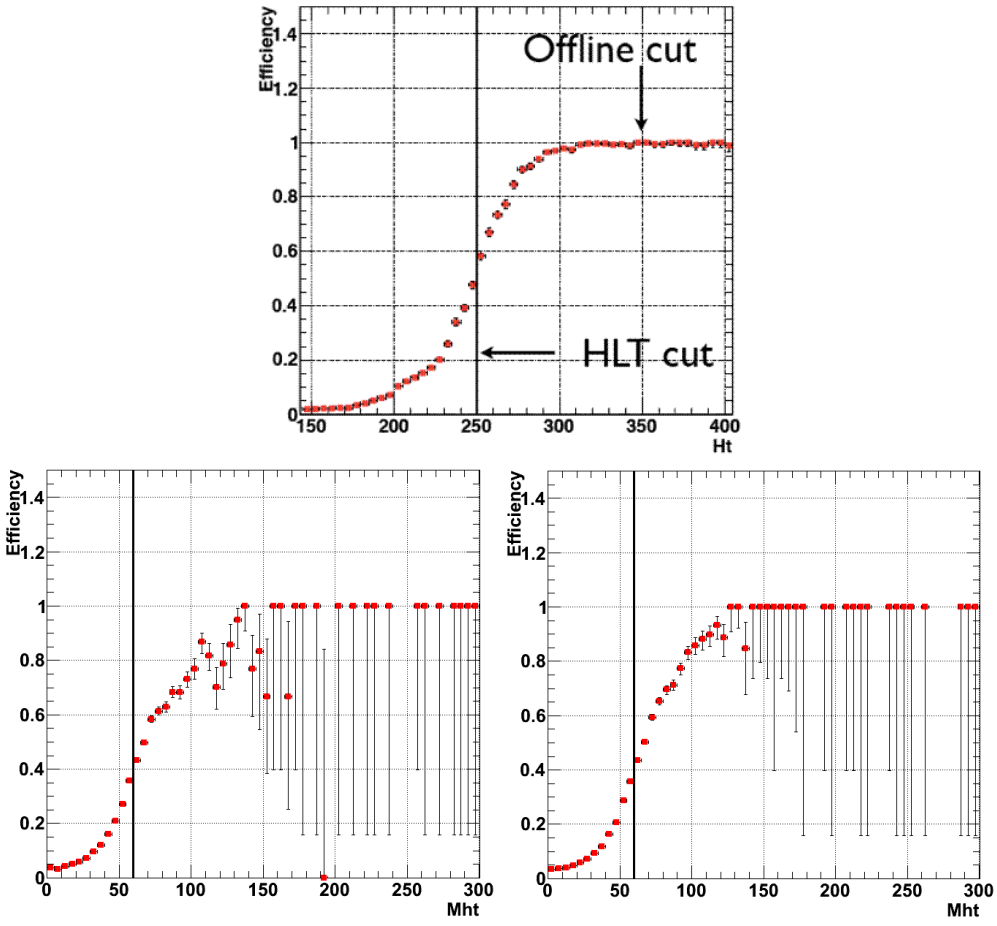

Figure 6.1: The HLT_HT250 trigger efficiency as a function of H_T measured in runs 162803–163261 (top). This efficiency curve is normalized to the HLT_HT150 trigger. The HLT_HT250_MHT60 trigger efficiency as a function of $\not{H}_T$ measured in runs 162803–163261 and 163270–163869, respectively (bottom). This efficiency curve is normalized to the HLT_HT250 trigger. These plots are taken from [47].

Dataset	Run Range	Trigger	Integrated Luminosity $[pb^{-1}]$
/HT/Run2011A-May10ReReco-v1_/AOD	160431-160578	HLT_HT160_v2	< 0.1
/HT/Run2011A-May10ReReco-v1_/AOD	160871-160943	HLT_HT240_v2	0.6
/HT/Run2011A-May10ReReco-v1_/AOD	160955-160956	HLT_HT260_MHT60_v2	0.6
/HT/Run2011A-May10ReReco-v1_/AOD	160957-161176	HLT_HT260_v2	4.9
/HT/Run2011A-May10ReReco-v1_/AOD	161217-163261	HLT_HT250_MHT60_v2	40.8
/HT/Run2011A-May10ReReco-v1_/AOD	163270-163869	HLT_HT250_MHT60_v3	167.8
/HT/Run2011A-PromptReco-v4_/AOD	165088-167151	HLT_HT250_MHT70_v1	138.8
/HT/Run2011A-PromptReco-v4_/AOD	165970-166345	HLT_HT250_MHT70_v3	97.6
/HT/Run2011A-PromptReco-v4_/AOD	166346-166346	HLT_HT250_MHT70_v4	4.26
/HT/Run2011A-PromptReco-v4_/AOD	166347-166967	HLT_HT250_MHT70_v3	420.7
/HT/Run2011A-PromptReco-v4_/AOD	167039-167913	HLT_HT250_MHT90_v1	264.8

Table 6.1: Trigger paths used for selecting the data for different datasets and run ranges. Shown are the run range, the trigger namewith the H_T and $\not{H}_T$ cuts and the integrated luminosity taken with this trigger. The total luminosity adds up to 1.14 fb^{-1}.

- At least 25% of the tracks need to be of high quality, if there are more than ten tracks present. This standard CMS cut [48] removes beam halo events and other background.
- Cut on the aktivity in the ECAL endcap. The number of ECAL endcap Rec Hits [1] "reducedEcalRecHitsEE" is required to be smaller than 2000 to clean events where the ECAL endcap lights up along with correlated noise in the drift tube (DT), the resistive plate chambers (RPC) and/or the cathode strip chamber (CSC) [48].
- The p_T sum over all good tracks divided by the H_T of all jets has to be greater than 0.1. This filter removes events where the tracking algorithm has problems with a too large number of clusters and it also removes events with a large amount of tracks coming from satellite interactions. [48]

[1] The number of ECAL endcap Rec Hits corresponds to the number of cells with an energy above threshold.

- The HBHE noise filter with an isolation-based filter [49] [50] is used. It cuts on the distribution of energy in different HCAL time-slices. As the version of this filter used on the data collected in 2010 was sensitive to out-of-time pile-up, the cuts had to be adjusted to account for the increased pile-up environment.

- The standard CSC beam halo filter [51] is used, which identifies beam halo muons based on information from the cathode strip chamber (CSC).

- Events with large energy in dead or masked ECAL towers are removed. These events can be recognised by using the independent readout of the trigger primitive information or by looking at the energy deposited in the towers neighbouring these towers [31].

- Events with suspicious particle flow muon momenta are removed. This cut does not have a great influence on the selection of the search region as events containing muons are vetoed, but it is important for the selection of the control sample described in the next chapter. The event is removed if:

  - the difference between the momentum calculated with the standard CMS reconstruction and the Particle Flow algorithm differs by more than 100 GeV,
  - the Particle Flow momentum is larger than 100 GeV, while $|\frac{P_T(tracker)}{P_T(global)} - 1| < 0.1$ [48], or
  - the muon is isolated, but still the ECAL and HCAL energy combined is greater than the momentum measured ("greedy muon")

- events are rejected if a jet entering the $\not\!\!H_T$ calculation has more than 95% of its energy in particle flow neutral electromagnetic particles (photons) or more than 90% of its energy in particle flow neutral hadrons. This is done to reject events with cosmic muons, ECAL alignment-laser contamination and ECAL+CSC noise. This filter is referred to as particle based noise rejection (PBNR). As this filter rejects isolated photons the effect of this cut on events with not reconstructed electrons from a W decay, that are discussed in detail

in the next chapter, was studied as they can be reconstructed as photons. It was found that the effect on these events was small.

Filter	Baseline		High HT	High MHT
	Data	LM4	Data	Data
Analysis selection	1078	55862	200	145
HBHENoiseFilter	798	55820	71	18
EENoiseFilter	788	55820	70	17
BeamHaloFilter	757	55820	57	4
TrackingFailureFilter	754	55808	55	3
InconsistentMuonFilter	752	55787	54	2
GreedyMuonFilter	752	55757	54	2
EcalTPFilter	738	55458	53	2
EcalBEFilter	718	54563	51	2
PBNR	706	54114	49	2

Table 6.2: Summary of number of events rejected by various filters at successive stages of the cleaning sequence on data and signal (not normalised SUSY benchmark point LM4 with parameters as defined in Tab. 6.3) events using a subset of about $800 pb^{-1}$ of the full data sample. The analysis selection refers to events with at least one good reconstructed vertex that passes the analysis cuts in addition to the cleaning cut on the good quality of at least 25% of the tracks and the trigger requirements as listed in Table 6.1. This table is taken from [47].

The performance of these filters on data and a SUSY benchmark point are shown in Tab. 6.2. As the absolute number of signal events does not matter here, the signal point is not normalised to the same luminosity as the data. While the signal is hardly affected by these filters leading to a total reduction of about 3%, the events in data are reduced severly. This reduction, that is best visible in the evolved selections, is due to the efficient rejection of beam- and detector-related background, which would criticaly decrease the sensitivity of the analysis .

It has been studied wheter the cut efficiencies have a correlation with $\not\!\!H_T$ for good events. None or only small correlations have been found.

6.4 Comparison of Data and Simulation

In this section a comparison between data and simulation is shown. The aim of this comparison is a qualitative understanding of the data and not the search for a possible excess in data as this will be done in chaper 7.8 using data driven background estimation techniques.

The Monte-Carlo (MC) simulated samples are produced with the Geant [52] [53] CMS detector simulation. They are generated either with the `PYTHIA` [54] or the `MADGRAPH` [55] event generator. As a benchmark for new physics the CMS benchmark point LM4 is used. It models a point in the cMSSM with the parameters shown in table 6.3.

	m_0	$m_{1/2}$	A_0	$\tan\beta$	sign(μ)
Parameter Value	210 GeV	285 GeV	0	10	+

Table 6.3: cMSSM parameters of the CMS benchmark point LM4.

In Tab. 6.4 the event yields of data and the dominant SM MC scaled to an integrated luminosity of $1.14 fb^{-1}$ after several selections are shown. The upper table shows that the sum of these dominant SM processes agrees very well with the data at all stages of the analysis. The yield of other SM processes are at least two orders of magnitude below this background shown. It can be seen that the $\Delta\Phi$-cuts are very effective in reducing the QCD background while the lepton veto reduces a large part of the remaining $t\bar{t}$ and W + jet background. The lower of the two tables shows the same comparison for the evolved selections. It can be seen that the high-$\not\!\!H_T$ selections are nearly QCD free, while it is still an important background for the high-H_T selection. For the baseline selection the other three dominant Standard Model backgrounds $t\bar{t}$, W + jet and $Z \to \nu\bar{\nu}$ have roughly the same size. The benchmark point LM4 shown as signal example is shown to be be clearly visible in this analysis. However, it can also be seen that the agreement between data and MC is getting worse in the tails of the analysis and a simple MC study is not sufficient to archive the sensitivity wanted.

Figure 6.2 shows the H_T, the $\not\!\!H_T$ and the effective mass (M_{eff}) distribution for the baseline selection. The effective mass is a simple scalar sum of the H_T and $\not\!\!H_T$

	Reduced	Reduced $\geq$ 3jets	Reduced $\geq$ 3jets $\Delta\phi$ cuts	Baseline
Data ($1.14 fb^{-1}$)	6377	3408	1640	986
Sum SM MC	6406	3227	1709	987
QCD (PYTHIA 6)	1143	549	11	11
Z $\rightarrow \nu\overline{\nu}$ (MG, $\sigma = 5769$ pb NNLO)	1370	481	387	386
W (MG, $\sigma = 31300$ pb NNLO)	2963	1365	784	346
$t\bar{t}$ (MG, $\sigma = 165$ pb NLO)	930	832	527	244
LM4 (PYTHIA 6, $\sigma = 2.5$ pb NLO)	1477	1179	942	742

	Med-H_T &$\not\!\!H_T$	High-H_T	High-H_T &$\not\!\!H_T$
Data($1.14 fb^{-1}$)	78	70	3
Sum SM MC	95	83	7.5
QCD (PYTHIA 6)	0	7	0.0
Z $\rightarrow \nu\overline{\nu}$ (MG, $\sigma = 5769$ pb NNLO)	46	29	4.2
W (MG, $\sigma = 31300$ pb NNLO)	37	28	2.9
$t\bar{t}$ (MG, $\sigma = 165$ pb NLO)	11	18	0.4
LM4 (PYTHIA 6, $\sigma = 2.5$ pb NLO)	318	304	54

Table 6.4: Event yield in data and simulated samples. The latter are normalized to an integrated luminosity of 1.14 fb^{-1}. The main cross sections used are indicated in the table. All samples were made with the MADGRAPH generator (MG), except for signal samples and the QCD multijets. Reduced stands for cleaning cuts and the H_T and $\not\!\!H_T$ cuts of the baseline selection. The difference between the third and the fourth column of the upper table is the lepton veto in the baseline selection.

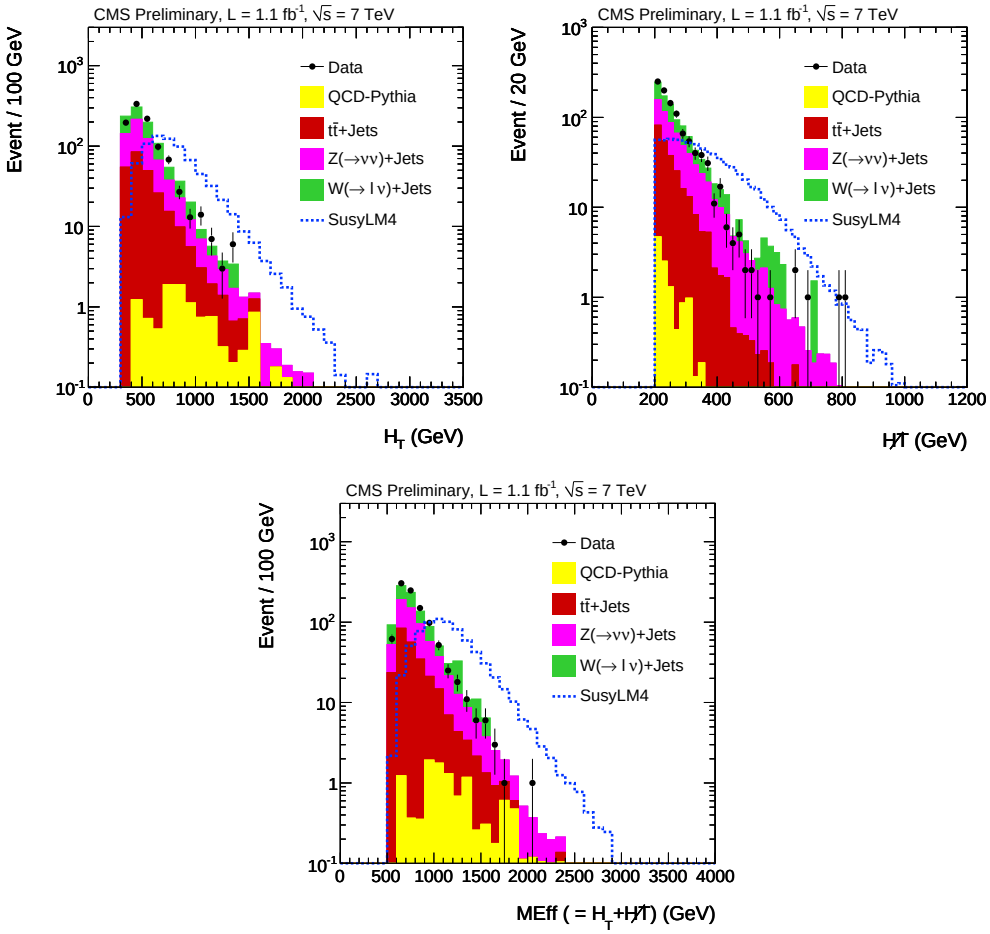

Figure 6.2: Comparison between data and MC after baseline selection. The plots show the $\not{H}_T$ (left) and H_T (right) and effective mass defined as sum of H_T and $\not{H}_T$ distribution (bottom). These plots are taken from [47].

and is a good indication of the combined mass of of the initialy produced SUSY particles, as all visible energy and the energy of the invisible LSPs are taken into account. The comparison of the H_T and $\not{H}_T$ distribution between SM MC and the signal MC visualise the need for the more difficult to predict evolved selections as the SM background decreases much stronger than the signal towards higher values.

These plots confirm that the MC describes the data well except for the outer tails of the distributions where there is more background predicted by simulation than seen in the data. This deficit indicates that the simulation should be handled with care when looking at the tails of distributions. The $\not{H}_T$ distribution of the MC looks not as smooth as expected, indicating a lack of MC statistics in the W-sample. It should also be noted that the expected yields in this special region depend strongly on the generators and the Monte Carlo tunes of the simulation. Therefore, a closer discussion of the difference between data and Standard Model prediction is postponed until the background is estimated with more precision. This will be done in the following chapter with a focus on the $t\bar{t}$ and W + jet background, where the lepton is lost due to acceptance, reconstruction or isolation inefficiencies.

7

Background Studies

7.1 Introduction

In this chapter the data driven background estimation methods are discussed and the results using $1.14 fb^{-1}$ of data is presented. Data driven background estimation methods have been developed for all significant sources of Standard Model background to the search described in the previous chapter. These are QCD, $t\bar{t}$, W + jet and $Z \to \nu\overline{\nu}$ events. The $t\bar{t}$ and W + jet background is estimated together as there is in both cases real $\not\!\!H_T$ from the neutrino of a leptonic W-decay in the event. The lepton veto is passed even though there is a real lepton in the event. These events are divided into those events where the lepton is:

- out of acceptance,
- not reconstructed,
- not isolated,
- a tau lepton that decays hadronically.

The background from the first three items is estimated with the "lost lepton"-method, which is explained in full detail in this thesis, while the contribution from the last item is estimated by the "hadronic tau"-method developed in [56] and taken from there. Events where all W-bosons decay hadronically are no background to the analysis because there is not enough $\not\!\!H_T$ in the events and

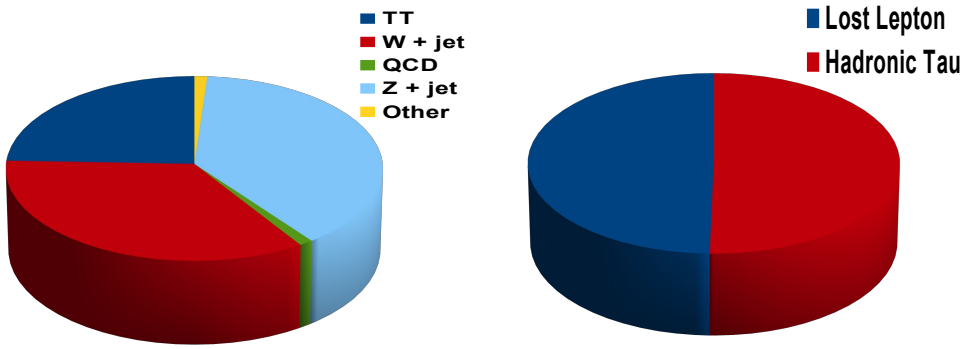

Figure 7.1: The left diagram shows the relative contributions to the background as estimated from MC for the baseline selection. Single top and di-boson production are summerised under "other backgrounds". The right diagram shows the relative contribution of "hadronic tau" and "lost lepton" background from the $t\bar{t}$ and W + jet background.

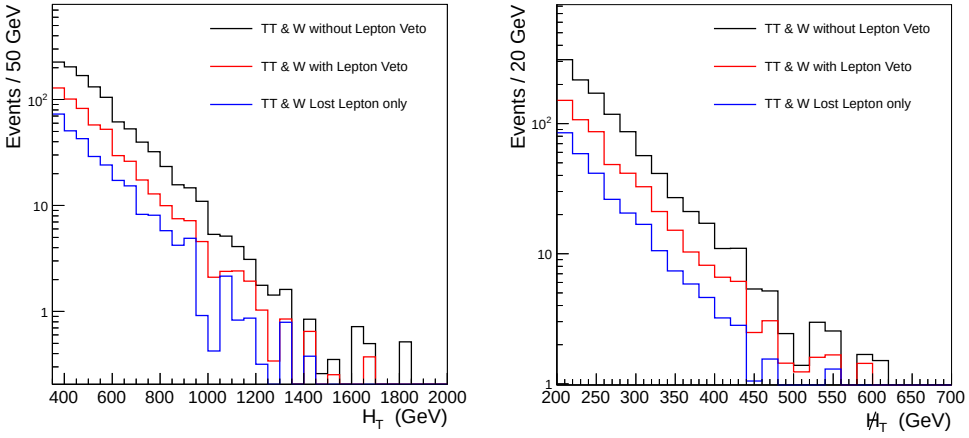

Figure 7.2: The plots show the H_T (left) and $\not{H}_T$ (right) distribution of the $t\bar{t}$ and W + jet background before and after the lepton veto and the contribution of the "lost lepton" background for the baseline selection.

the cut on the $\Delta\phi$ between $\not{H}_T$ and the three leading jets is very efficient against events where the $\not{H}_T$ is produced by jet mismeasurements.

In Fig. 7.1 the relative contributions to the total background is shown as estimated from MC for the baseline selection. The QCD contribution is very small in this selection, but the uncertainties in the simulation are larger compared to the other background contributions and QCD is an important background for the high H_T selection. Therefore a good estimation of the QCD background is still very important. The $t\bar{t}$ and W + jet background together contribute about 60% to the total background. It can be seen from the figure on the right hand side that the contributions from "hadronic tau" and "lost lepton" to this background have about the same size. In Fig 7.2 the H_T and $\not{H}_T$ distribution of the $t\bar{t}$ and W + jet background before and after the lepton veto and the contribution of the "lost lepton" background is shown for the baseline selection. It can be seen that the lepton veto is efficient over the whole kinematic range and that the relative contribution of the "lost lepton" background is independent of H_T and $\not{H}_T$.

For the QCD background only the "rebalance and smear"-method taken from [57] is described shortly at the end of the chapter, as the "factorisation"-method [58] is only available for parts of the dataset and was used as a cross check. Also for the $Z \to \nu\overline{\nu}$ background there are several methods available, but only one of them is suited for the small statistics in the evolved selections. In this thesis only this method using the similarities between Z-bosons and photons at high boson p_T taken from [59] is used [1]. It will also be discussed at the end of the chapter in a compact way.

7.2 The Lost Lepton Method

The aim of this method is to estimate all Standard Model background where significant $\not{H}_T$ originates from a neutrino from a W-boson decay and where the associated lepton is either an electron, muon or a tau that decays leptonically. The separation between $t\bar{t}$ and W + jet is avoided and therefore uncertainties associated with their experimental separation do not arise.

[1] In the future it is planned to use a combination of these methods to estimate this background

7.2.1 Properties of the Background Events

This background is dominated by semileptonic $t\bar{t}$ and leptonic W + jet events. W decays to a τ-lepton that decays hadronically are not counted as leptonic decays in the following. Di-leptonic $t\bar{t}$ events with two real light leptons (electrons or muons) in the final state contribute to this background by about 2.5 % in the baseline selection. Another even smaller contribution to the estimated background comes from diboson events where at least one boson is a W-boson and single tops.

	$t\bar{t}$		W+jets	
	electron	muon	electron	muon
not reconstructed	1.3	0.6	2.3	0.8
not isolated	1.1	1.2	1.0	1.3
out of acceptance	3.1	2.8	5.2	4.9
total	5.6	4.6	8.5	7.0

Table 7.1: Contributions to the total background of the baseline selection from $t\bar{t}$ and from W+jets in MADGRAPH MC for 100/pb. The rare di-leptonic events with one electron and one muon show up in both columns.

The background is divided into those events where the lepton is out of detector acceptance, not reconstructed or not isolated. The contribution of the different classes to the background to be estimated are given in table 7.1 as predicted by the sample generated with MADGRAPH and the Z2 tune [1]. Events where the lepton is a tau that decays to a muon or an electron are included in the muon and electron group, respectively. These events are more important than expected by the branching ratio as the additional neutrino increases the $\not\!\!H_T$ while the final lepton is usually soft so that it is more likely to drop out of detector acceptance.

The relative importance of not isolated leptons decreased compared to the publication [44] because the radius of isolation cone also decreased from 0.4 to

[1] This dataset describes the data collected from electroweak processes best and is recommended by the electroweak working group

0.3 [1]. This smaller radius is more suited for this multi-jet environment and shows less dependence on pile-up.

7.2.2 Calculating the Prediction

7.2.2.1 Overview

As the lepton veto is an very efficient cut against the background described above, the basic idea of this method is to invert the lepton veto. Therefore, a control sample is constructed with the same cuts, cleaning and triggering as defined in Ch. 6 except for the inverted criteria of one well isolated and identified muon. The muon in the control sample is defined in the same way as the vetoed muons in Ch 6. A closer look at the control sample in data and the introduction of additional cuts against signal contamination is postponed to 7.2.2.2.

Starting from the muon control sample, the background due to lost electrons or muons is determined as sketched in Fig. 7.3 for the example of background due to lost muons. For this determination the isolation efficiency (ϵ_{ISO}), the identification efficiency (ϵ_{ID}) and the acceptance efficiency (ϵ_{Acc}) as defined below are used. The isolation and identification cuts are described in Ch. 6.

$$\epsilon_{\mathrm{ISO}} = \frac{\text{number of reconstructed leptons passing iso and id cuts}}{\text{number of reconstructed leptons passing id cuts}} \tag{7.1}$$

$$\epsilon_{\mathrm{ID}} = \frac{\text{number of reconstructed leptons passing id cuts}}{\text{number of leptons in } p_T \text{ and } \eta \text{ detector acceptance}} \tag{7.2}$$

$$\epsilon_{\mathrm{Acc}} = \frac{\text{number of leptons in } p_T \text{ and } \eta \text{ detector acceptance}}{\text{all leptons}} \tag{7.3}$$

As the number of events in the control sample (CS) corresponds to the numerator in Eq. 7.1 for muons, the number of events with muons that pass all cuts except for the isolation (!ISO$^{\mu}$) can be calculated with the following formula:

[1] W + jet MC is quite sensetive to changes in the generator tunes. Older MC samples showed far less events in the baseline selection. The $t\bar{t}$ prediction did not change much, although the amount of not reconstructed leptons was smaller.

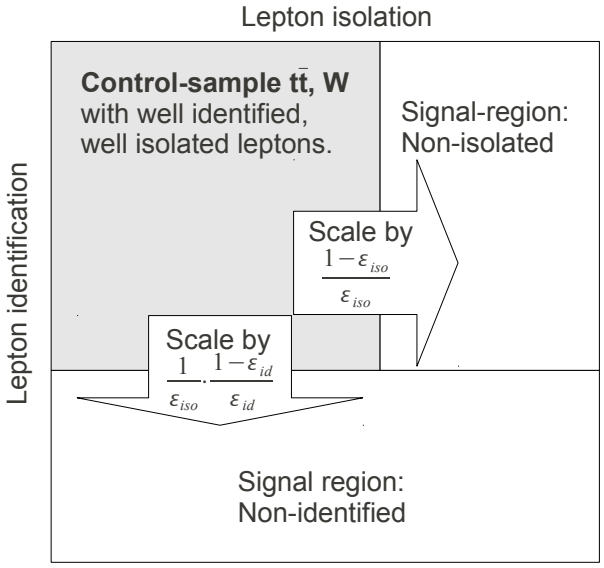

Figure 7.3: Sketch of the lost lepton method for the W + jet and $t\bar{t}$ background.

$$\begin{aligned} !\mathrm{ISO}^{\mu} &= \text{muons passing id cuts} - \text{muons passing iso and id cuts} \\ &= \text{muons passing id cuts} \cdot (1 - \epsilon^{\mu}_{\mathrm{ISO}}) \\ &= \mathrm{CS} \cdot \frac{1 - \epsilon^{\mu}_{\mathrm{ISO}}}{\epsilon^{\mu}_{\mathrm{ISO}}} \end{aligned} \tag{7.4}$$

The number of events with non-reconstructed muons ($!\mathrm{ID}^{\mu}$) can be calculated in a similar way:

$$\begin{aligned} !\mathrm{ID}^{\mu} &= \text{muons in } p_T \text{ and } \eta \text{ detector acceptance} - \text{muons passing id cuts} \\ &= \text{muons in } p_T \text{ and } \eta \text{ detector acceptance} \cdot (1 - \epsilon^{\mu}_{\mathrm{ID}}) \\ &= \mathrm{CS} \cdot \frac{1 - \epsilon^{\mu}_{\mathrm{ID}}}{\epsilon^{\mu}_{\mathrm{ID}} \cdot \epsilon^{\mu}_{\mathrm{ISO}}} \end{aligned} \tag{7.5}$$

The number of muons out of p_T and η detector acceptance ($!\mathrm{Acc}^{\mu}$) is given by:

$$\begin{aligned} !\mathrm{Acc}^{\mu} &= \text{all muons} - \text{muons in } p_T \text{ and } \eta \text{ detector acceptance} \\ &= \text{all muons} \cdot (1 - \epsilon^{\mu}_{\mathrm{Acc}}) \\ &= \mathrm{CS} \cdot \frac{1 - \epsilon^{\mu}_{\mathrm{Acc}}}{\epsilon^{\mu}_{\mathrm{Acc}} \cdot \epsilon^{\mu}_{\mathrm{ID}} \cdot \epsilon^{\mu}_{\mathrm{ISO}}} \end{aligned} \tag{7.6}$$

In Eq. 7.6 is has been used that the number of all muon events can be written as:

$$\text{all muons} = \frac{\mathrm{CS}}{\epsilon^{\mu}_{\mathrm{Acc}} \cdot \epsilon^{\mu}_{\mathrm{ID}} \cdot \epsilon^{\mu}_{\mathrm{ISO}}} \tag{7.7}$$

Due to lepton universality the total number of events with muons is the same as the number of events with electrons. With this assumption the number of events with lost electrons can be calculated from the muon control sample. The formula used to calculate the contribution of non-isolated electrons ($!\mathrm{ISO}^{\mathrm{e}}$), non-reconstructed electrons ($!\mathrm{ID}^{\mathrm{e}}$) and electrons out of acceptance ($!\mathrm{Acc}^{\mathrm{e}}$) are given below:

$$\begin{aligned} !\mathrm{Acc}^{\mathrm{e}} &= \text{all electrons} \cdot (1 - \epsilon^{e}_{\mathrm{Acc}}) \\ &= \mathrm{CS} \cdot \frac{1}{\epsilon^{\mu}_{\mathrm{ISO}}} \cdot \frac{1}{\epsilon^{\mu}_{\mathrm{ID}}} \cdot \frac{1 - \epsilon^{e}_{Acc}}{\epsilon^{\mu}_{Acc}} \end{aligned} \tag{7.8}$$

$$!\mathrm{ID}^{\mathrm{e}} = \mathrm{CS} \cdot \frac{1}{\epsilon^{\mu}_{\mathrm{ISO}}} \cdot \frac{1 - \epsilon^{e}_{\mathrm{ID}}}{\epsilon^{\mu}_{\mathrm{ID}}} \cdot \frac{\epsilon^{e}_{Acc}}{\epsilon^{\mu}_{Acc}} \tag{7.9}$$

$$!\mathrm{ISO}^{\mathrm{e}} = \mathrm{CS} \cdot \frac{1 - \epsilon^{e}_{\mathrm{ISO}}}{\epsilon^{\mu}_{\mathrm{ISO}}} \cdot \frac{\epsilon^{e}_{ID}}{\epsilon^{\mu}_{ID}} \cdot \frac{\epsilon^{e}_{Acc}}{\epsilon^{\mu}_{Acc}} \tag{7.10}$$

The sum over all six background contributions make up the total background due to lost leptons. The only additional correction factors that need to be taken into account is a correction because of the cut against signal contamination discussed in section 7.2.2.2, a small correction factor for di-leptonic events discussed in section 7.2.3 and a correction factor due to kinematical differences between the $t\bar{t}$, W + jet and the Z-sample influencing the reconstruction efficiency as discussed in section 7.4.2.

In the following details about the control sample and the background contributions are given before the "Tag & Probe"-method, that is used to determine the efficiencies, is discussed in detail. The method is then tested on simulation and applied to data.

7.2.2.2 The Control Sample

In this section the control sample used in the "lost lepton"-method is studied, and possible contamination due to other Standard Model processes or signal events are discussed.

The muon control sample is defined by the same trigger requirements, cleaning and search cuts as defined in Ch. 6, expect for exactly one well isolated and identified muon. This muon is defined in the same way as the vetoed muons in 6. In principle, also a control sample with an electron instead of the muon could be used, which would roughly double the statistic of the control sample, but electrons are much more likely to be faked by photons and jets, leading to a severe problem with contamination of the control sample. One could tighten the electron definition to reduce this problem, but the possibility of fake electrons cannot be eliminated. Their number would be difficult to estimate and thus new uncertainties would be introduced. Tight quality cuts on the electron would also reduce the electron control sample and therefore reduce the gain in statistics. As will be discussed later, the uncertainties on the isolation- and identification-efficiencies are larger for the electrons than for the muons, which also favours the use of the muon control sample. These facts have led to the decision to drop the use of the electron control sample.

In Fig. 7.4 the comparison between data and MC for $1.14 fb^{-1}$ is shown. A good agreement in the shape of all distributions can be observed, and even though slightly less events are seen in data than expected from MC, this difference is covered by statistical and systematic uncertainties. The systematic uncertainties taken into account for the simulation are the uncertainties on the luminosity and the jet energy scale. The MC used was reweighted to agree with the shape of the primary vertex distribution of the data before all cuts. It can be seen that there is still a good agreement for the control sample of the baseline selection. The ΔR

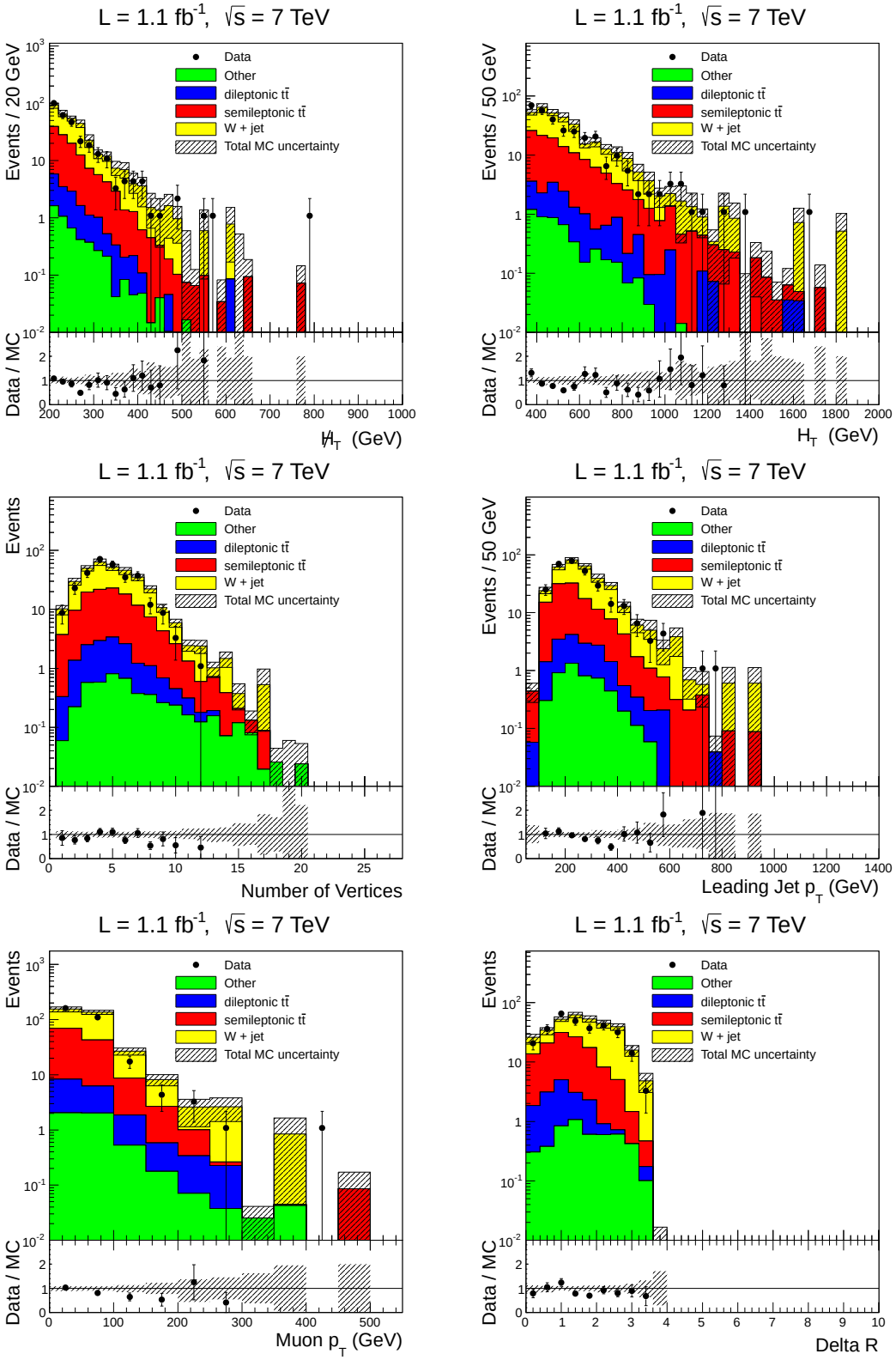

Figure 7.4: Comparison between data and MC for the control sample after baseline selection for $1.14 fb^{-1}$. The distributions shown are: $\not{H}_T$ (upper left), H_T (upper right), number of primary vertices (middle left), leading jet p_T (middle right), muon p_T (lower left) and ΔR between lepton and jet as used for the isolation parametrisation (lower right).

distribution decreases towards low values not only because of the smaller area per bin, but also because only isolated leptons are shown and only few leptons closer to a jet pass the isolation requirement in Eq. 6.3. The isolation efficiency in dependence on event kinematics will be discussed in more detail in the following sections.

Contamination of the Control Sample

The control sample and the background to be predicted consist of about the same mix of events, i.e. it is dominated by semileptonic $t\bar{t}$ and W + jet events. As discussed above for the background events there is also a contribution of di-leptonic $t\bar{t}$ events and a small contribution of single top and some di-boson events. Di-boson events are mostly WW events. The single top and di-boson events each make up less than 1 % of the control sample due to the much smaller cross section and because there are less jets in single top events compared to $t\bar{t}$ events. This contribution is also shown in Fig. 7.4. As these can be used to predict the single top and di-boson contribution to the background no additional correction is needed.

There can also be non-W Standard Model background in this control sample as for example from QCD- or Z-events. Monte Carlo studies suggest that no such events pass the hard cuts of the baseline control sample for the luminosity considered, as QCD and leptonic Z-events are unlikely to produce sufficient $\not\!\!H_T$ to pass the hard $\not\!\!H_T$- and $\Delta\Phi$-cuts. QCD is further suppressed by the muon requirement.

Z-events that decay into two neutrinos do not contain a muon and are unlikely to produce enough high energetic jets. This contribution is therefore negligible for the control sample. Z-events with a decay into two tau-leptons, where one tau decays into a muon and two neutrinos is the only possible contribution without severe mismeasurement, but due to the small branching ratio and the steeply falling H_T- and $\not\!\!H_T$-spectrum, this contribution is very small.

Especially for QCD, the statistics of a simple MC study is not considered to be sufficient to rule out the possibility of Standard Model contamination.

Therefore, a 3% systematic uncertainty is atributed to SM contamination of the control sample. This value is conservatively estimated from the contamination of the control sample due to a muon enriched QCD-sample and a Z-sample for a reduced baseline selection. It is one of the smaller uncertainties of the method.

Signal Contamination

In large areas of the SUSY parameter space there can be leptons produced in the decay chain of supersymmetric particles. This can either be due to decaying sleptons or due to leptonically decaying bosons. To distinguish these events from the $t\bar{t}$ and W + jet events, the sources of the $\not\!\!E_T$ is studied. In $t\bar{t}$ and W + jet events the neutrino is the dominant source, while in SUSY-events a large part of $\not\!\!E_T$ will come from the two LSPs. [1]

In Standard Model events, where the $\not\!\!E_T$ originates from the neutrino from the W-decay, the transverse mass of the combination of the lepton and $\not\!\!E_T$ defined as:

$$m_T = \sqrt{2P_{T,\mu} \cdot \not\!\!E_T \cdot (1 - \cos(\Delta\Phi))} \tag{7.11}$$

corresponds to the transverse W-mass distribution, which peaks around the W-mass of 80.4 GeV and decreases strongly towards higher values. $\Delta\Phi$ is the distance in Φ between the muon and $\not\!\!E_T$. To gain from the better performance, $\not\!\!E_T$ defined as the negative vectorial sum of the momentum of all particle flow particles is used instead of $\not\!\!H_T$.

The transverse mass distribution is shown in Fig. 7.5. In di-leptonic $t\bar{t}$ events the $\not\!\!E_T$ originates from two neutrinos. Therefore these events contribute to the tail at $m_T > 80$ GeV. Leptonically decaying tau leptons also show a slightly different behaviour compared to events where the muon comes directly from the W-decay because the momentum of the neutrinos can to some extend cancel in the calculation of $\not\!\!E_T$, leading to slightly smaller values. However, these τ-events have a small impact on the m_T distribution.

For SUSY-events with $\not\!\!E_T$ from at least two LSPs this distribution does not correspond to a mass and is therefore very broad. To reduce signal contamination

[1] R-parity violation models are not studied as the results are only interpreted within the cMSSM, where R-parity is conserved.

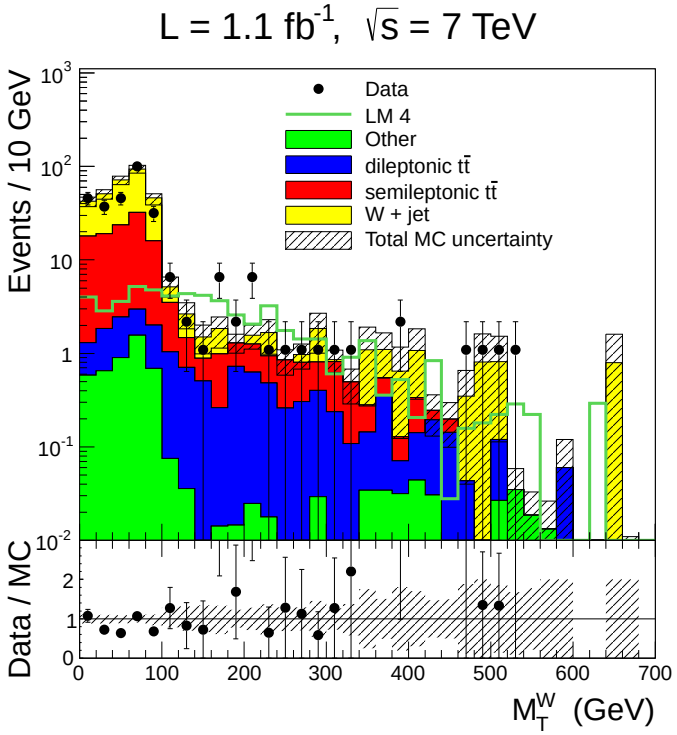

Figure 7.5: Comparison of the transverse mass distribution as defined in Eq. 7.11 between data and MC for the control sample after baseline selection for $1.14 fb^{-1}$. The signal benchmark point LM4 is shown for comparison.

the requirement $m_T < 100$ GeV is introduced for the control sample. The SM contribution removed by this cut is in the MC 10.5% of the remaining control sample. To account for this cut the final prediction on data is corrected by the factor f_{m_T-cut}:

$$f_{m_T-cut} = \frac{\text{all events in control sample}}{\text{events in control sample with } m_T < 100\text{GeV}} = 1.105. \qquad (7.12)$$

The cut-value is motivated purely by the well known physics of the Standard Model with an increase from the W-mass to 100 GeV due to detector resolution effects. No assumption on the physics beyond the Standard Model is made except for the existence of two LSPs, or any other source of $\not{E}_T$, and this assumption was already used when designing the search cuts of the analysis. Therefore, no loss in generality is introduced.

The effect of this cut on the signal contamination from SUSY events is parameter dependent. For LM4 the contamination is reduced by about 50% in the baseline selection. However, for the evolved selections this cut improves the situation more than naively expected. While this variable is a physical quantity for semileponic $t\bar{t}$ and W + jet events with little correlation to other kinematic quantities, the momentum of a muon and the $\not\!\!E_T$ in SUSY events is of a different physics orgin and therefore to a large extend uncorrelated leading to a correlation between m_T and $\not\!\!E_T$. This leads to the fact that the reduction grows to about 75% for LM4 for the high $\not\!\!H_T$ selection.

To calculate the uncertainty due to this cut, several sources are considered. Di-Leptonic events make up about 23% of the events with a $M_T > 100$ GeV. Large variations of the di-leptonic contribution of 40% do not change the relative contribution of events above the cut, i.e. $1-_{m_T-cut}$, by more than 10%. Even though the di-leptonic contribution is known with a high precision, this is conservatively taken as systematic uncertainty. To calculate the uncertainty due to $\not\!\!E_T$ mismeasurements the $\not\!\!E_T$ is varied by 10% and the effect on f_{m_T-cut} is included as systematic uncertainty. The possibility of non-gaussian $\not\!\!E_T$ mismeasurements is very difficult to estimate precisely, so a conservative estimate of 30% on the relative contribution of events above the cut is attributed to this source. Combined, this conservative estimation yields an uncertainty of 39% on $1 - f_{m_T-cut}$. This uncertainty plays a minor role compared to other uncertainties.

7.2.2.3 Non-isolated Leptons

The relative importance of events passing the lepton veto because the lepton is not isolated is larger for $t\bar{t}$ than for W + jet events, as can be seen from table 7.1. The reason for this is not only that there are usually more jets in $t\bar{t}$ events than in W + jet events, but also the kinematics in these events. While in W + jet events the jets are dominantly produced opposite in Φ to the W-boson, the top-quark decays into a W-boson and a b-quark. If the top-quark is strongly boosted, which is enhanced by the cuts on H_T and $\not\!\!H_T$, the b-jet and the W-boson are emitted close to each other in the detector. Therefore, also the lepton tends to be close to the b-jet and is less likely to be isolated than in W + jet events.

The isolation efficiencies between $t\bar{t}$ and Z-events, on which the efficiencies are determined, are not expected to be identical for similar reasons as for the difference between $t\bar{t}$ and W + jet events discussed above. Here the difference is even larger because there are no requirements on the hadronic environment for the Z-sample. While the muon MC isolation efficiency in the $t\bar{t}$ and W + jet sample after the baseline selection without the lepton veto is 89.9 % and 93.3 %, respectively it is 96.6 % on a Z-sample. The error of using a plain number for the isolation efficiency in Eq. 7.4 and Eq. 7.10 to estimate the events with non-isolated leptons would therefore be very large.
The proximity between leptons and jets is responsible for this difference. Therefore, this efficiency is parametrised not only in terms of the p_T of the lepton, which is CMS standard, but also as a function of $\Delta R = \sqrt{\Delta\Phi^2 + \Delta\eta^2}$ between the lepton and the closest jet with a transverse momentum of at least 30 GeV. More details on the efficiency calculation, parametrisation and the effect of the different kinematics are given in the next section 7.3.

7.2.2.4 Non-reconstructed Leptons

The events with non-reconstructed leptons or with leptons that do not pass the Id-cuts are estimated with Eq. 7.5 and Eq. 7.9. While muons are reconstructed with a very high efficiency, as was discussed in chapter 4.2, electrons do not have such a clean signature and they are not reconstructed with such a high efficiency. This is why events with not reconstructed electrons contribute much more to the background than events with not reconstructed muons. This can also be seen in table 7.1.

Also the reconstruction efficiency depends on the event kinematics and is therefore sample dependent. However, this dependence is much smaller than for the isolation. As the reconstruction efficiency cannot be parametrised in the same way as the isolation efficiency this effect is corrected for as will be discussed in chapter 7.4.2.

7.2.2.5 Leptons out of Detector Acceptance

The largest contribution of events that pass the lepton veto even though there is a real lepton in the events comes from leptons out of the detector acceptance. This is the case if the lepton has a $p_T < 10$ GeV or because the lepton is emitted too close to the beam axis. The second contribution is about a factor of three smaller than the first for the $t\bar{t}$ and W + jet processes.

As leptons out of η acceptance are not measured at all and leptons below the p_T threshold are only reconstructed with a bad efficiency that is also not known with a high precision, the background from leptons out of detector acceptance must be estimated with MC simulations. It has been discussed before that the use of pure MC estimations is not sufficient. As the spectrum of the leptons is known more reliable than the number of events in the tail of the H_T and $\not{H}_T$ distribution, only the efficiency of leptons being in detector acceptance is taken from MC and the muon control sample can be reweighted accordingly to model this kind of background. Apart from the p_T-spectrum there is a dependence on the $|\eta|$-spectrum and to a small extend on the ratio between $t\bar{t}$ and $W+jet$ events in the background, as the spectrum is slightly different for each. The estimation of events with leptons out of acceptance is defined in Eq. 7.6 and Eq. 7.8. The acceptance efficiency used in these equations is determined on a combination of $t\bar{t}$ and W + jet events.

While the kinematics of leptons in $t\bar{t}$ events show no significant charge dependence, W-bosons are preferably polarised left-handed along their flight [16] direction due to the left-handed nature of the weak force discussed in chapter 2.2.3.Therefore positively charged leptons are preferably emitted opposite to the direction of flight, while the neutrino is preferably emitted in direction of flight leading to larger $\not{H}_T$. This leads to about four times as many positively charged leptons in W + jet events as negatively charged leptons after the the baseline cut on $\not{H}_T$. This dependence is not used in this analysis, but might become useful in future updates of the analysis - especially if there is a separation between $t\bar{t}$ and W + jet events, e.g. by making a b-tag and non-b-tag selection to improve the sensitivity for searches with third generation particles in the decay chain [1].

[1] This is a likely development for future updates of the analysis, as the hierarchy problem

Generally, the acceptance efficiency depends on the transverse boost of the W-boson and is therefore positively correlated with $\not{H}_T$. This correlation is strong for low $\not{H}_T$ values below the baseline cut. Above $\not{H}_T = 150$ GeV the dependence of the acceptance efficiency on $\not{H}_T$ is very small and is in fact compatible with a constant efficiency for the statistics of the MC samples available. The same acceptance efficiency is therefore used for all selections. [1]

Jet Multiplicity

Leptons are clustered into jets with the particle flow algorithm. The distribution of the p_T of the leptons in the control sample peaks around 50 GeV, i.e. close to the jet threshold. Therefore, about half of the control sample has one more jet than the background to be predicted. The absolute number of predicted events is still determined correctly by the way the acceptance efficiency is calculated: First, all cuts except the lepton veto are applied on a simulated MC sample. Then, the efficiency is taken as the fraction of the generated leptons that are inside the detector acceptance. Therefore, no additional calculation is needed for the events where a transition from a "$n+1$"-jets to a "n"-jet sample would be necessary. However, there can be an effect on the H_T- and $\not{H}_T$-spectra. The effect on the $\not{H}_T$ distribution is small, as the effect on the neutrino p_T is small and removing this additional jet would artificially introduce $\not{H}_T$ in the event.

The effect on the H_T spectrum is in general also small, however, for low H_T values near the baseline cut of 350 GeV the different jet spectra together with the cut on the number of jets lead to a small underprediction, which is visible in the lowest H_T bin in the closure test discussed later. The analysis of the full data taken in 2011 uses already a baseline cut on H_T of 500 GeV, well above of where a difference in shape can be observed. It has been checked that these effects on the H_T spectrum do not change the acceptance efficiency for the different selections significantly.

hints to stop masses that are not too heavy

[1] As soon as higher statistics MC samples are available, this assumption should be checked again .

7.2.3 Correction for Dileptonic Events

Dileptonic events from $t\bar{t}$ or di-boson events make up about 3% of the control sample in the simulation. They enter the control sample if one lepton is lost. As each of the leptons can be lost and because the likelihood of one lepton being lost is in good approximation independent of the second lepton, dileptonic events make up twice the fraction in the control sample as in the background to be predicted. This leads to an overprediction of about 1.5%. Therefore the predicted background is corrected with the factor 0.985. The contribution is small, because the cut against signal contamination discussed in section 7.2.2.2 removes more dileptonic $t\bar{t}$ events compared to semileptonic $t\bar{t}$ or W + jet events. Without that cut the contribution of dileptonic events would be about 5%.

7.3 Lepton Efficiencies

In this section the lepton efficiencies are discussed in more detail. First the "tag & probe"-method [60] on the Z-resonance is discussed, which is used to determine the lepton efficiencies on data. The lepton efficiencies are factorised into identification efficiency and isolation efficiency, where the latter will depend much stronger on the hadronic activity in the event. Then these efficiencies are compared to expectations obtained from the simulation.

7.3.1 Tag & Probe Method

To determine an efficiency, it is important to know if a reconstructed lepton is a real, physical lepton without applying cuts on the properties of the lepton, as the efficiencies of these cuts are the subject of the study. Therefore, a well known physical process is used that can be cleanly identified without applying cuts to the lepton under study. In this thesis the processes $Z \to ee$- and $Z \to \mu\mu$ are used as the kinematical properties of the leptons cover the region of interest. Other resonances that decay into two leptons, such as the J/Ψ, can in principle be used as well.

A well identified tag-lepton is used to trigger the event. This lepton is required to have a transverse momentum of at least 20 GeV and needs to be isolated in

the same way as defined in the chapter 6, i.e. the sum of the p_T of all particles reconstructed with the particle flow algorithm in a cone with radius $\Delta R = 0.3$ around the lepton should not exceed 20% of the p_T of the lepton. Furthermore, the lepton needs to pass tight quality cuts. These cuts are in place to make sure that this lepton is a real, prompt lepton.

This tag-lepton also has to fire the trigger to leave possible other leptons in the event completely unbiased. The requirements on the tag-lepton from the trigger side should not influence the probe measurements. This is the reason why no dilepton triggers can be used. Cross-trigger with requirements on the hadronic activity are unproblematic, as these conditions are closer to the properties of the events considered in the background prediction. As instant luminosity and trigger threshold increase, the Z-sample is suited better to calculate efficiencies for a multi-jet environment. The triggers used for the matching between the tag-lepton and the lepton from trigger information are all single muon triggers for the muon efficiencies. The cut on the muon at trigger level increased from 9 GeV to 40 GeV with increasing instant luminosity. In the later runs, the triggering muon also was required to be isolated at trigger level.

Similarly for the tag-electron all single electron triggers are used. With increasing instant luminosities the electron needs not only to be isolated, but there also has to be some additional energy in the event to trigger the event. This is called an electron-H_T cross-trigger that requires an H_T trigger, similar to the one described in Ch. 6 but with much reduced thresholds, to fire in addition to the electron trigger. [1]

In the next step a probe-lepton is selected with very loose quality cuts. These probe-leptons are different for each efficiency and will be defined in the according section. If such a probe-lepton can be found, the energy-momentum vectors of the tag- and the probe-lepton are combined to form the mass of the assumed Z-boson. Only events where the mass is between 60 GeV and 120 GeV for muons

[1] As the trigger thresholds increase above the offline cuts on the tag-lepton, a higher fraction of Z-events is rejected with increasing instant luminosity, and therefore a slight shift of the pile-up distribution towards lower values is introduced. However, it has been shown that this effect is negligible for the data discussed and it is not necessary to tighten the cuts on the tag-lepton, which would lead to an increased statistical uncertainty.

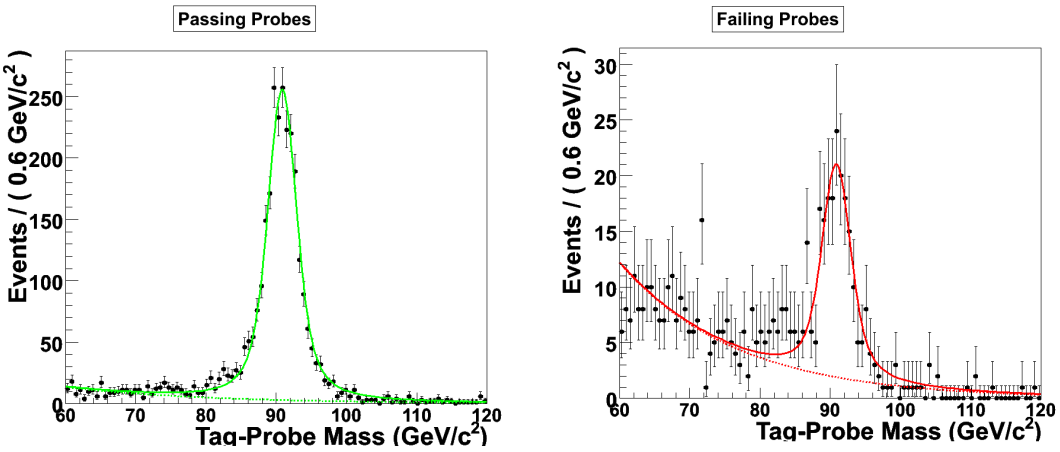

Figure 7.6: Z-boson mass as combination of the tag- and the probe-lepton for events where the probe is passing (left) and failing (right) the test criterion for the muon isolation on an example bin for $880pb^{-1}$ of data.

and 70 GeV and 110 GeV for electrons are kept. These events are divided into two groups, depending on the probe-lepton passing or failing the test criterion for which the efficiency is calculated. For isolation efficiencies this criterion is for example passed if the lepton is isolated. Such distributions can be found in figure 7.6.

To each of these distributions a fit is performed with a signal and a background component. The functional form of the signal is a "Voigtian", which is a Gaussian convoluted with a Breit-Wigner function. The background can either be modeled with an exponential function or a second order Chebychev polynomial. As the Chebychev polynomial did not converge properly in some bins, the exponential function is used. An example of such a fit can also be seen in figure 7.6.

The efficiency is taken as the integral of the Voigtian of the events where the probe-lepton passes the test criterion divided by the sum of the integrals of the Voigtians for passing and failing test probes. The uncertainty of the fit is propagated as a systematic uncertainty on the efficiency. As this uncertainty depends strongly on the statistics in the fit region this uncertainty has decreased significantly compared to the analysis on 36pb^{-1} of data, and it is expected to reduce even further with increasing integrated luminosity.

7.3.2 Lepton Identification Efficiency

The global identification efficiency ϵ_{ID} is a product of all sub-efficiencies:

$$\epsilon^{e}_{ID} = \epsilon^{e}_{Gsf} \cdot \epsilon^{e}_{\text{ID cuts}} \quad (7.13)$$

$$\epsilon^{\mu}_{ID} = \epsilon^{\mu}_{\text{global}} \cdot \epsilon^{\mu}_{\text{ID cuts}} \quad (7.14)$$

$$\epsilon^{\mu}_{\text{global}} = \epsilon^{\mu}_{\text{tracking}} \cdot \epsilon^{\mu}_{\text{standalone}} \quad (7.15)$$

The electron sub-efficiencies are the efficiency ϵ_{Gsf} that a super cluster with $P_T > 10$ GeV can be matched to a Gsf-electron and the efficiency $\epsilon_{\text{ID cuts}}$ that the electron passes the ID cuts used in this analysis. These superclusters are cleaned from jets with hadronic fractions above 15% to reduce the background from jets to the superclusters. Even with this cut the sample for this this sub-efficiency has by far the largest background leading to an increased uncertainty, especially for the low p_T bins. The superclusters in the transition region $1.4442 < |\eta| < 1.566$ are excluded in the same way as for the whole analysis described in Ch. 6.

For muons, ϵ^{μ}_{ID} is the product of the efficiency $\epsilon^{\mu}_{tracking}$ that a standalone muon can be matched to a global muon, the efficiency $\epsilon_{standalone}$ that a track can be matched to a global muon and the efficiency $\epsilon_{\text{ID cuts}}$ that the muon passes the ID cuts. The definitions and passing-criteria to acquire these efficiencies are summarised in Tab. 7.2.

Efficiency	definition of the probe lepton	passing-criterion for the probe
ϵ^{e}_{Gsf}	Super Cluster $P_T > 10$ GeV	Gsf Electron
$\epsilon^{e}_{\text{ID cuts}}$	Gsf Electron $P_T > 10$ GeV	passing ID-cuts
$\epsilon^{\mu}_{\text{tracking}}$	Track Muon $P_T > 10$ GeV	match global muon to it
$\epsilon^{\mu}_{\text{standalone}}$	standalone Muon $P_T > 10$ GeV	match global muon to it
$\epsilon^{\mu}_{\text{ID cuts}}$	global Muon $P_T > 10$ GeV	pass ID-cuts

Table 7.2: Summary of the tag & probe criteria for the electron and muon identification efficiency measurement on $Z \to l^+l^-$ events.

The ID-cuts on the leptons are defined in chapter 6. In Figs. 7.7 and 7.8 the measured "Tag & Probe" muon and electron identification efficiencies are shown and compared to MC parametrised in p_T and η of the lepton.

The muon efficiencies derived here are used not only for this analysis of lost leptons, but also for the prediction of the $t\bar{t}$ and W + jet background of tau-leptons that decay hadronically [56]. Because that analysis uses different cuts on muon p_T and η, a fine binning of the muon efficiencies is used.

In data the identification efficiency for muons are in the range 94% - 98% and for electrons typically between 80% and 97%. A good agreement between data and MC is observed for all efficiencies. The efficiency in data is slightly smaller than in MC except for electrons in the high $|\eta|$-region. The largest difference between data and MC efficiency of 5% is found for very high p_T electrons in the outer η region of the negative η side of the detector. There is also a large uncertainty for low p_T electrons below 20 GeV, especially for the outer η regions of the positive η side of the detector. The GSF-efficiency is binned in p_T-bins of 10 GeV and the background of ECAL superclusters not belonging to an electron is rather large in the lowest bin, leading to the large uncertainty in the electron efficiency for $p_T < 20$ GeV. However, uncertainties and differences between data and MC is largest for the outer η-regions, where there are few events in the control sample discussed in section 7.2.2.2, and the influence on the final background prediction is small. In general the uncertainties and differences between data and MC are larger for the electrons. This is one of the reasons only a muon control sample and no electron control sample, discussed in 7.2.2.2 is used. This way the electron efficiencies enter only the numerator of the prediction of non-isolated and non-reconstructed electrons (see Eq. 7.4 - 7.10).

7.3.3 Lepton Isolation Efficiency

The muon isolation efficiency ϵ^{μ}_{ISO} is defined as the efficiency of a muon having a relative isolation $\mathrm{Iso}_{\mathrm{rel}} < 0.2$ as defined in Eq. 6.3. Only muons passing the ID-cuts with $P_T > 10$ GeV are taken into account. The electron isolation efficiency ϵ^{e}_{ISO} is defined accordingly. The probe definition and passing-criteria are summarised in Tab. 7.3.

The isolation efficiencies are determined on a sample with Z-bosons, but are used on the control sample consisting of $t\bar{t}$ and W + jet events. The $t\bar{t}$ and W + jet control sample in MC have an average isolation inefficiency $(1 - \epsilon^{\mu}_{Iso})$ for the

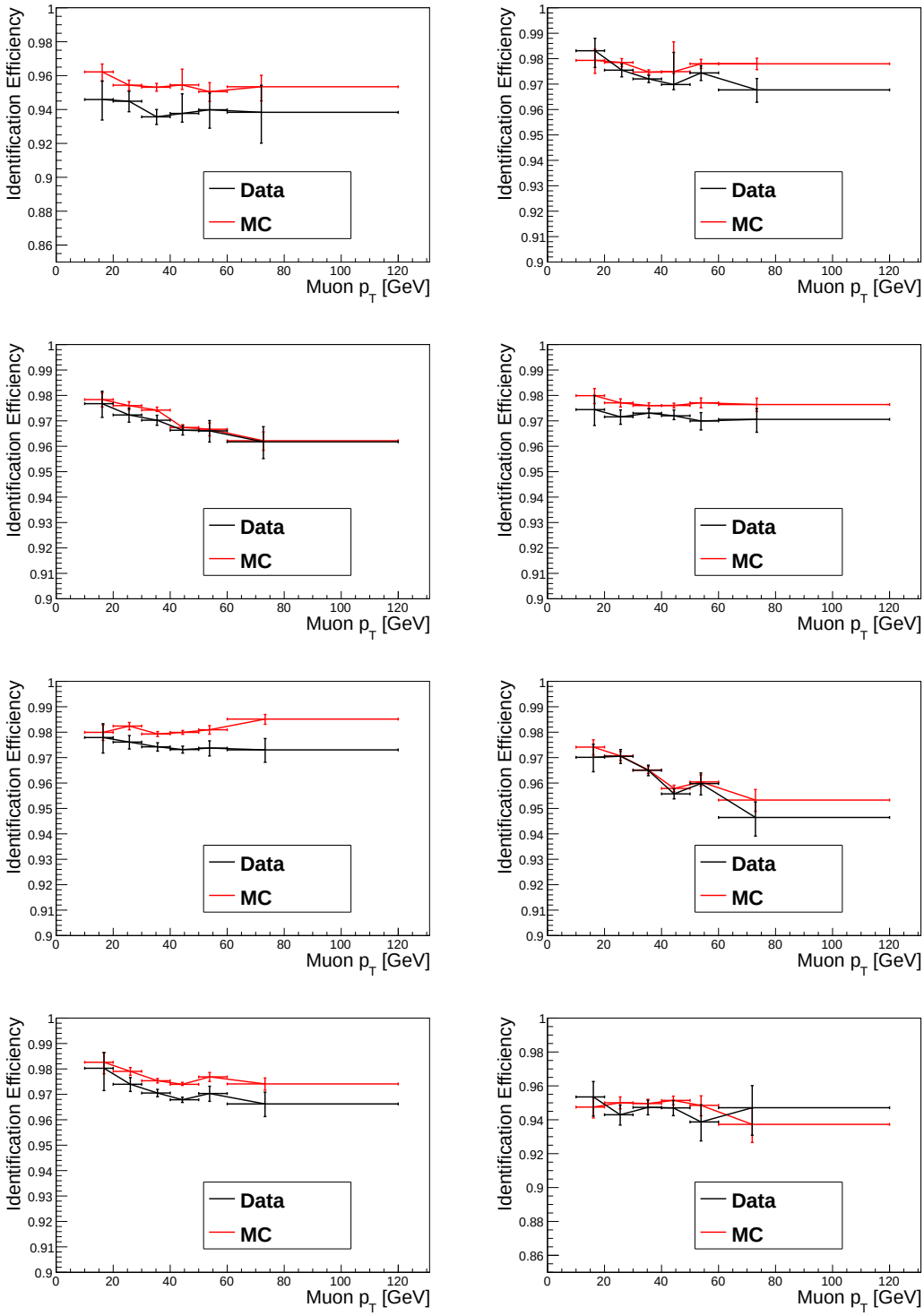

Figure 7.7: Identification efficiency ϵ_{ID}^{μ} for muons from the tag & probe method for different η-regions compared to MC simulation. The bin edges of the η-ranges are left top to bottom: -2.4, -2.1, -1.4, -0.7, 0 and right top to bottom: 0, 0.7, 1.4, 2.1, 2.4.

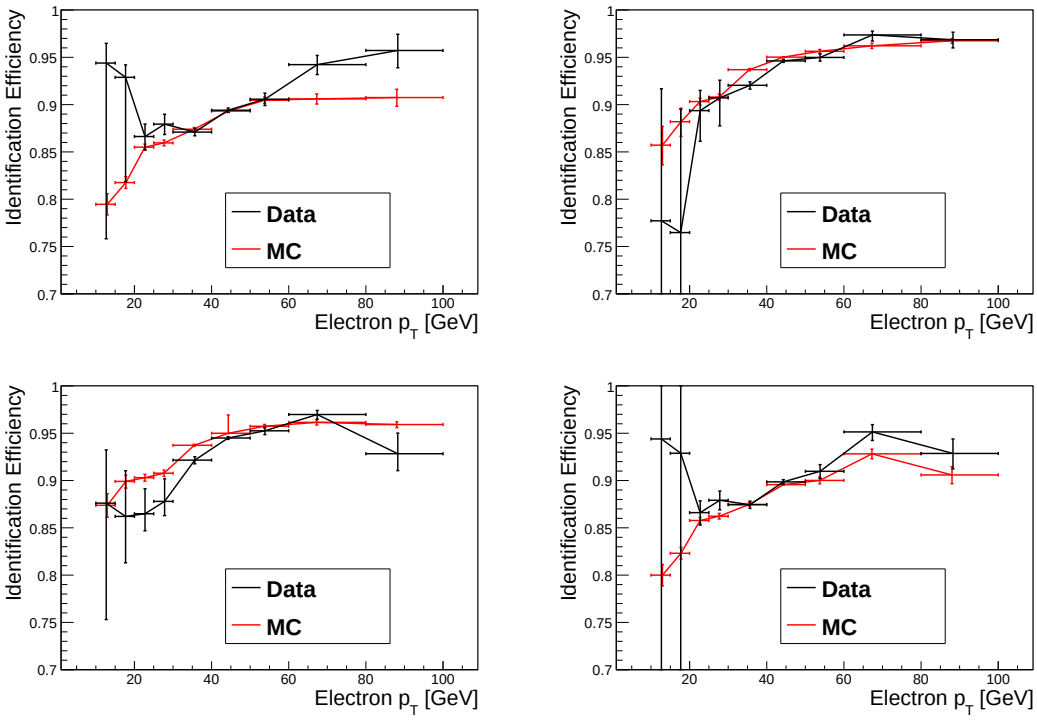

Figure 7.8: Identification efficiency ϵ^e_{ID} for electrons from the tag & probe method for different η-regions compared to MC simulation. The bin edges of the η-ranges are top left to right: -2.5, -1.2, 0 and bottom left to right: 0, 1.2, 2.5.

Efficiency	tag for the probe lepton	passing-criterion for the probe lepton
ϵ^{μ}_{ISO}	muon $P_T > 10$ GeV, ID-cuts	$\mathrm{Iso}_{\mathrm{rel}} < 0.2$
ϵ^{e}_{ISO}	electron $P_T > 10$ GeV, ID-cuts	$\mathrm{Iso}_{\mathrm{rel}} < 0.2$

Table 7.3: Summary of the tag & probe criteria for the electron and muon isolation efficiency measurement on $Z \to l^+l^-$ events.

baseline selection of 10.1 % and 6.7 %, respectavely, while it is only 3.4 % on a Z-sample. The reason for this large difference is due to the different kinematics of these events. While not much activity close to the leptons is expected in $W + jet$ and $Z + jet$ events, the top quark decays in a b-quark and a W boson, that can further decay into a lepton and a neutrino. This lepton is usually close to the b-jet. The larger jet activity in $t\bar{t}$ events will further decrease the isolation efficiency of the leptons. The analysis cuts on the number of jets and the H_T on the events in the control sample defined in section 7.2.2.2 increases further the differences between the "Tag & Probe" Z-sample and the control sample.

To account for this difference the isolation efficiency is measured in bins of the ΔR between the lepton and the closest jet and in bins of $p_T^{\text{lepton}}/p_T^{\text{closest jet}}$. This jet is a corrected calorimeter jet made solely from HCAL and ECAL clusters, that is required to have a $p_t > 30\ GeV$ and an electromagnetic energy fraction between 0.05 and 0.9 to avoid jets that arise from the lepton itself. Calorimeter jets are used here as the jet resolution is in this case of minor importance and particle flow jets are clustered from all particles including leptons as was discussed in chapter 5. This makes the probability of the jet passing the p_T cut dependent on the lepton and introduces many other unwanted correlations e.g. in the jet direction. It would also be possible to clean the jets from the leptons, but this would introduce a bias if the lepton definition is not exactly identical to the probe definition and studies would therefore be much more complicated to do. However, electrons leave a signal in the ECAL. If the ΔR between the electron and the jet is smaller than 0.5, the p_T of the electron is subtracted from the jet p_T to make the jet p_T comparable for both lepton flavours.

A comparison for these efficiencies on data and MC can be seen in Fig. 7.9 and 7.10. Very good agreement can be observed for the muon. The electron efficiencies also show a good agreement. The electron efficiency shows a large uncertainty for small ΔR and high $p_T^{\text{lepton}}/p_T^{\text{closest jet}}$ as the statistics of these events is small in the Z-sample in data and MC simulation. However, the effect on the final result is very small as these events are also rare in the control sample defined in section 7.2.2.2.

Figure 7.11 shows the shape of kinematical quantities ΔR and $p_T^{\mu}/p_T^{\text{closest jet}}$ used for the parametrisation of the isolation efficiency in comparison for $t\bar{t}$, W

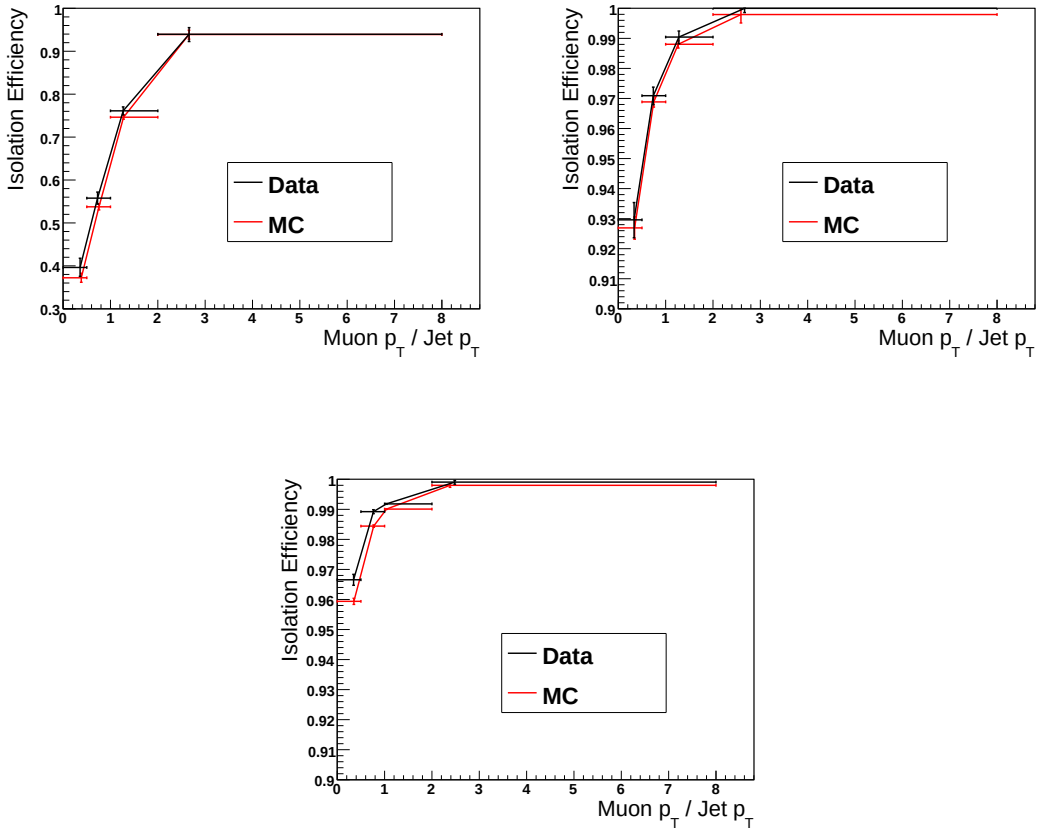

Figure 7.9: Isolation efficiency ϵ^{μ}_{Iso} for muons from the tag & probe method for different ΔR-regions as function of $p^{\mu}_{T}/p_{T}^{\text{closest jet}}$ compared to MC simulation. The bin edges of the ΔR-ranges are for the top left to right: 0, 0.5, 1.0 and on the bottom 1.0 and 5.0.

+ jet and Z-events, with the baseline cuts with inverted lepton veto on $t\bar{t}$ and W + jet events. It can be seen that the average ΔR is as expected smallest for $t\bar{t}$ and largest for Z-events. The difference is even larger that seen in the plot as the 73.5% of Z-events that do not have a jet are not shown here. In the efficiency determination these events are handeled as if they had $\Delta R = 5$. Also the average $p^{\mu}_{T}/p_{T}^{\text{closest jet}}$ is larger for Z-events, which is mainly due to the cuts of the baseline selection on the $t\bar{t}$ and W + jet events. The kinematics shown in Fig. 7.11 and the strong dependence of the isolation efficiency shown in Fig. 7.9 and 7.10 suggest that the parametrisation chosen is necessary for a

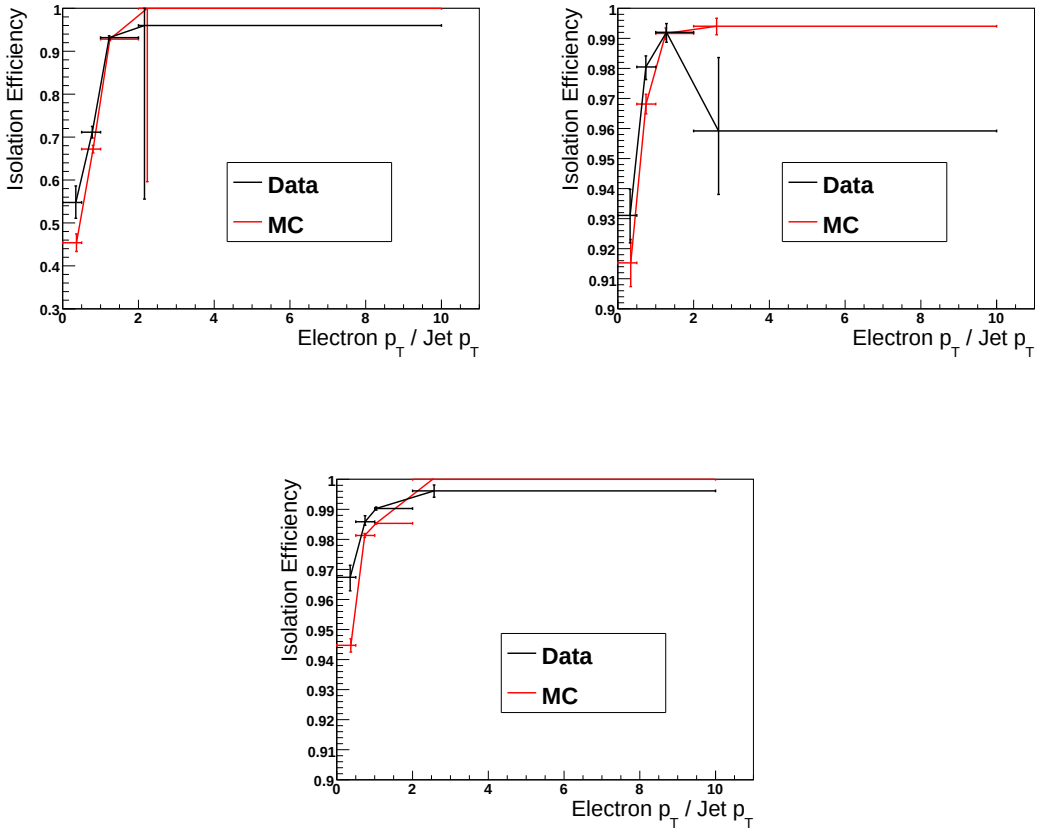

Figure 7.10: Isolation efficiency ϵ^{e}_{Iso} for electrons from the tag & probe method for different ΔR-regions as function of $p^{e}_{T}/p_{T}^{\text{closest jet}}$ compared to MC simulation. The bin edges of the ΔR-ranges are for the top left to right: 0, 0.5, 1.0 and for the bottom 1.0 and 5.0.

data-driven prediction of the background due to lost leptons. A final test on the data prediction quality is discussed in the next chapter.

The isolation efficiency at low ΔR is small, so that a large correction is applied to some events. This increases the statistical uncertainty and also makes a finer binning less optimal, as this would increase the statistical uncertainties further. Alternative binnings have been studied, e.g in terms of the jet multiplicity. Here, the dependence of the efficiency is not as strong, leading to smaller statistical uncertainties, but the kinematic differences between the samples cannot be resolved well enough leading to large systematic uncertainties.

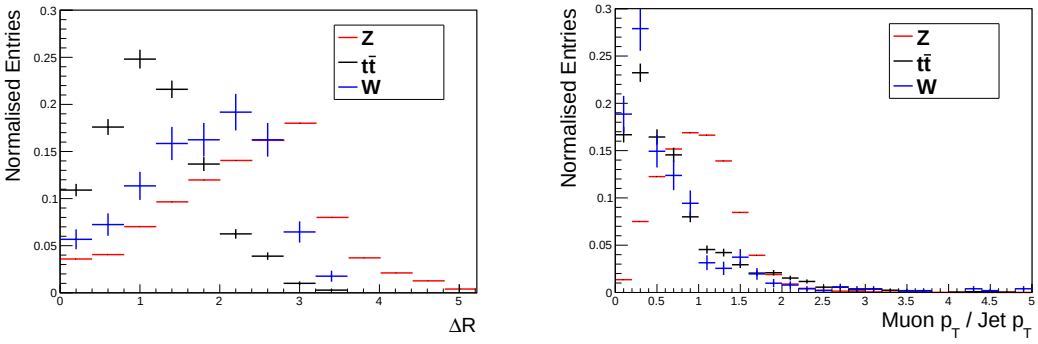

Figure 7.11: Comparison of kinematic quantities in $t\bar{t}$, W + jet and Z-events. Shown are the ΔR between the muon and the closest jet (left) and $p_T^{\mu}/p_T^{\text{closest jet}}$ (right) as used for the parametrisation of the muon isolation efficiency. $t\bar{t}$ and W + jet events are shown after the cuts of the baseline selection with inverted lepton veto. Only Z-events with at least one jet are shown, although 73.5% of the events do not have a jet as defined in the text. The area below the histogram is scaled to one for a better comparison.

7.4 Test of the Method on Simulated Events

In this section the method is tested on the MC sample to check if the resulting prediction agrees with the plain MC simulation of the same sample. It is also checked if the $\not{H}_T$ and H_T distributions agree between the MC simulation and the prediction using simulated events.

In Tab. 7.4 the plain MC simulated background contributions on MC and the prediction on the same MC sample are compared. The prediction and the plain MC agree very well for the non-isolated leptons independent of lepton flavour or sample. This shows that the parametrisation chosen is able to account for the kinematic differences between the samples. The agreement for leptons out of acceptance is also very good. This is not surprising for the combination of $t\bar{t}$ and W + jet, as the acceptance efficiency is taken from the same MC sample, but the agreement in each sample shows the similarity of the acceptance efficiency in $t\bar{t}$ and W + jet. It can also be seen that the largest discrepancy is observed for not reconstructed leptons, more importantly electrons. This underprediction is discussed below in more detail and is corrected for in the prediction on data.

	$t\bar{t}$ prediction	$t\bar{t}$ simulation	W+jets prediction	W+jets simulation
not reconstructed $\mu^{\pm}$	0.3 ± 0.0	0.6 ± 0.1	0.5 ± 0.1	0.8 ± 0.2
not isolated $\mu^{\pm}$	1.3 ± 0.1	1.2 ± 0.1	1.3 ± 0.2	1.3 ± 0.3
$\mu^{\pm}$ out of acceptance	2.8 ± 0.1	2.8 ± 0.2	4.8 ± 0.3	4.9 ± 0.5
not reconstructed $e^{\pm}$	1.0 ± 0.1	1.3 ± 0.1	1.6 ± 0.1	2.3 ± 0.4
not isolated $e^{\pm}$	1.0 ± 0.1	1.1 ± 0.1	1.1 ± 0.2	1.0 ± 0.2
$e^{\pm}$ out of acceptance	3.2 ± 0.1	3.1 ± 0.2	5.0 ± 0.3	5.2 ± 0.5
total	9.5 ± 0.3	10.0 ± 0.3	14.3 ± 1.0	15.5 ± 1.0

Table 7.4: Comparison of the prediction on MC and the plain MC simulation on the $t\bar{t}$ and W + jet sample corresponding to 100/pb. The uncertainties shown are statistical only.

7.4.1 Test of the Prediction of not-isolated Leptons

In Fig. 7.12 the $\not{H}_T$ and H_T distribution of the prediction of events where the lepton is not isolated is compared to the plain MC simulation of these events. The $t\bar{t}$ and W + jet samples are combined, but separated for the electron and the muon channel. A good agreement can be observed. This kind of test of the method is referred to as "closure"-test in the following. As shown in Table 7.4 the agreement is also very good for $t\bar{t}$ and W + jet separately. The closure plots for the separated test of $t\bar{t}$ and W + jet can be found in the appendix A. Only statistical uncertainties are shown in these plots to test the method. These uncertainties include the statistical uncertainties on the efficiencies of the "Tag & Probe " method on MC. The shape of the predictions for the electron and the muon channel is similar, as the same control sample is used to predict the background of lost electrons and muons.

7.4.2 Test of the Prediction of non-reconstructed Leptons

In Fig. 7.13 the same distributions are shown for events where the lepton is not reconstructed. The separated $t\bar{t}$ and W + jet closure plots can be found in the appendix A. Even though the statistical uncertainty is quite large, a systematic underprediction can be observed for both samples and for both lepton flavours.

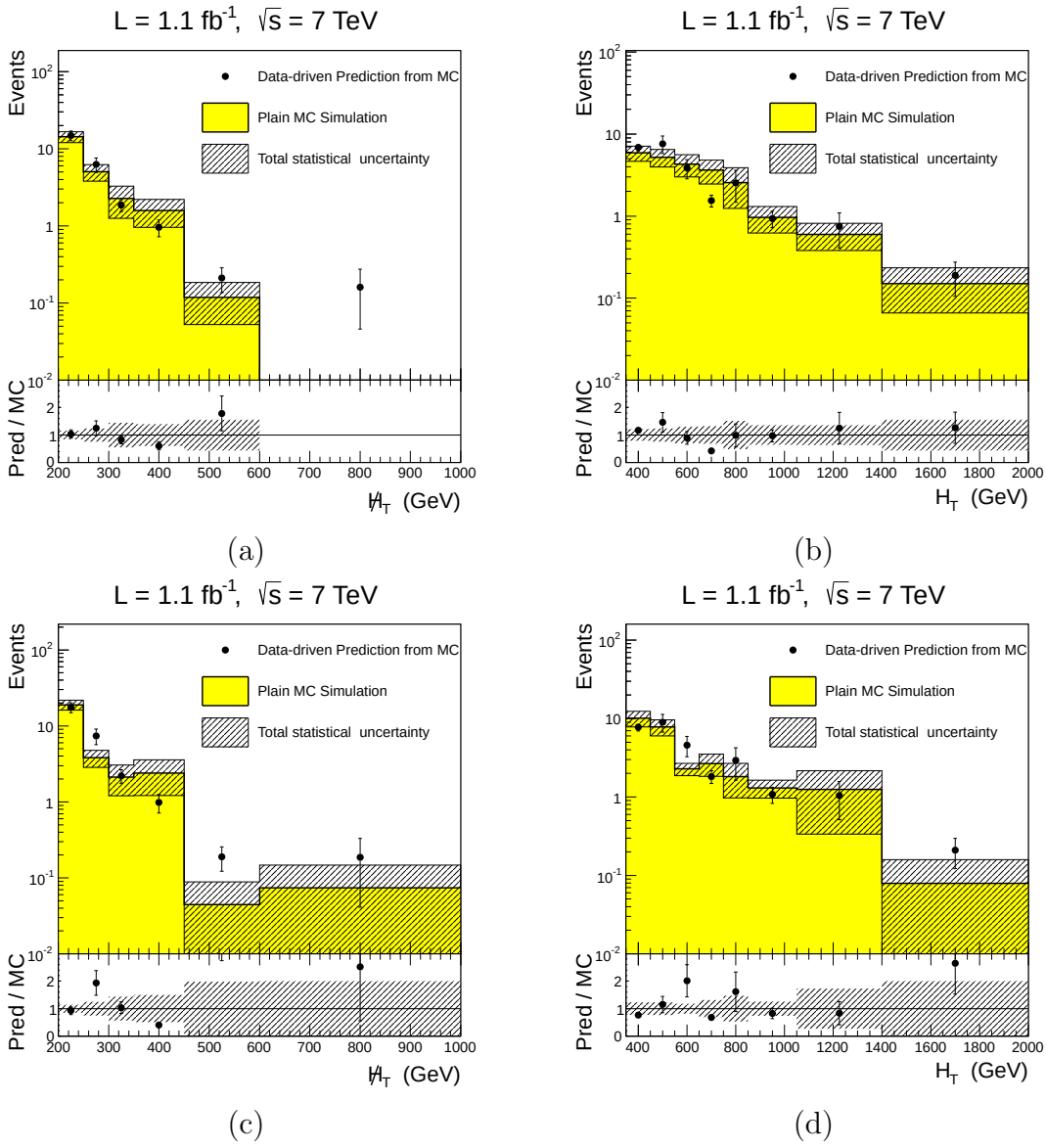

Figure 7.12: Comparison of the kinematic properties of the plain MC simulation and the prediction on the same sample of identified but non-isolated leptons from $t\bar{t}$ and W + jet channel combined on MC, for electrons (upper two plots) and muons (lower two plots). The shown variables are MHT (left) and HT(right)

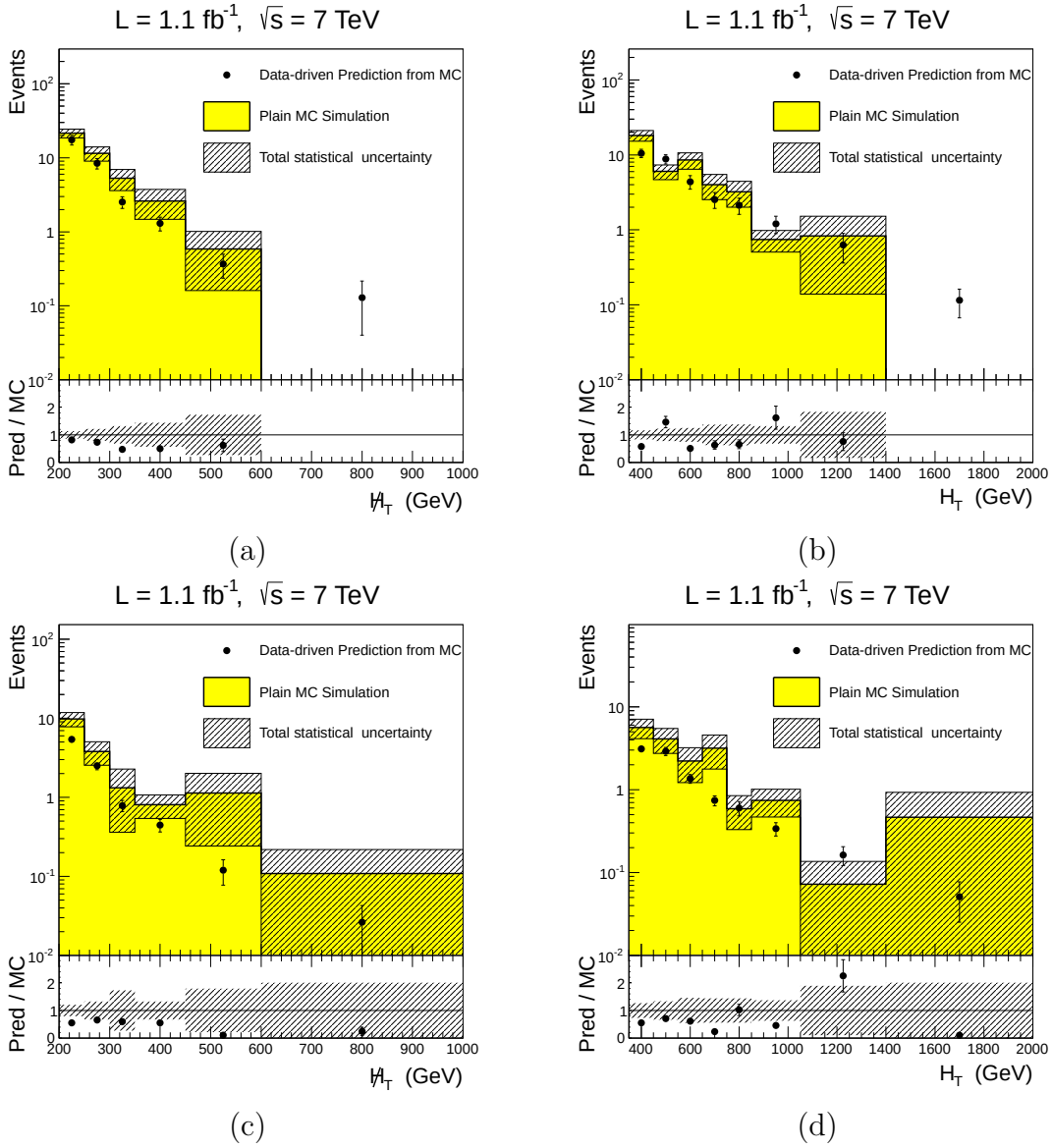

Figure 7.13: Comparison of the kinematic properties of the plain MC simulation and the prediction on the same sample of non-identified leptons in detector acceptance from $t\bar{t}$ and W + jet channel combined on MC, for electrons (upper two plots) and muons (lower two plots). The shown variables are MHT (left) and HT(right). The difference in scale will be corrected for.

The shape of the kinematic variables seem to be in good agreement. The total prediction of events with not reconstructed leptons amounts to 3.4 ± 0.3 events for 100pb^{-1} compared to 5.0 ± 0.5 events expected from plain MC simulation. This corresponds to a total underprediction of 32% for these kind of events, half of it being covered by the statistical uncertainty. However, this underprediction corresponds to only 7% of the total and the prediction on data is corrected for this effect.

The reason for this difference is, that while the reconstruction efficiency does not differ as much as the isolation efficiency between the samples, there is still some dependence on the kinematics of the events that cannot be resolved with the binning chosen. A binning similar to that for the isolation efficiency is not possible as supercluster need to be cleaned from jets in the "Tag & Probe" method as was discussed in Section 7.3.

7.4.3 Test of the Total Background Prediction

Figure 7.14 shows the final test of the method comparing the total estimation before the 7% scale correction discussed above to the true number of total events, and a good agreement can be observed for all distributions. The only exception is the lowest bin in the H_T distribution. This is probably to some extend a statistical fluctuation in the MC control sample as comparisons between data and MC in Fig. 7.4 suggest. The main reason, however, is the different jet spectrum for leptons in and out of acceptance and the cut on the number of jets as discussed in section 7.2.2.5. The separated $t\bar{t}$ and W + jet closure plots and a closure plot for leptons out of acceptance can be found in the appendix A.

The good agreement of the primary vertex distribution between simulation and prediction on simulation is reassuring, as it shows that the method is not very sensitive to pile-up. The main reason for this is the rather narrow isolation cone and the loose isolation definition. In the very busy environment of the events of interest, the additional energy due to pile-up does not play a big role. [1]

[1] The primary vertex distribution for the data used here is quite different to the distribution of the last femtobarn of data taken in 2011. This distribution, which peaks around 13 primary vertices, can not be tested with the simulation available, as too few events with such a high pile-up contribution are simulated.

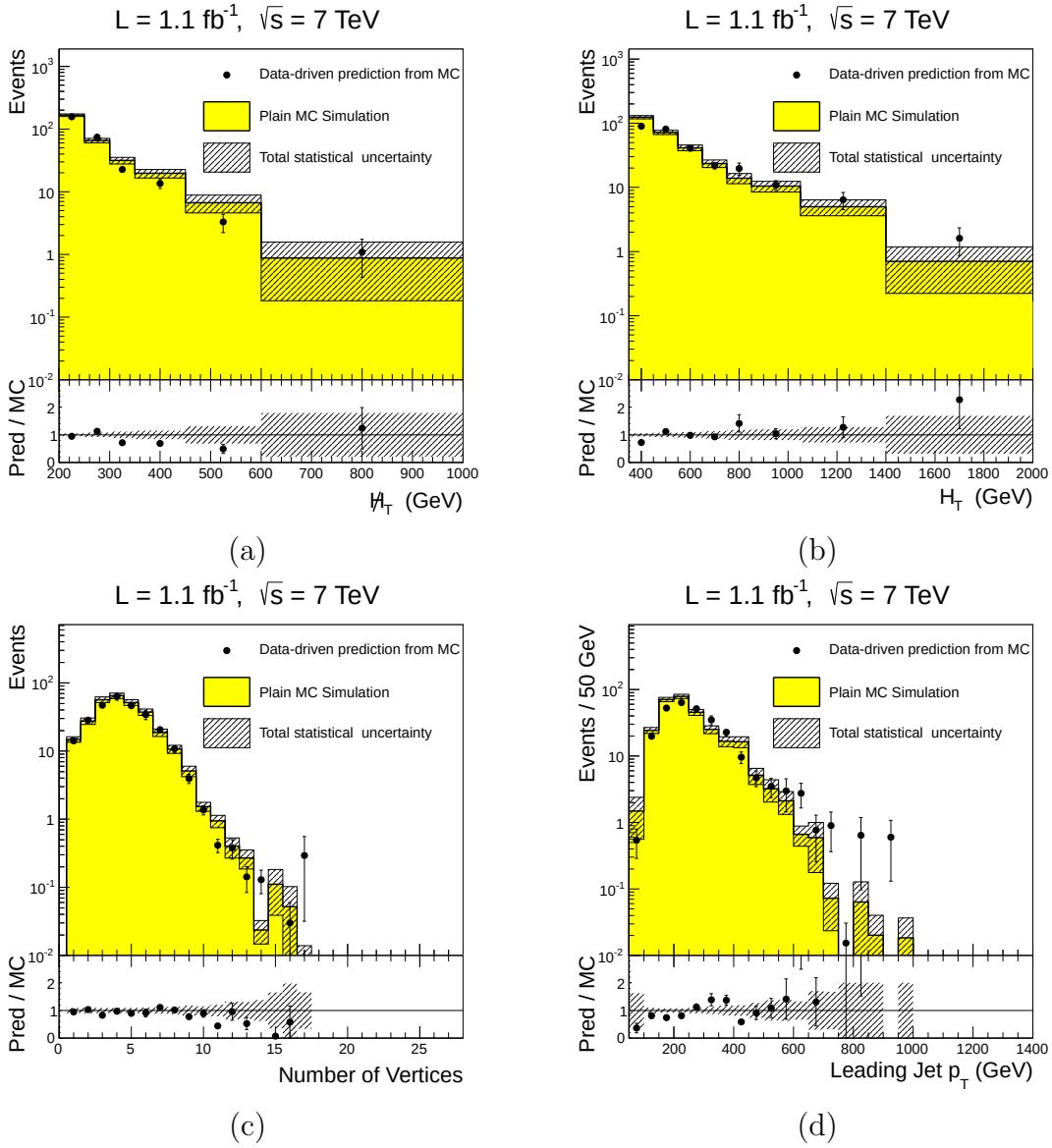

Figure 7.14: Closure test of the method. The total background prediction without scale correction on $t\bar{t}$ and W + jet MC samples is compared to the plain MC simulation for the same samples. using the muon control sample only The shown variables are: MHT (a), HT (b), number of primary vertices (c) and the leading jet p_T (d).

A 10% uncertainty is attributed to the level of agreement which is mainly due to the remaining differences in the reconstruction efficiency between the $t\bar{t}$, W + jet and Z sample. Although this is the largest non-statistical uncertainty, it is much smaller than the statistical uncertainties in the evolved selections used for the interpretation of the results.

7.5 Uncertainties

The dominant source of uncertainties for the evolved selections comes from the statistical limitations. As the best signal to background ratio can be achieved at high values of H_T or $\not{H}_T$ depending on the SUSY-parameter point under study, cuts will always be adjusted in a way that the control sample is low in statistics. The events with a small ΔR between the lepton and the closest jet enter the estimate with a relatively large weight due to the small isolation efficiency of these events as discussed in chapter 7.2.2. Therefore, the statistical uncertainties are higher than naively expected because events enter the prediction with different weights.

The uncertainty on the isolation and reconstruction efficiencies are partly statistical and partly systematic. The statistical contribution to this uncertainty is arising from the statistic of the "tag & probe" sample. This uncertainty is already small at the sample used and will improve with luminosity. The other part of this uncertainty is purely systematical as it accounts for possible remaining differences in the control sample and the tag & probe sample and possible small systematic uncertainties in the "tag & probe" method itself. This uncertainty is estimated to be 10% from the closure tests as explained in section 7.4.

Another systematic uncertainty arises from the use of Monte Carlo simulation to describe the ratio between leptons within and out of the detector acceptance. This ratio relies on the well modeled p_T-spectrum of the leptons and to a small extend on the ratio between $t\bar{t}$ and W + jet events in the control sample. There is also a dependence on the $\not{H}_T$ of the event, but this dependence is found to be small for cuts above the baseline selection even though it is larger for smaller $\not{H}_T$ values as discussed in Sec. 7.2. The uncertainty on the acceptance efficiency is estimated to be 6%, which includes the differences between $t\bar{t}$ and W + jet and

Source	Systematic Uncertainties [%]	
Statistics of control-sample	−8.1	+8.1
iso- & id- efficiencies (statistical)	−4.2	+4.2
Differences $t\bar{t}$, W, Z-samples	−10.0	+10.0
and kinematic in control vs. signal region		
SM background in control-region	−3.0	+0.0
MC use for acceptance calculation	−3.9	+3.9
transverse W-mass-cut	−4.3	+4.3
total, combined uncertainty	−15.0	+14.7

Table 7.5: The dominant relative systematic uncertainties on the number of events of the lost-lepton prediction for the baseline selection with $1.14 fb^{-1}$ of data.

the uncertainties due to the parton distribution functions (PDF) of the proton. The dominantly gluon induces $t\bar{t}$ process has a much larger PDF uncertainty compared to the mainly quark induced W + jet process. For the calculation of this uncertainty $t\bar{t}$ is assumed to contribute three quarters of the background. The resulting uncertainty on the total background estimation is about 4%.

Tests on possible further Standard Model background to the control sample on MC have shown a very small contribution. As discussed in chapter 7.2.2.2 the estimated uncertainty is 3%. As there can be no negative signal contamination this uncertainty only has a negative contribution.

The uncertainty on the efficiency of the cut on the transverse mass results in an uncertainty of less than 5% on the total prediction as discussed in chapter 7.2.2.2.

The different systematic uncertainties are summarised for the baseline selection in Tab. 7.5.

7.6 Prediction of the Lost Lepton Method

With all the studies discussed above an estimation of the electroweak background containing a W boson decaying to an electron or muon in the final state can be performed. The method discussed in section 7.2 is used on the control sample

discussed in section 7.2.2.2 with the efficiencies discussed in section 7.3. Additionally the correction of 7% due to kinematical differences between the samples, that cannot be resolved by the parametrisation of the reconstruction efficiency, discussed in section 7.4.2 and the small correction for di-leptonic events discussed in section 7.2.3 is applied.

selection	Prediction on Data			MC Expectation		
Baseline	244	± 20	$^{+30}_{-31}$	291	± 11	$^{+14}_{-29}$
Medium	12.7	± 3.3	± 1.5	17.0	± 2.9	$^{+2.4}_{-1.4}$
high H_T	22.5	± 6.7	$^{+3.0}_{-3.1}$	21.9	± 3.0	$^{+2.6}_{-2.1}$
high $\not{H}_T$	0.8	± 0.8	± 0.1	1.3	± 0.8	$^{+0.2}_{-0.4}$

Table 7.6: Final event yield for the lost-lepton RA2 background for the baseline selection (three jets > 50 GeV, $H_T > 350$ GeV, $\not{H}_T > 200$ GeV, $\Delta\Phi$ cuts, lepton veto) and for the evolved search selection "high $\not{H}_T$ ", "high H_T " and "medium". The simulation corresponds to the data luminosity of $1.14 fb^{-1}$. The systematic uncertainty on the plain MC expectation takes into account only the jet energy scale and luminosity uncertainty.

The results are shown in Tab. 7.6 and compared to the expectation from plain MC simulation with the statistical-, jet energy scale- and luminosity-uncertainties. The prediction on data is about one standard deviation below the pure MC expectation. In the high H_T selection, the large statistical uncertainty originates from one event with a rather high correction in the control sample.

To compare the shapes of kinematic variables between data-driven prediction of the background due to lost leptons and pure MC expectation, some variables are shown in Fig. 7.15. A good agreement in the shape of these variables can be observed. These plots are also published in [45].

Comparing the uncertainties between the prediction on data and the MC expectation in Tab. 7.6 the impression might arise that the data-driven prediction is not superior to the use of MC simulation. However, not all uncertainties on the use of pure MC simulation have been taken into account. No uncertainty on the next-to-leading-order (NLO) cross-section, the value of α_S or the parton desity functions (PDF) have been taken into account. These uncertainties can have large

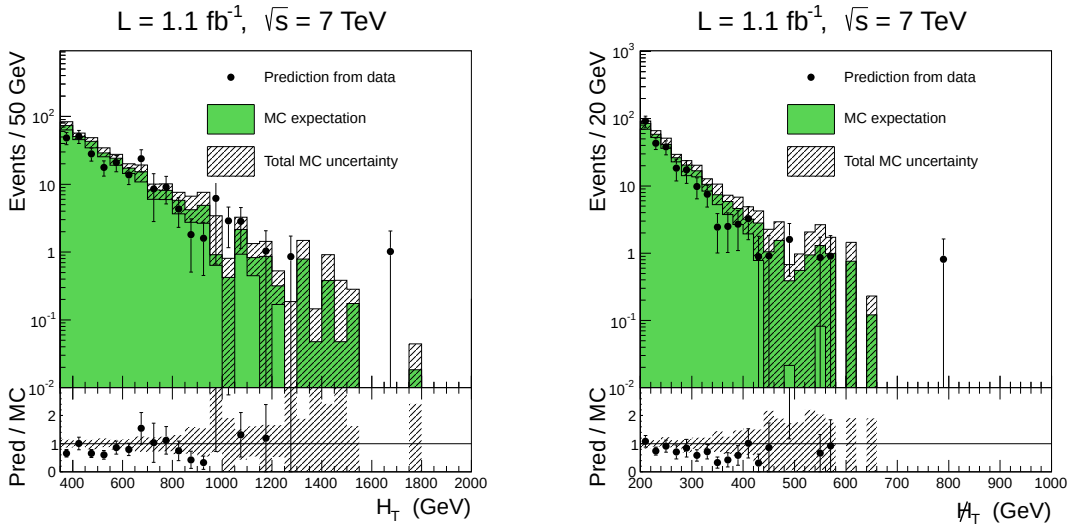

Figure 7.15: Prediction for HT (left) and MHT (right) on $1.14 fb^{-1}$ of data compared to the properly scaled expectation from plain MC simulation.

effects as the SUSY search described investigates the tails of distributions, while the MC is tuned to the correct description of the bulk of the LHC data. Especially for the W + jet background several jets need to be in the event in addition to the hard process and the exact prediction from simulation of the kinematics of these events is very challenging. Furthermore, only the uncertainty on the jet energy scale is taken into account for the simulation of the detector. The reconstruction and isolation efficiencies discussed in section 7.3 are only one example for possible deviations between the simulation and the real, very complex, detector.

All of these effects are by construction taken care of in the data-driven prediction of the background discussed and therefore the quality of the prediction of the background discussed is improved significantly.

The sum of all simulated SM backgrounds presented in chapter 6.4 is already considerably larger than the data found in the search region. It is therefore very likely that the pure MC expectation overestimates the background. The fact that the data driven prediction of the background discussed here yields a smaller value than the expectation from pure MC is therefore another indication of the superior quality of the method discussed. The comparison between data and the combination of the prediction of this and all other backgrounds will be discussed

in section 7.8.

The data-MC comparison in the last chapter already indicated that the evolved selections have a superior signal to background ratio and are therefore most useful for SUSY searches. These evolved selections lack statistics in the data control samples as well as in the MC. It is therefore crucial to check this method and the behaviour of the acceptance efficiency with a higher statistics MC, that is still in preparation. Note that higher luminosity implies higher cut values for H_T and $\not{H}_T$, reintroducing the problem of a lack in MC statistics. The W + jet MC has intrinsically a larger problem with statistics due to the much higher cross section compared to $t\bar{t}$.

7.7 Other Standard Model Background

In this section the other background estimation methods used in the analysis will be reviewed shortly. As described in chapter 6, the main sources of background are $t\bar{t}$-, W + jet-, QCD- and Z + jet-events, where the Z-boson decays into two neutrinos.

The "lost lepton" method described above in full detail estimates the $t\bar{t}$ and W + jet events where there is a real electron or muon in the final state, which is not isolated, not reconstructed or out of detector acceptance. The remaining background of $t\bar{t}$ and W + jet are events, where the W boson decays into a tau lepton, which decays hadronically. This background is estimated with the "hadronic tau" method [56]. For the QCD background there are two methods available, the "rebalance and smear" method [57] and the "factorisation" method [58] used as a cross check. The latter will not be described here. For the $Z \to \nu\nu$ background there are several methods available, but only the method using the similarity between the Z-boson and photons [59] delivers enough statistics to be used meaningfully on the evolved selections.

All methods have been proven to work on MC. Even though the uncertainties are large for some of the background, every method gives estimates with smaller uncertainties than a pure MC prediction would provide.

7.7.1 Hadronically decaying Tau Leptons

Similarly to the "Lost Lepton" method a muon control sample is used to estimate this background, but only two jets are required as an additional jet from the tau decay is present. Also the H_T and $\not{H}_T$ cuts are relaxed. Due to these relaxed cuts, it is not possible to use the hadronic triggers, instead a muon trigger is used. Because of the trigger threshold of 17 GeV, only muons with $p_T > 20$ GeV can be used.

Because of lepton universality the muon can be replaced by a tau lepton. For this the muon is replaced by a jet with a p_T that is determined using a τ-response template from MC, which gives the average ratio of the p_T of a jet originating from the tau and the p_T of the tau itself. With this jet instead of the muon the values for H_T and $\not{H}_T$ are recalculated, and the baseline cuts are applied. These events are re-weighted using a correction factor for the branching ratio of hadronically decaying taus and lepton- & trigger-efficiencies. As only prompt muons should be used for this estimate the events are also re-weighted for the amount of muon events that originate from a tau that decays into a muon and two neutrinos.

There is an overlap between the sample used for this method and the "Lost Lepton" method, albeit reduced by the fact that this method only uses muons with a p_T greater than 20 GeV and because of the recalculation of H_T and $\not{H}_T$. As the correction due to lepton inefficiencies only plays a minor role in this analysis the systematic uncertainties are not strongly correlated. While statistical limitations are the source for the dominant uncertainty in the evolved selections, the uncertainty on the tau-template dominates for the baseline selection.

7.7.2 QCD

QCD events can pass the selection cuts only if jets are severely mismeasured as QCD events do not have intrinsic $\not{H}_T$ in the event, except for a small contribution from the decay of heavy flavour quarks. If only one jet is mismeasured or emits neutrinos due to heavy flavour quark decays, the $\not{H}_T$ vector will very likely be aligned in the transverse plain with one of the first three jets. Events like this

would not pass the $\Delta\Phi$ cut. To estimate how many events pass these cuts the "rebalance and smear" method is used.

First it is needed to get a sample of QCD events with perfectly measured jets. To get this sample every jet in every event is adjusted to form a perfectly balanced event. This is done by maximising the likelihood calculated from the resolution functions of the jet momenta under the condition that $\not{H}_T = 0$. There are also non-QCD events being rebalanced and are input to this estimate, but as the number of these events are small compared to the QCD events and because the kinematics of these events is QCD-like after the rebalancing, this is not a big problem.

In the second step every jet is smeared again using the jet resolution functions that are measured in data [43]. As this method aims to estimate the tail of the $\not{H}_T$ distribution it is especially important to also account for badly mismeasured jets in this step, i.e. including the non-Gaussian tails of the resolution. Finally the selection of the analysis is applied on these rebalanced and smeared events providing an estimate for the QCD background.

All events with enough energy need to be included in the sample to be rebalanced. As some of these events are triggered with a high prescale, large weights are introduced. The smearing is repeated several times with different values for the response of the rebalanced jets and the variance of this distribution is taken as statistical uncertainty. Due to the possibly high prescales for some events this uncertainty is large.

7.7.3 Invisibly Decaying Z

The method to estimate the background due to Z-events, where the Z decays into two undetected neutrinos, uses the fact that high p_T photons are produced in a similar way as high p_T Z-bosons. Only these high p_T events are of importance for this method as the two neutrinos from the Z-boson and the boost of the boson must be sufficient to generate enough $\not{H}_T$. The method starts from a photon + jet sample and replaces the photon in the event record by a invisibly decaying Z-boson, i.e. the photon is removed. H_T and $\not{H}_T$ are recalculated without the photon.

There are several corrections needed. First the smaller cross section of Z-events compared to photon-events needs to be accounted for and efficiency corrections to the photon events are needed. Furthermore, only events with prompt photons are relevant to this analysis. Non-prompt photons are background, that needs to be corrected for.

This analysis needs more corrections than the analysis where Z events decaying to two electrons or muons are used and the leptons are removed. However, this cleaner Z analysis suffers from a severe lack of statistics due to the factor 6 smaller branching fraction of Z-bosons decaying muons compared to neutrinos. Therefore, the photon analysis is chosen. In future updates of the analysis it is planed to use a combination of several background estimation methods to reduce the uncertainties on this background.

7.8 Combination of the Background

In this section the background prediction as described above is combined and compared to the data.

Method	Baseline (H_T >350 GeV) ($\not{H}_T$ >200 GeV)		Medium-H_T &$\not{H}_T$ (H_T >500 GeV) ($\not{H}_T$ >350 GeV)		High-H_T (H_T >800 GeV) ($\not{H}_T$ >200 GeV)		High-$\not{H}_T$ (H_T >800 GeV) ($\not{H}_T$ >500 GeV)	
$Z \to \nu\bar{\nu}$	376.3	$\pm 12.3 \pm 79.2$	42.6	$\pm 4.4 \pm 8.9$	24.9	$\pm 3.5 \pm 5.2$	2.4	$\pm 1.1 \pm 0.5$
$t\bar{t}/W \to e, \mu$+X	243.5	$\pm 19.8^{+30.0}_{-30.9}$	12.7	$\pm 3.3 \pm 1.5$	22.5	$\pm 6.7^{+3.0}_{-3.1}$	0.8	$\pm 0.8 \pm 0.1$
$t\bar{t}/W \to \tau_{\text{hadr}}$+X	263	$\pm 8 \pm 7.4$	17	$\pm 2 \pm 0.7$	18	$\pm 2 \pm 0.5$	0.73	$\pm 0.73 \pm 0.04$
QCD	30.9	$\pm 35.2^{+16.6}_{-6.2}$	1.3	$\pm 1.3^{+0.6}_{-0.4}$	13.5	$\pm 4.1^{+7.3}_{-4.3}$	0.09	$\pm 0.31^{+0.05}_{-0.04}$
Total background	927.5	± 103.1	73.9	± 11.9	79.4	± 12.2	4.6	± 1.5
Observed in data	986		78		70		3	

Table 7.7: Predicted event yields from the different background estimation methods for the baseline selection and for the evolved search regions. The background combination is performed by taking into account the shape of the uncertainties. Thus the simple sum of the mean predictions of each background prediction does not necessarily correspond to the combined background prediction.

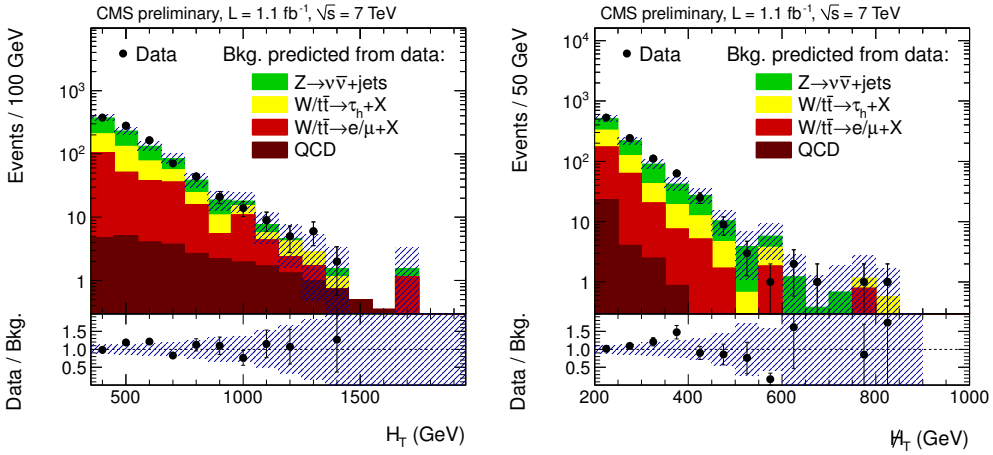

Figure 7.16: Comparison between the data and the data driven background estimates for the baseline selection. The distributions shown are H_T (left) and $\not{H}_T$ (right).

The predictions from the different background estimation methods for $1.14 fb^{-1}$ are summarised in Tab. 7.7. The combination of these backgrounds takes into account the different distributions of the uncertainty, although most uncertainties are found to be in a good approximation to be distributed in a Gaussian way. These possibly asymetric distributions, and the fact that the part of the distribution that corresponds to negative background predictions are not taken into account, lead to a possible shift of the mean predicted value compared to the simple sum. There are only minor systematic correlations between the different background estimation methods. The statistical correlation between the two $t\bar{t}$ and W + jet predictions is taken into account for the high $\not{H}_T$ evolved selections. This is the only selection, where this correlation has a significant influence on the total uncertainty.

Data and SM background prediction agree within the uncertainties. In general, the prediction slightly over-estimates the data for the evolved selection. Comparing the data-driven background predictions to the pure MC simulation shown in Ch. 6, it can be seen that the data-driven predictions agree much better with the data. This indicates the improvement due to these background estimation methods. The comparison of the H_T and $\not{H}_T$ distribution between data and

the data driven background estimates can be seen in Fig. 7.16. These plots are also published in [45].

As no excess of data can be observed, it is only possible to set exclusion limits within the SUSY parameter space.

8

Interpretation in the cMSSM

In this chapter the interpretation of the results within the constraint MSSM [61] (cMSSM) is presented. The limits on this model are set with the CL_s method [62].

8.1 Results with the CL_S Method

Method

As it is necessary to know the expected signal yield [1] for different points in the parameter space of the cMSSM and the uncertainties on this value, the analysis is run on the signal sample produced with CMSSW 4.2 fast simulation. The NLO cross section is calculated for each production mechanism separately using Prospino [63]. The scan has a positive μ, $\tan\beta = 10$ and $A_0 = 0$. The values m_0 and $m_{1/2}$ are varied from 0 to 2000 GeV and 0 to 800 GeV, respectively, in steps of 20 GeV. [2]

The systematic uncertainties on the signal yields taken into account are:

- Jet energy scale: The jet energy scale is scaled up and down by the uncertainty derived for data [41] and the corresponding difference in the signal

[1] For a cross section limit the signal acceptance is sufficient, but here the cross section calculated for the cMSSM as shown in Fig. 3.4 is used directly, speeding up the limit calculation

[2] Several points failed in the production chain and they are therefore not included in the limit calculation, but hardly any of these points are close to the limit curve found.

acceptance is taken as the uncertainty.

- Jet energy resolution: The generator level jets are smeared with the detector resolution as measured in data plus and minus the uncertainty on this resolution. Half the difference between the event yield of both measurements is taken as the uncertainty.

- Parton distribution functions: Using the uncertainties on the signal acceptance calculated with the latest PDF4LHC recommendation. [64]

- Luminosity: The uncertainty on the luminosity measurement is taken to be 6%. [65] [1]

The signal acceptance and the uncertainties for the cMSSM parameter space can be found in the appendix B. The NLO cross section shown in Fig. 3.4 used for the limit calculation was discussed in chapter 3.5.

To calculate the confidence level (CL) of a given hypothesis first a probability density function is defined for each hypothesis. For the background only hypothesis a Poisson function is created with the predicted background events as mean value to account for statistical fluctuations of the data. Similarly for the signal plus background hypothesis the mean of the Poisson is the expected background plus the expected signal contribution.

Systematic uncertainties are not of immediate interest, but must be accounted for and are therefore treated as nuisance parameters. As the shape of the combined uncertainties of the background prediction is Gaussian, these parameters are Gaussian distributed around zero. The width of the distribution is the uncertainty relative to the mean value of the background prediction.

With these probability density functions a test statistics Q can be created for the background only hypothesis, the signal plus background hypothesis and the data. An optimal[2] choice for the test statistics that maximises the difference

[1] The Uncertainty quoted in the reference is 4.5%.However, at the time of the limit calculation the value was still 6% that was reduced due to improvements in the measurement shortly afterwards. The influence on the limit is very small.

[2] The likelihood ratio is shown to be optimal in the Neyman-Pearson lemma

between background only and background plus signal hypothesis is the likelihood ratio. The value for Q on data is defined as:

$$Q = \frac{L(data, s+b)}{L(data, b)} \tag{8.1}$$

The distribution of the likelihood $L(data, Hypothesis)$ is the probability density function (PDF) of the data for a given hypothesis. For the signal plus background and background only hypothesis toy Monte Carlo data is generated according to the probability density function for the signal plus background and background only hypothesis, respectively, leading to a test statistic distribution. An example plot of such a test statistics is shown in Fig. 8.1.

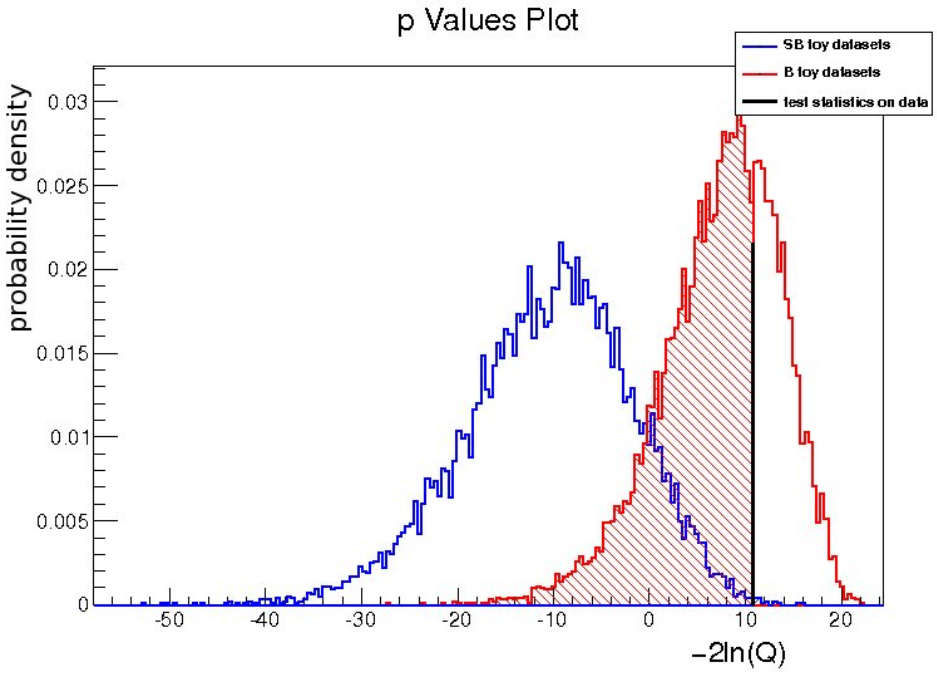

Figure 8.1: Test statistics shown as -2 ln(Q) for an example susy point ($m_0 = 300$, $m_{1/2} = 500$). The red plot shows the distribution with data from a background-only toy dataset and the blue plots shows the distribution with data from a signal-plus-background toy dataset. The curves are normalised to the integral of one. The shaded area of the red plot corresponds to $1 - CL_b$, the small shaded area under the blue graph on the right of the Q value found in data corresponds to CL_{s+b}

CL_b and CL_{s+b} are defined as the probability that the observed Q in data is larger or equal to the Q of the distribution for the background-only and signal-plus-background hypothesis:

$$CL_b = P_b(Q \leq Q_{obs}) \tag{8.2}$$

and

$$CL_{s+b} = P_{s+b}(Q \leq Q_{obs}) \tag{8.3}$$

CL_S is defined as the ratio between the confidence level of the signal plus background hypothesis CL_{s+b} and the background only hypothesis CL_b to account for statistical fluctuations[1]:

$$CL_s = \frac{CL_{s+b}}{CL_b} \tag{8.4}$$

Even though CL_s is not a confidence level, but a ratio of two confidence levels, a tested cMSSM point is excluded with at least 95% confidence if $CL_s < 0.05$. To calculate the expected limit toy Monte Carlos are generated according to the expected background only hypothesis. Using the mean and the closest two points that contain 68% of the toy MC distribution instead of the measured data the mean and the one sigma uncertainty band of the expected limit is calculated.

Results

Calculating the limits for all selections, it can be seen in Fig. 8.2 that the high H_T and high $\not{H}_T$ selection are most sensitive. The $\not{H}_T$ selection is as expected most sensitive in the region of low m_0 up to about 850 GeV, while the high H_T selection is most sensitive for higher values of m_0. The combined exclusion curve shows the contour of the best of the limits. This exclusion curve can be found in Fig. 8.3.

Comparison with other analyses

In Fig. 8.4 all limits in the cMSSM plane from the CMS experiment are shown. The analysis presented in this thesis labeled with Jets+MHT has the best limits.

[1] CL_{S+B} would by definition exclude in 5% of the searches a signal with zero strength

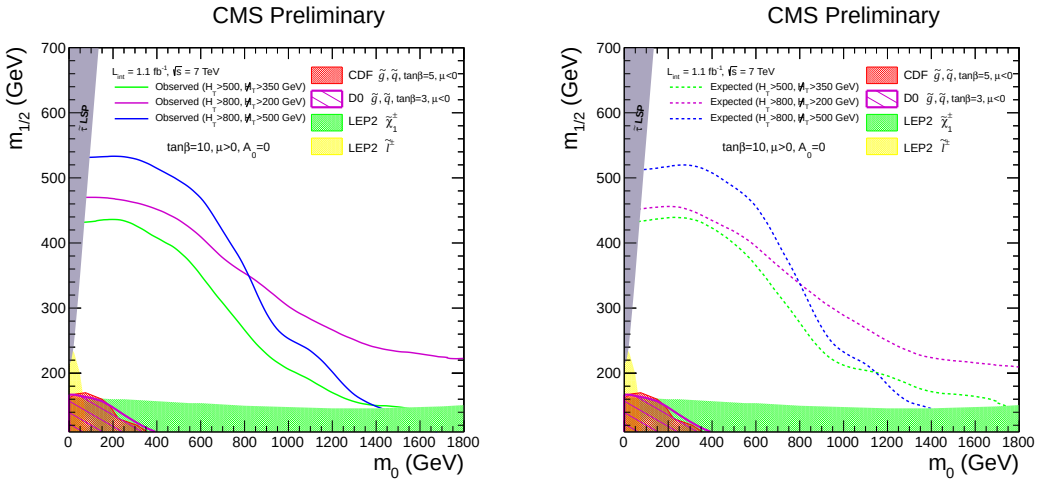

Figure 8.2: Observed (left) and expected (right) limits for the evolved selections medium H_T & $\not\!\!H_T$ (green), high H_T (purple) and high $\not\!\!H_T$ (blue) in the m_0-$m_{1/2}$-plane for $1.14 fb^{-1}$.

For low values of m_0 up to about 400 GeV the limit is rather flat at about $m_{1/2} = 530$ GeV. For higher values of m_0 the limit in $m_{1/2}$ drops with a similar shape as the line of a constant squark mass. Except for very high values of m_0 the hadronic searches dominate the limits. One other hadronic analysis is the analysis labeled α_T [66] that also includes dijet events and relies heavily on the variable α_T to suppress QCD events. This variable uses the fact that QCD-jets are usually back-to-back, while this is usually not true for the two leading jets in events with real $\not\!\!E_T$. A further hadronic analysis is labeled $MT2$ [67] that is based on the transverse mass variable. Like in the analysis presented here two search regions are optimised for sensitivity at low and high values of m_0, respectively. Another analysis called the "Razor"-analysis [68] was made public well after this analysis and is therefore not included in Fig. 8.4. It only predicts the shape of the contributing SM backgrounds and fits the scale of these backgrounds to best fit the data in a region where only little signal is expected. This analysis uses hadronic as well as leptonic search regions and is therefore more sensitive at very high values of m_0.

The analysis presented here also shows superior results in comparison with

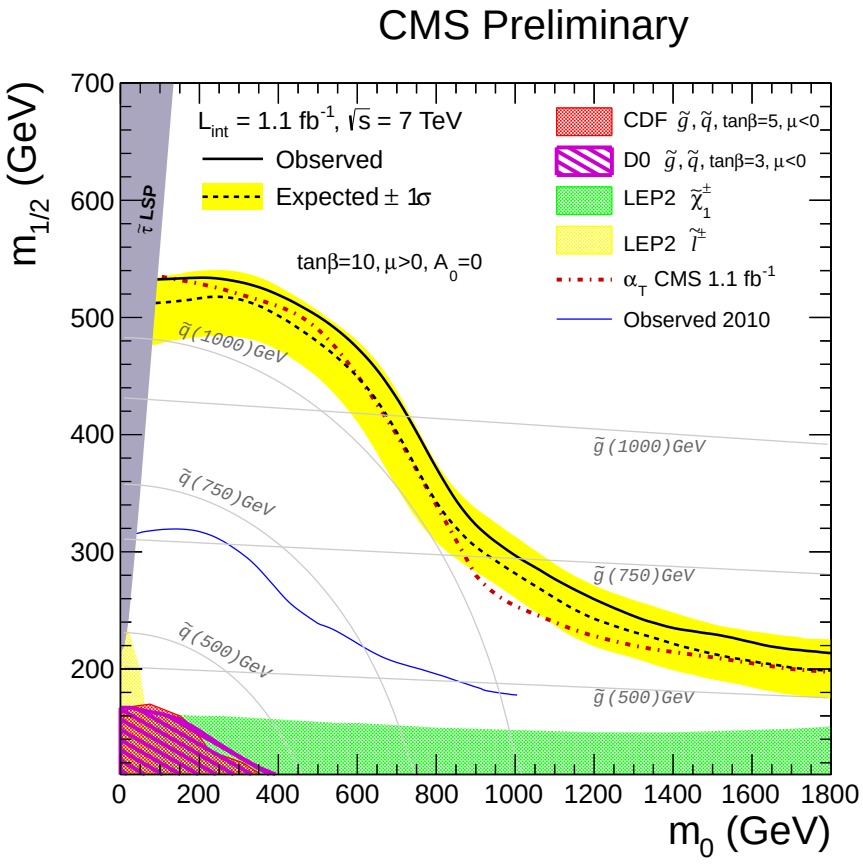

Figure 8.3: Observed and expected limit with 1 sigma uncertainty band in the m_0-$m_{1/2}$-plane for $1.14 fb^{-1}$. The best limit of the different selections is used.

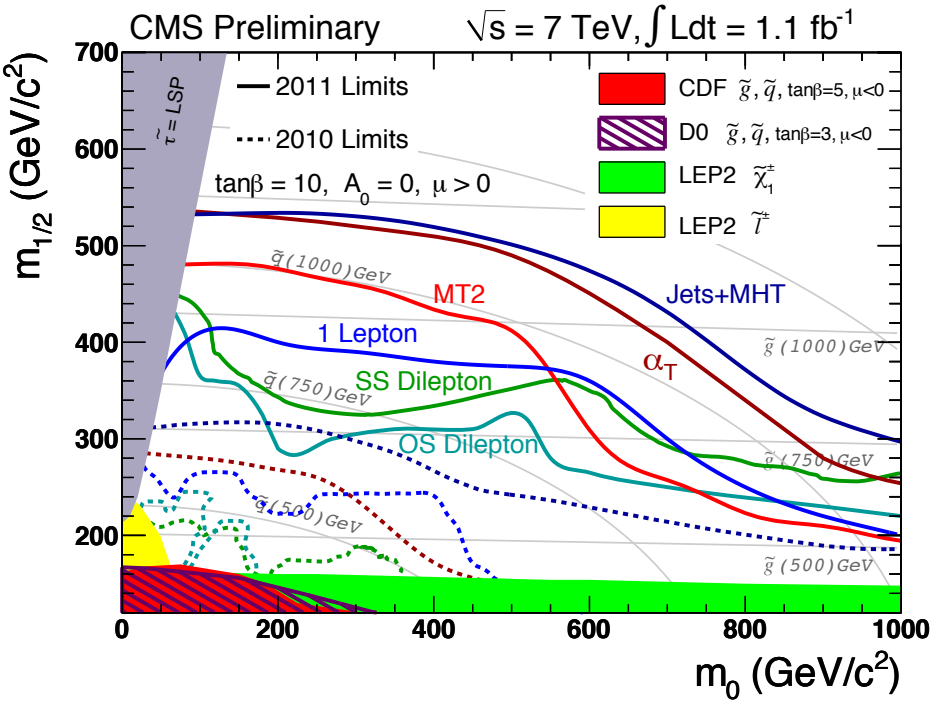

Figure 8.4: Comparison between all the limits set on the cMSSM parameter space by the different CMS analysis.

the ATLAS limits making it the most constraining direct analysis on the cMSSM when made public. The intense work on data-driven background estimates results in an increased sensitivity. In this context it should be reminded that this analysis is rather model independent and the competitiveness of the analysis was not obvious at the beginning.

8.2 Combining the Search Regions

As described above, the best limit of several selections was used for the total limit setting. This can bias the limit towards higher values because from two selections with the same sensitivity the one where the measured data fluctuated towards lower events would be taken. The effect of picking up statistical fluctuations in data becomes larger if more search regions are added. The biggest disadvantage,however, is that two selections that might be quite different, but

Background	(H_T >800 GeV) (350 GeV<$\not{H}_T$ <500 GeV)	(500 GeV<H_T <800 GeV) ($\not{H}_T$ >500 GeV)	(H_T >800 GeV) ($\not{H}_T$ >500 GeV)
$Z \to \nu\bar{\nu}$	$4.71 \pm 1.61 \pm 0.91$	$6.05 \pm 1.62 \pm 1.32$	$2.23 \pm 1.02 \pm 0.47$
$t\bar{t}/W \to e,\mu$+X	$2.10 \pm 1.22^{+0.23}_{-0.24}$	$1.67 \pm 1.19^{+0.19}_{-0.20}$	$0.73 \pm 0.73 \pm 0.08$
$t\bar{t}/W \to \tau_{\mathrm{hadr}}$+X	$2.37 \pm 0.70 \pm 0.15$	$3.49 \pm 0.82 \pm 0.78$	$0.68 \pm 0.68 \pm 0.04$
QCD	$1.00\ ^{+1.11\ +0.45}_{-1.00\ -0.37}$	$0.00\ ^{+0.03\ +0.01}_{-0\ \ -0}$	$0.08\ ^{+0.30\ +0.05}_{-0.08\ -0.04}$
Total background	10.17 ± 2.63	11.21 ± 2.67	3.66 ± 1.54
Observed in data	8	8	3

Table 8.1: Predicted event yields for different background processes for exclusive regions. The first uncertainty given is statistical, the second is the systematic uncertainty. The data and background prediction correspond to $1.06 fb^{-1}$.

yield a similar confidence level at some parameter regions, are not combined to give an improved confidence level. Therefore, a proper combination of different search regions is wanted and studied here for application in future analyses.

The search regions discussed so far are overlapping, i.e. events that enter one selection can also enter another selection. These selections cannot be combined in a straightforward way as this would lead to a double counting of some regions leading to a limit that is too stringent. To avoid this problem exclusive regions are defined and thus made statistically independent. The data yield of these search regions together with the background predictions from the background estimation methods described in the last chapter are summarised in Tab. 8.1. Note that not for all background estimation methods a prediction with $1.14 fb^{-1}$ was available for the exclusive regions. Therefore the data and background predictions in this table correspond to only $1.06 fb^{-1}$. The statistical uncertainties on the QCD prediction is large relative to the predicted value, but as the QCD background is small for these regions, the influence on the total uncertainty is small.

In contrast to the published result discussed above, the total background in each region is taken as the sum of the individual background predictions here and in future updates of the analysis [69]. The effect on the limit is very small. However, especially in search regions with little predicted background and large relative uncertainties the prediction can be shifted towards higher values by taking

the uncertainties into account. An overestimated uncertainty can therefore lead to a larger predicted background and improve the limit.

To combine the different exclusive regions the likelihood used in Eq. 8.1 can simply be multiplied for the different channels [62]. However, care has to be taken about the correlation of the uncertainties. The systematic uncertainties of the background predicted by one method is taken to be fully correlated between the different channels. This is done by using the same value for the nuisance parameter in all channels. The statistical uncertainties and the systematic uncertainties between different background estimation methods are uncorrelated. Therefore, several nuisance parameter have to be introduced; one for each background estimation method, one for each channel to account for the statistical uncertainty within these methods and - as in the standard case - one for each signal uncertainty.

The resulting limit can be seen in Fig. 8.5. Since for the high m_0 or high $m_{1/2}$ region one search region is much more sensitive than the others, no strong improvement is expected, and in fact only very little difference due to the combination of the exclusive regions can be seen close to the borders of the signal scan. The slight decrease in sensitivity for the combined observed limit at low m_0 is due to the smaller luminosity used for the exclusive search regions, while the data yield is the same in the high $\not{H}_T$ selection. The larger difference between the standard result and the result using the combination for high m_0, that is also visible in the expected limit, is due to the missing search region of high H_T and low $\not{H}_T$ [1]. In the region around medium m_0, however, where several search regions yield similar sensitivity, an improvement of up to 40 GeV in $m_{1/2}$ can be observed due to the combination of the exclusive regions in the observed and the expected limit.

Apart from this increase in sensitivity this combination introduces no bias, and defining search regions is much easier. With the previous method few search regions have to be defined that are most sensitive, without looking at the data to not bias the result. An non-optimal choice would lead to a severe drop in sensitivity. With the combination method many regions can be defined and combined.

[1] The search region of $H_T > 800$ GeV and 200 GeV $< \not{H}_T <$ 350 GeV could not be included as the background prediction was not available for all background prediction methods.

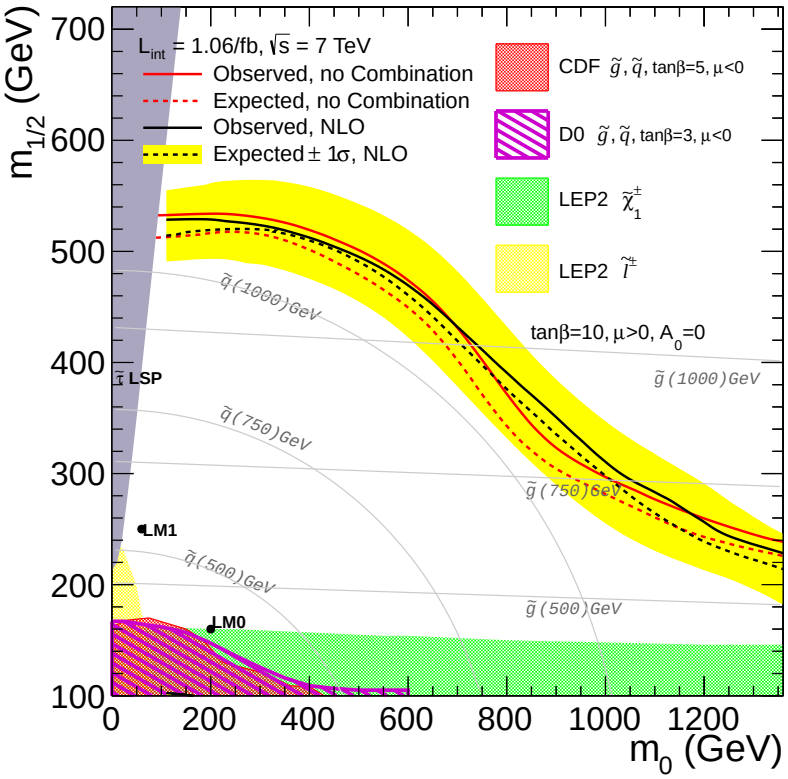

Figure 8.5: Limits on the cMSSM from this analysis, including the combination of several exclusive search regions. The limit set without combination uses $1.14 fb^{-1}$ of data, while the combined limit uses only $1.06 fb^{-1}$.

Insensitive regions simply do not add much information and the limit remains unchanged.

With the use of IsaPythia with ISAJET [70] version 7.71 the masses of the SUSY particles have been calculated within the cMSSM. Fig. 8.6 shows the same limit in the squark-gluino plane. The squark mass corresponds to the mean of the squark masses of the first two generations, that are nearly mass-degenerated. Squark masses of the third generation might, however, be smaller. The very narrow band close to the region where there is no cMSSM solution is the region where the stau is the LSP. As there is no simulation available in this region and

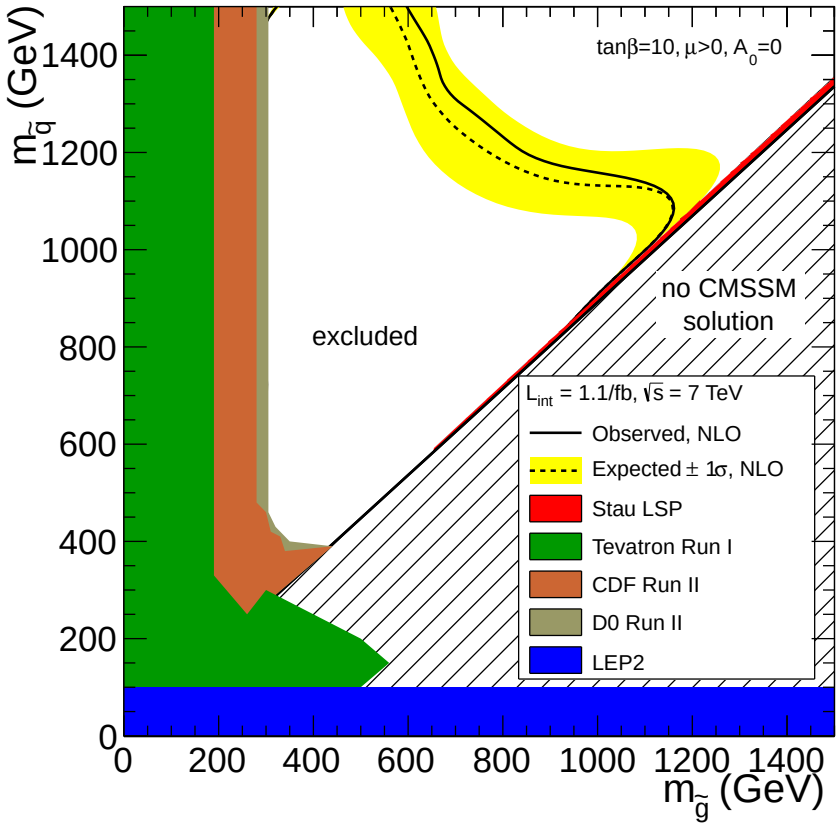

Figure 8.6: Limits on the cMSSM from this analysis, including the combination of several exclusive search regions in the squark-gluino plane.

this analysis is not targeted at this region, this region remains allowed. However, as discussed in Ch. 3 the LSP would not be a dark matter candidate anymore. Except for this region, squark masses of the first two generations can be excluded in the cMSSM up to about 1050 GeV.

8.3 Results with the Full 2011 Dataset

While this thesis was written more data has been recorded and analysed. The full dataset taken by CMS in 2011 corresponds to an integrated luminosity of

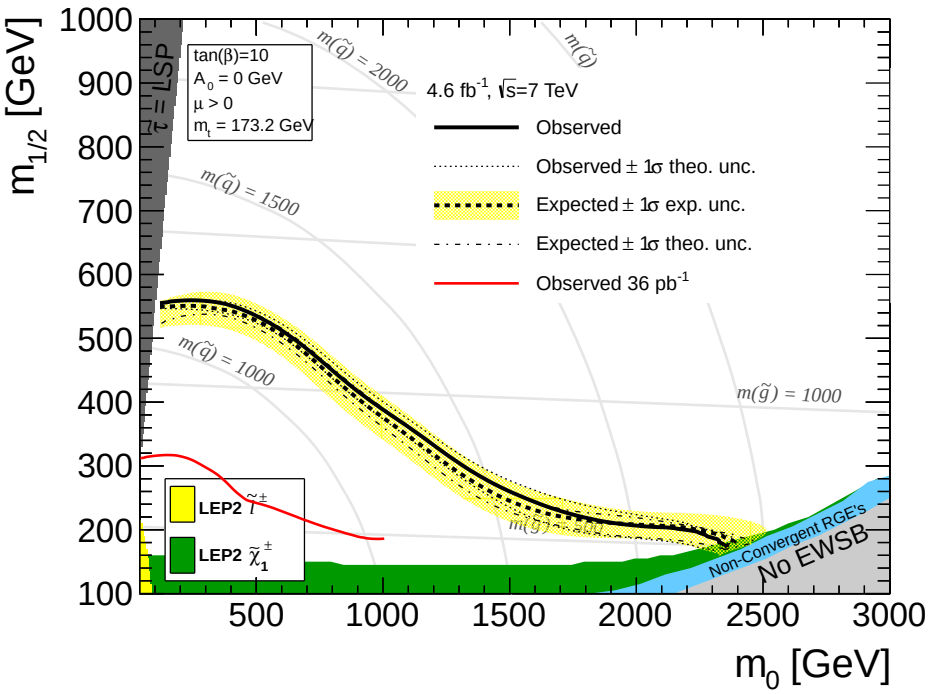

Figure 8.7: Limits on the cMSSM with the combination of several exclusive search regions on $4.65 fb^{-1}$.

$4.65 fb^{-1}$. For the interpretation of this data the combination of several search regions discussed above has been applied, using 14 exclusive bins. Apart from this, the most important change was the increased H_T cut to 500 GeV for the baseline selection due to increased trigger thresholds. The analysis of the full 2011 dataset will be made public soon [69]. The update of the "lost lepton" method to the full 2011 dataset will be described in full detail in [71]. Apart from updated MC studies with higher statistics the main difference is the use of reconstruction efficiencies from simulation. While this increases the dependence on the simulation it allows for a better treatment of the kinematical differences between the $t\bar{t}$, W + jet and Z-sample.

The limits that can be set with this dataset are shown in Fig. 8.7 in the $m_0/m_{1/2}$ mass plane and in Fig. 8.8 in the m_{squark}/m_{gluino} mass plane. While the limit has improved significantly, the gain in sensitivity is not nearly as large as between the analysis described in this thesis and the analysis using $36 pb^{-1}$ of

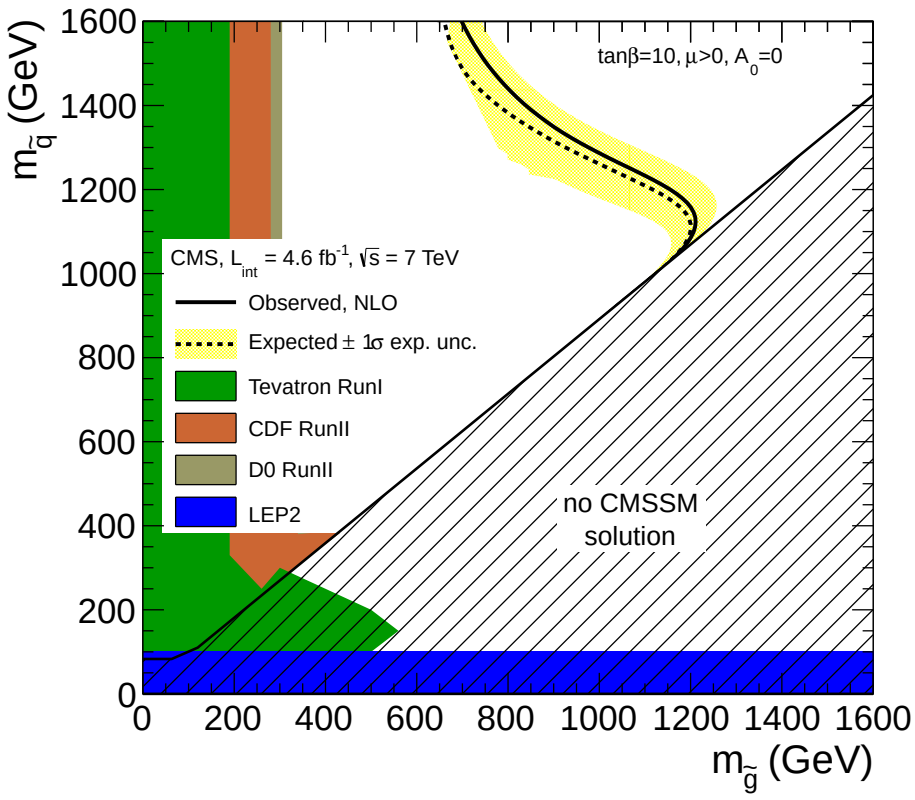

Figure 8.8: Limits on the cMSSM with the combination of several exclusive search regions on $4.65 fb^{-1}$ in the squark/gluino mass plain.

data. Squark masses of the first two generations below about 1100 GeV can be excluded.

9

Conclusion

Motivated by the observation of dark matter and theoretical predictions for SUSY discussed in chapter 3, an all-hadronic search based on jets and $\not{H}_T$ for new physics has been performed on $1.14 fb^{-1}$ and $4.65 fb^{-1}$ of data recorded by the CMS experiment using proton-proton collisions at $\sqrt{s} = 7$ TeV. While the search is rather generic due to the signature of large $\not{H}_T$, the focus is set on a SUSY search and an interpretation within the mSUGRA framework. The lepton veto in this analysis is introduced to reduce the $t\bar{t}$ and W + jet background. The most striking feature of the analysis is the large amount of effort put into data driven background estimation methods that allow for a determination of the expected Standard Model background with high precision. A large part of this thesis documents the prediction of the $t\bar{t}$ and W + jet background where the lepton from the W decay is not reconstructed, not isolated or out of detector acceptance. A control sample is constructed close in phase space to the search region of the analysis, but with exactly one muon. This control sample is re-weighted using reconstruction, isolation and acceptance efficiencies for the muon and the electron to predict the background to signal events. The reconstruction and isolation efficiencies for leptons are determined using the "tag & probe"-method on the Z-resonance. Possible signal contamination in the control sample is removed using the combined transverse mass from the muon and the $\not{E}_T$.

In combination with background predictions for QCD, $Z \to \nu\nu$ and the remaining $t\bar{t}$ and W + jet background due to hadronically decaying taus, control of the $\not{H}_T$ tails is demonstrated for a final hadronic analysis.

As no excess over the predicted SM background has been observed, limits are set on the mSUGRA parameter space. The limits calculated with the CL_S method rule out a large, previously unexplored area of the parameter space, setting a lower limit on the squark masses of the first two generations of 1050 GeV for $\tan\beta = 10$ and $A_0 = 0$ already with $1.14 fb^{-1}$ of data. This is the world-wide most sensitive result in the cMSSM made public in summer of 2011. With the full integrated luminosity of $4.65 fb^{-1}$ the limit improves to about 1100 GeV.

As discussed in section 3.2, rather light SUSY particles are favoured due to the corrections to the higgs mass, the dark matter density and the running of the coupling constants. With the limits set from the analysis discussed in this thesis the impression might arise that a large part of the most favoured parameter region of SUSY is already excluded. However, it should be noted that the cMSSM discussed here is a heavily contraint SUSY model and direct limits on the left- and right-handed stop are only at around 260 GeV and 190 GeV, respectively [72]. Even within the cMSSM there are many very interesting non-excluded regions, where the dark matter density can be accounted for by enhanced annihilation processes of the LSP [73]. SUSY is therefore far from being excluded and the search continues.

Especially with the planned increase in the center of mass energy in 2014, further regions of the parameter space can be probed as the cross-section for heavy particles increases much stronger with energy than the standard model background.

To account for the stringent limits set so far, future SUSY searches should be interpreted also in more general frameworks than the cMSSM. The analysis discussed above is already being interpreted with more general, simplified models [74].

Appendix A

Additional Tests of the Method on Simulated Events

In this part of the appendix additional closure plots as defined in chapter 7.4.1 are shown. First the closure of leptons out of acceptance A.1 is shown. The remainder of the plots are the closure pots as shown in the thesis seperated for $t\bar{t}$ and W + jet.

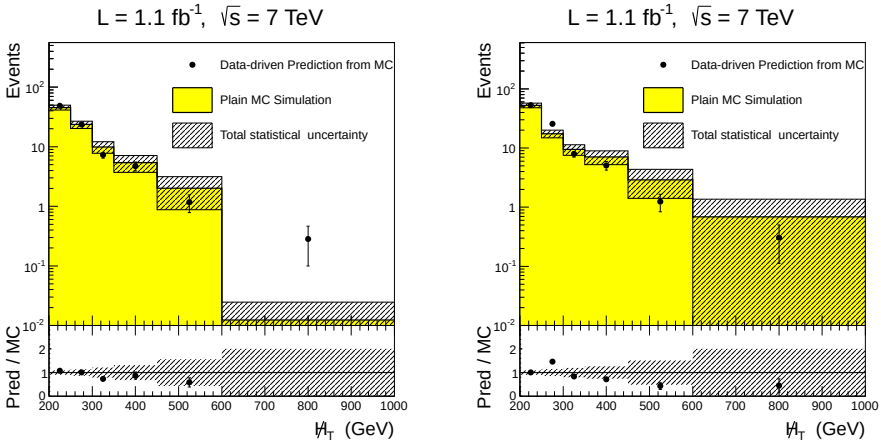

Figure A.1: Comparison of the kinematic properties of the plain MC simulation and the prediction on the same sample of leptons out of detector acceptance, for muons (left) and electrons (right). Schown is the $\not\!\!E_T$ distribution, where the largest dependence is expected as it is correlated with the boost of the W-boson and the lepton p_T

A. ADDITIONAL TESTS OF THE METHOD ON SIMULATED EVENTS

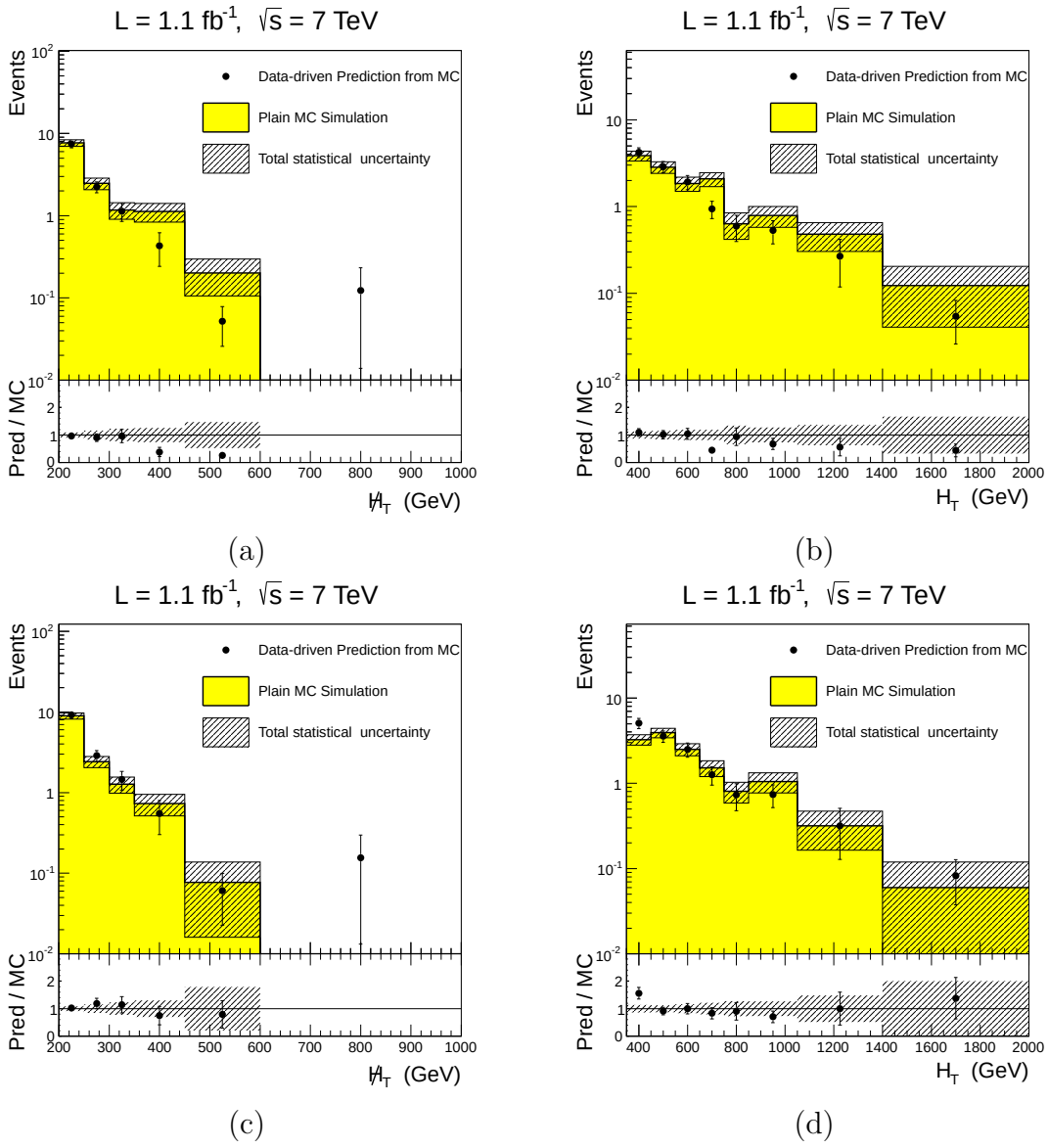

Figure A.2: Comparison of the kinematic properties of the plain $t\bar{t}$ MC simulation and the prediction on the same sample of identified but non-isolated leptons, for electrons (upper two plots) and muons (lower two plots). The shown variables are MHT (left) and HT(right)

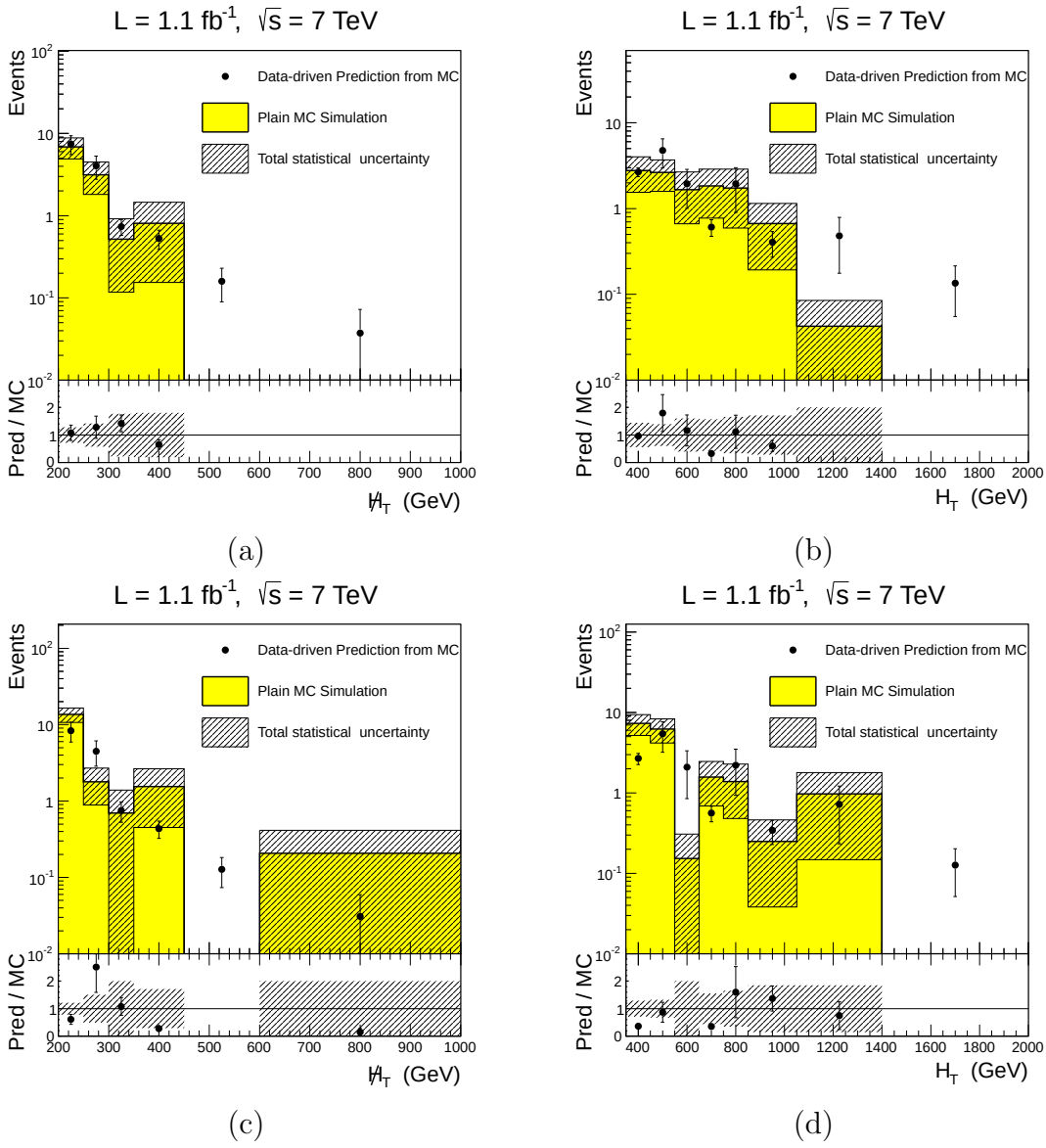

Figure A.3: Comparison of the kinematic properties of the plain W + jet MC simulation and the prediction on the same sample of identified but non-isolated leptons, for electrons (upper two plots) and muons (lower two plots). The shown variables are MHT (left) and HT(right)

A. ADDITIONAL TESTS OF THE METHOD ON SIMULATED EVENTS

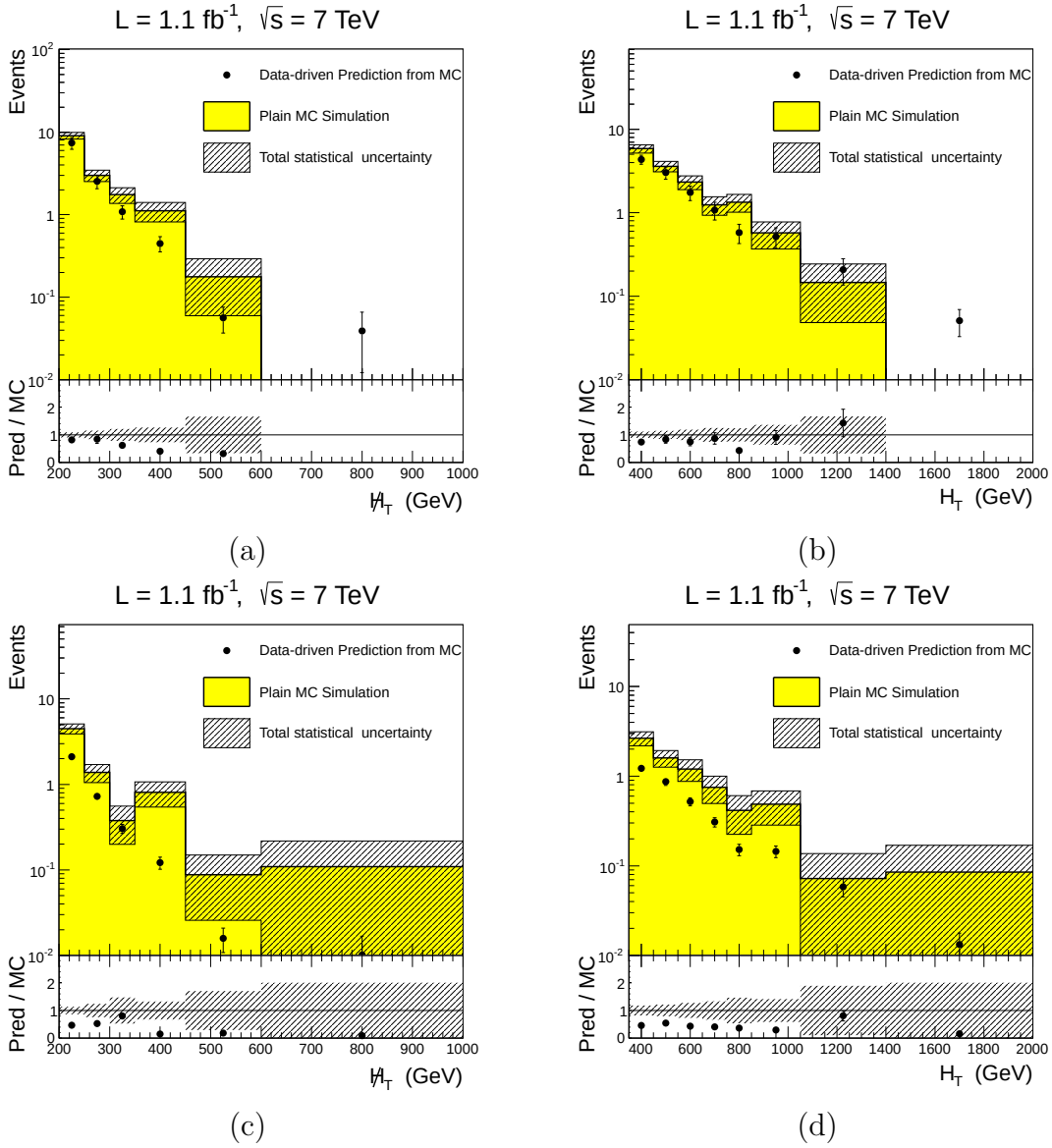

Figure A.4: Comparison of the kinematic properties of the plain $t\bar{t}$ MC simulation and the prediction on the same sample of non-identified leptons in detector acceptance, for electrons (upper two plots) and muons (lower two plots). The shown variables are MHT (left) and HT(right). The difference in scale will be corrected for.

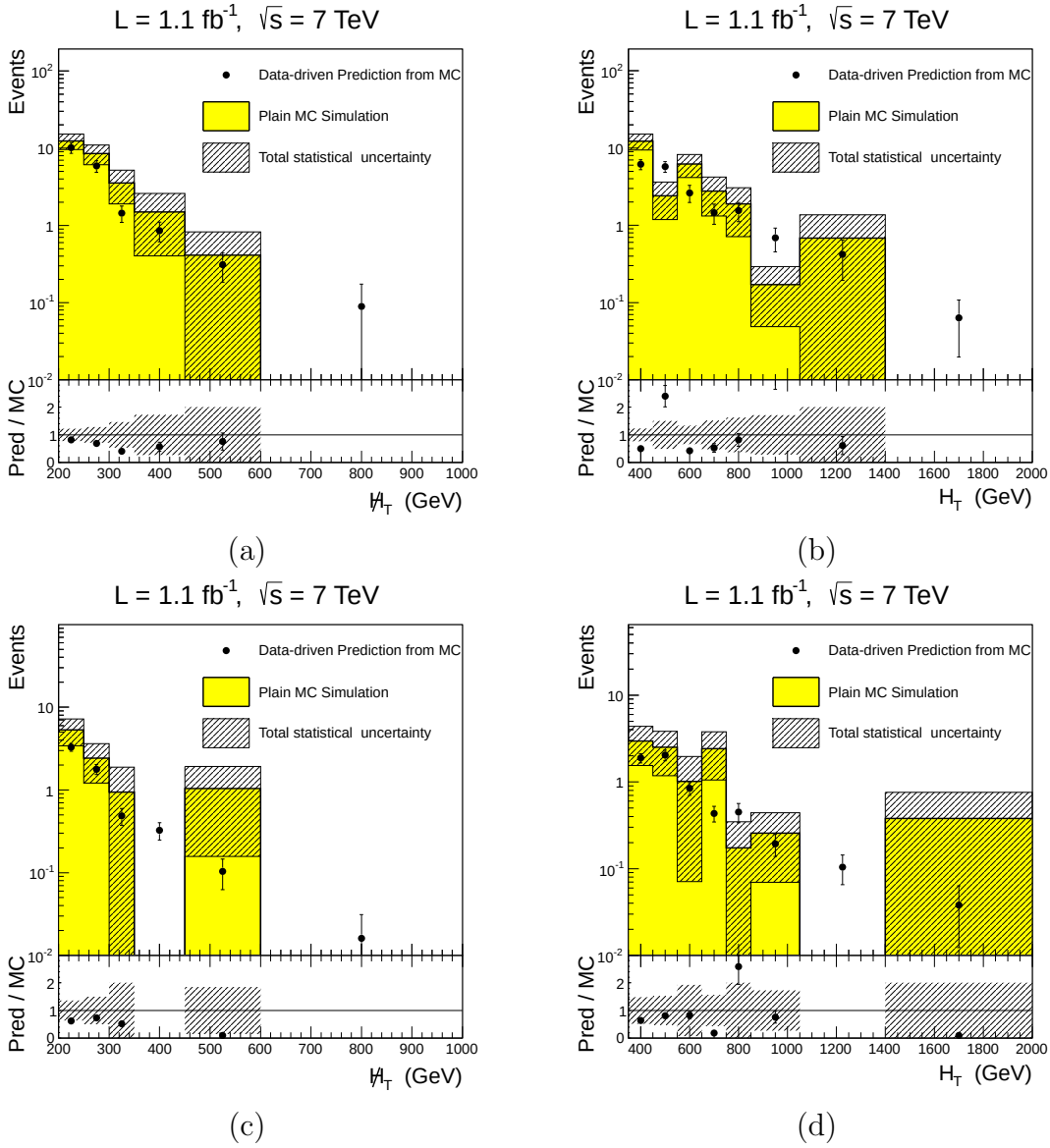

Figure A.5: Comparison of the kinematic properties of the plain W + jet MC simulation and the prediction on the same sample of non-identified leptons in detector acceptance, for electrons (upper two plots) and muons (lower two plots). The shown variables are MHT (left) and HT(right). The difference in scale will be corrected for.

A. ADDITIONAL TESTS OF THE METHOD ON SIMULATED EVENTS

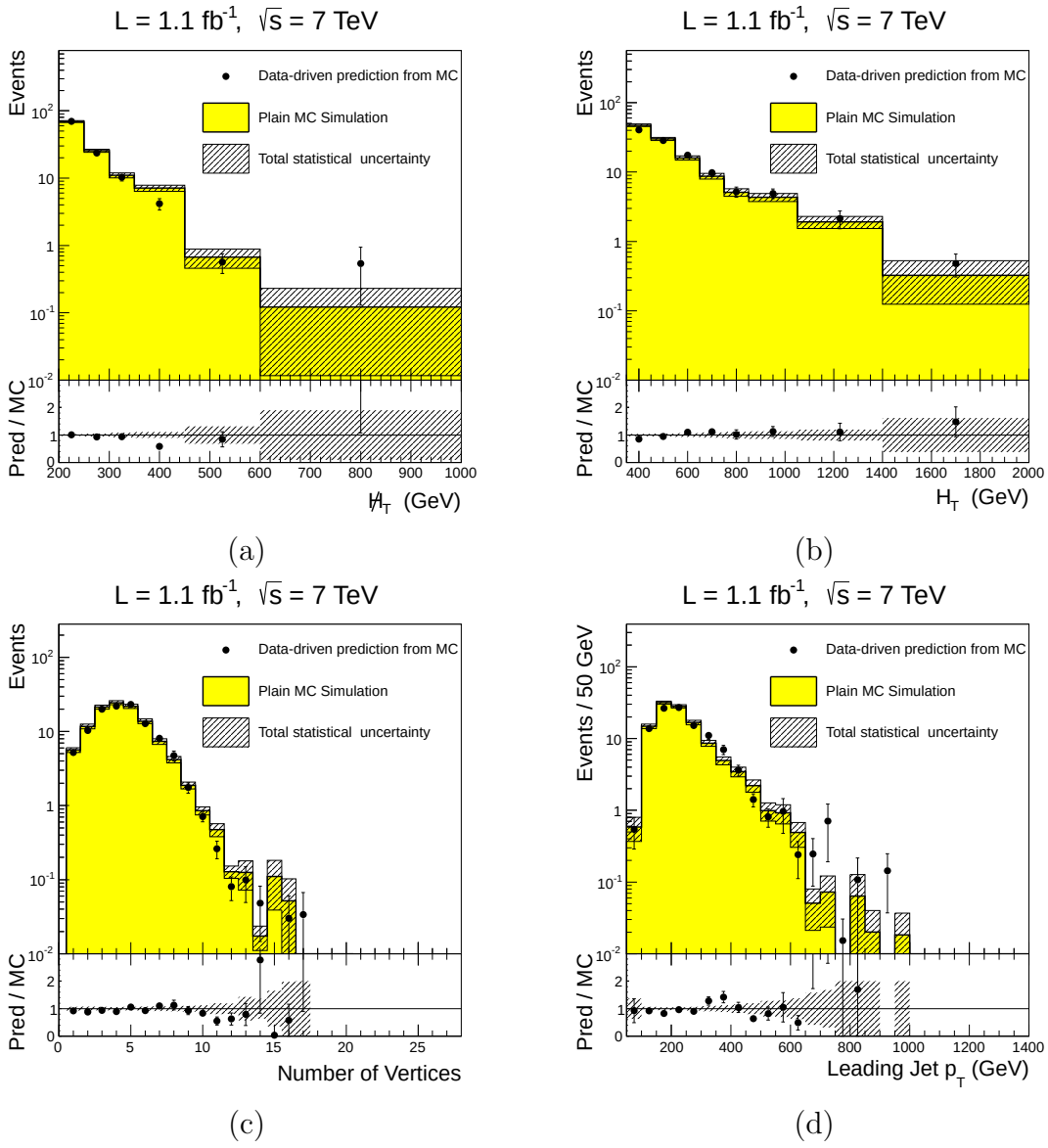

Figure A.6: Closure test of the method. The total background prediction without scale correction on $t\bar{t}$ MC samples is compared to the plain MC simulation for the same samples. using the muon control sample only The shown variables are: MHT (a), HT (b), number of primary vertices (c) and the leading jet p_T (d).

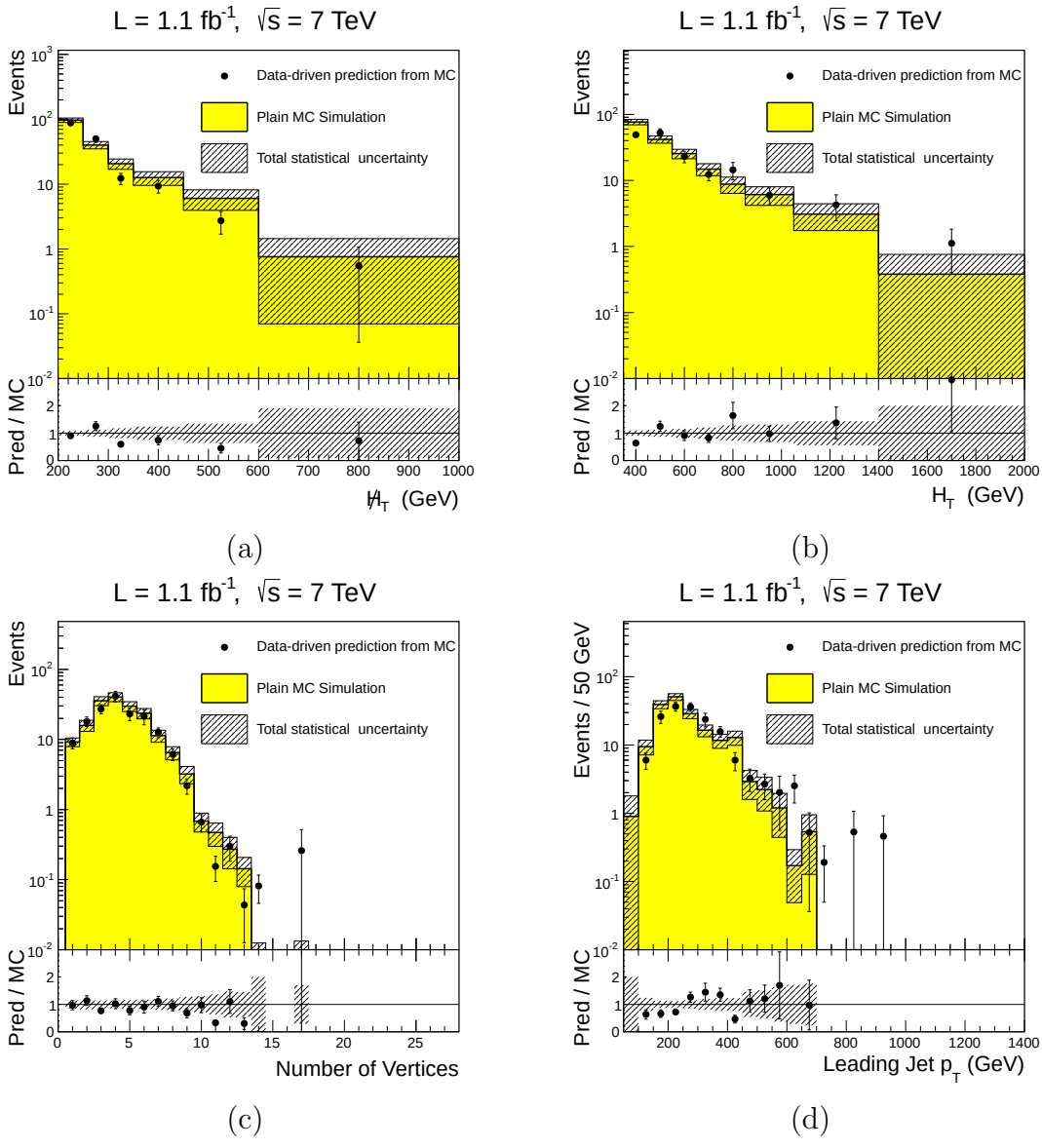

Figure A.7: Closure test of the method. The total background prediction without scale correction on W + jet MC samples is compared to the plain MC simulation for the same samples. using the muon control sample only The shown variables are: MHT (a), HT (b), number of primary vertices (c) and the leading jet p_T (d).

A. ADDITIONAL TESTS OF THE METHOD ON SIMULATED EVENTS

Appendix B

Additional Information for Limit Setting

In this part of the appendix additional information used for limit setting such signal acceptance B.1 and relative signal uncertainties B.2 B.3 are are shown for the cMSSM.

As discussed in the thesis some parameter points are not simulated. These point are excluded from the limit setting and left blank here. However, there are no large regions of not simulated parameter points close to the limit. Calculations used for the limit with the full 2011 dataset use an extended scan that is much more complete.

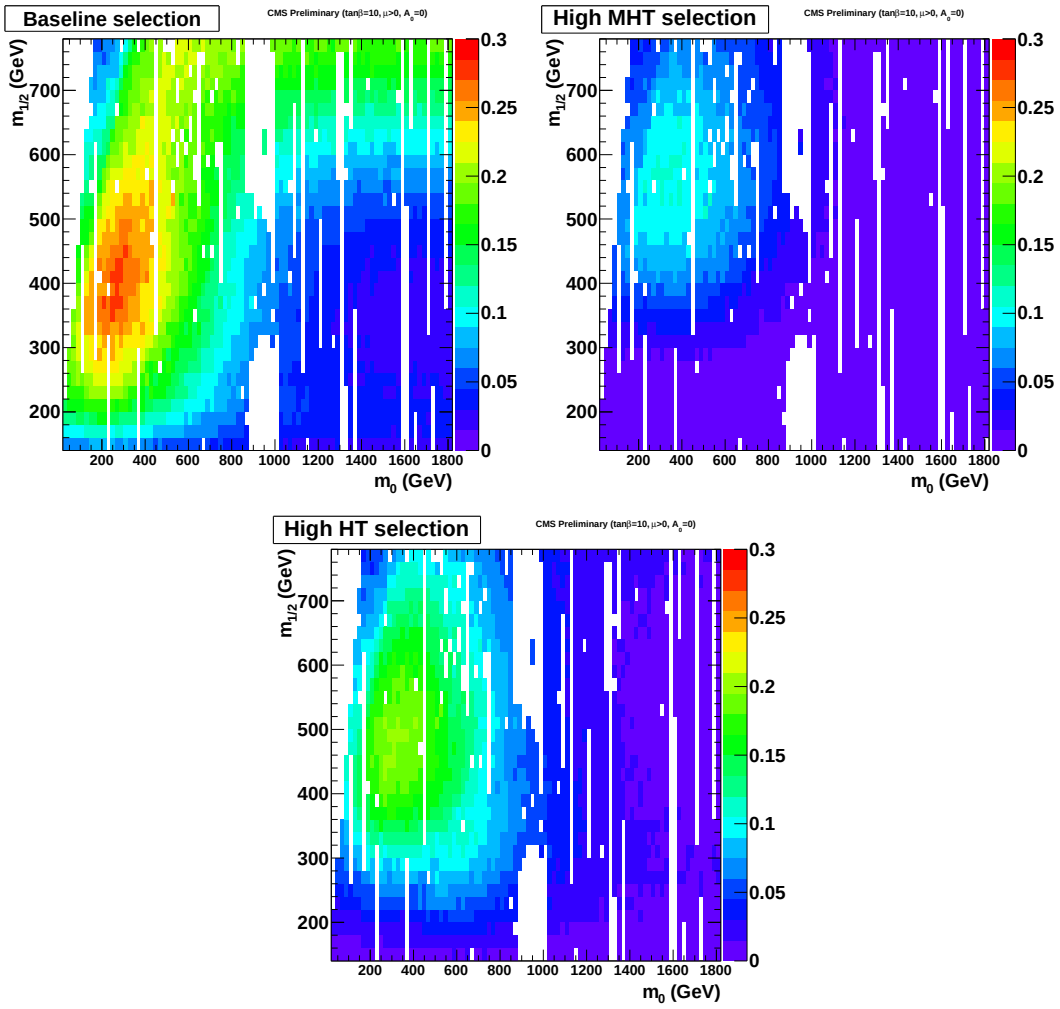

Figure B.1: The plots show the ratio of signal events passing the the baseline selection (top left), the high $\not{H}_T$ selection (top right) and the high H_T selection (bottom). There is no simulation available for the white regions.

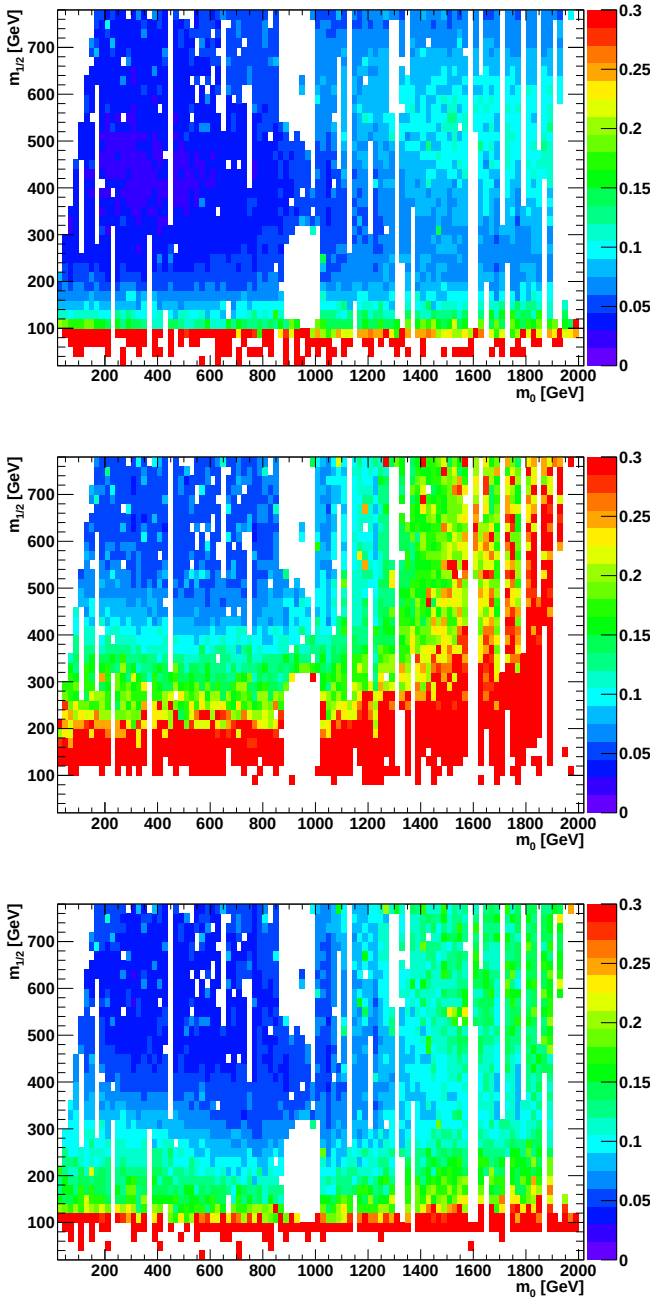

Figure B.2: Relative signal uncertainty for the baseline selection (top left), the high $\not{H}_T$ selection (top right) and the high H_T selection (bottom). This uncertainty is a combination of the jet energy scale, jet energy resolution, PDF and statistics as shown in Fig. B.3 There is no simulation available for the white regions.

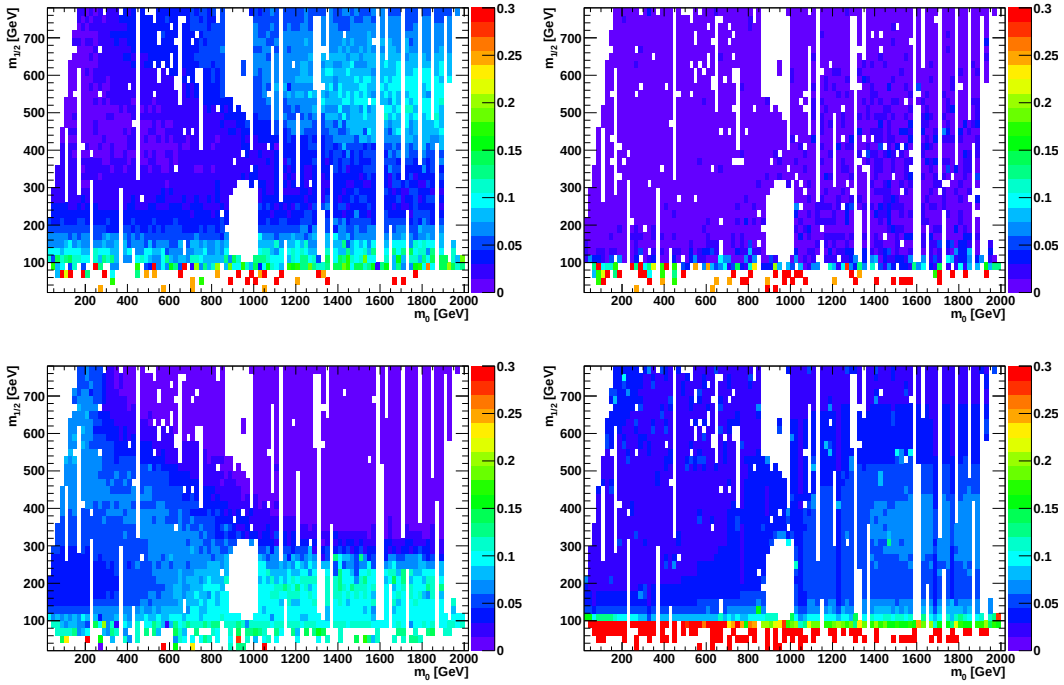

Figure B.3: Seperated parts of the relative signal uncertainty for the baseline selection. Uncertainties due to jet energy scale (top left), jet energy resolution (top right), signal acceptance due to parton distribution funcions (bottom left) and statistics (bottom right) are shown. There is no simulation available for the white regions.

List of Figures

List of Tables

Acknowledgements

First of all I want to thank Prof. Peter Schleper for giving me the opportunity to work in this very friendly and helpful group at Hamburg University. He allowed me to follow my interests in the huge field of particle physics and I always enjoyed the inspiring discussions with him.

Special thanks goes to my supervisor, Christian Autermann, for the many fruitful discussions and for proof-reading this thesis.

I also want to thank the whole group of Hamburg University, especially Chistian Sander, not only for the friendly way they helped in all aspects of my work, but also for all the poker and badminton rounds, that show how good the atmosphere in the group really is.

Finally and most importantly, I want to thank my family, especially my parents Frauke and Detlef, that have supported me in every possible way.

References

[1] *LEP design report*. CERN, Geneva, 1984. Copies shelved as reports in LEP, PS and SPS libraries. 1, 5, 31

[2] E. . Bruning *et al.*, "LHC design report. Vol. I: The LHC main ring,". CERN-2004-003-V-1. 1, 5, 31

[3] "ATLAS: Detector and physics performance technical design report. Volume 1,". 1, 31

[4] **CMS** Collaboration, "The CMS experiment at the CERN LHC," *JINST* **0803** (2008) S08004. 1, 31, 32, 33, 34, 35

[5] V. C. Rubin, W. K. J. Ford, and N. Thonnard, "Rotational properties of 21 SC galaxies with a large range of luminosities and radii, from NGC 4605 R = 4kpc to UGC 2885 R = 122 kpc," *The Astrophysical Journal Letters* **238** (June, 1980) 471–487. 1, 15

[6] D. Clowe, M. Bradac, A. H. Gonzalez, M. Markevitch, S. W. Randall, C. Jones, and D. Zaritsky, "A Direct Empirical Proof of the Existence of Dark Matter," *The Astrophysical Journal Letters* **648** no. 2, (2006) L109. `http://stacks.iop.org/1538-4357/648/i=2/a=L109`. 1, 15

[7] R. R. Wilson, "The Tevatron," *Phys.Today 30N10:23-30* (1977) . 5

[8] C. Burgess and G. D. Moore, *The Standard Model: A Primer*. Cambridge Univ. Press, 2007. 5

[9] W.B.Rolnick, *The fundamental Particles and their Interactions*. Addison-Wesley Publishing Company, 1994. 5

[10] L. H. Ryder, *Quantum Fiel Theory*. Cambridge Univ. Press, 1996. 5

[11] J. Thomsen, "Search for Supersymmetric Particles based on large Missing Transverse Energy and High Pt Jets at the CMS Experiment," *Diploma Thesis* (2007) . 5, 17

[12] S. N. e. a. Ahmed, "Constraints on Nucleon Decay via Invisible Modes from the Sudbury Neutrino Observatory," *Physical Review Letters* **92** no. 10, (Mar., 2004) 102004–+, `arXiv:hep-ex/0310030`. 6, 18

[13] E. Noether, "Invariante Variationsprobleme," *Nachr. d. König. Gesellsch. d. Wiss. zu Gø"ttingen* **Math.-phys. Klasse:235-257** (1928) . 7

[14] C. S. Wu, E. Ambler, R. W. Hayward, D. D. Hoppes, and R. P. Hudson, "Experimental Test of Parity Conservation in Beta Decay," *Physical Review* **105** (Feb., 1957) 1413–1415. 9

[15] P. E. AL., "Review of Particle Physics," *Physics Letters B* **667** (Sept., 2008) 1–6. 10

[16] Z. Bern, G. Diana, L. Dixon, F. Febres Cordero, D. Forde, *et al.*, "Left-Handed W Bosons at the LHC," *Phys.Rev.* **D84** (2011) 034008, `arXiv:1103.5445 [hep-ph]`. 11, 79

[17] **UA1** Collaboration *Physics Letters* **122B, 103, 126B, 398** (1983) . 12

[18] **CMS** Collaboration, S. Chatrchyan *et al.*, "Combined results of searches for the standard model Higgs boson in pp collisions at $\sqrt{(}s) = 7$ TeV," `arXiv:1202.1488 [hep-ex]`. 12

[19] M. Maltoni, T. Schwetz, M. Tórtola, and J. W. F. Valle, "Status of global fits to neutrino oscillations," *New Journal of Physics* **6** (Sept., 2004) 122–+, `arXiv:hep-ph/0405172`. 15

[20] "Lecture on Higgs Physics," *http://theory.physics.helsinki.fi/h̃iggsphys/* (2009) . 15

[21] S. P. Martin, "A Supersymmetry Primer," *arXiv:hep-ph/9709356v6* (2011) . 15, 17, 20, 23, 26, 30

[22] H. Baer and X. Tata, *Weak Scale Supersymmetry*. ISBN: 9780521857864, 2006. 17, 21

[23] U. Amaldi, W. de Boer, and H. Furstenau, "Comparison of grand unified theories with electroweak and strong coupling constants measured at LEP," *Phys. Lett.* **B260** (1991) 447–455. 20

[24] **CMS** Collaboration, "CMS Physics Technical Design Report, Volume II: Physics Performance," *Journal of Physics G: Nuclear and Particle Physics* **34** no. 6, (2007) 995. `http://stacks.iop.org/0954-3899/34/i=6/a=S01`. 26, 28

[25] W. de Boer, R. Ehret, and D. I. Kazakov, "Predictions of SUSY masses in the minimal supersymmetric grand unified theory," *Zeitschrift für Physik C Particles and Fields* **67** (1995) 647–664. `http://dx.doi.org/10.1007/BF01553992`. 10.1007/BF01553992. 26

[26] E. Buning, O., E. Collier, P., E. Lebrun, P., E. Myers, S., E. Ostojic, R., *et al.*, "LHC Design Report. 2. The LHC infrastructure and general services,". 31

[27] E. Benedikt, M., E. Collier, P., E. Mertens, V., E. Poole, J., and E. Schindl, K., "LHC Design Report. 3. The LHC injector chain,". 31

[28] "ATLAS: Detector and physics performance technical design report. Volume 2,". 31

[29] **CMS** Collaboration, "Tracking and Primary Vertex Results in First 7 TeV Collisions," *CMS PAS TRK-10-005* . 34

[30] **CMS** Collaboration, "Description and Performance of the CMS Track and Primary Vertex Reconstruction," *CMS AN-11-172* . 34

[31] H. Liu, K. Hatakeyama, U. Gebbert, K. Theofilatos, and W. Flanagan, "Studies on ECAL Dead and Masked Channel Contributions to High MET and MHT," *CMS-AN-10-354* (2010) . 35, 58

[32] **CMS** Collaboration, "Perfgormance of CMS muon reconstruction in pp collisions at $\sqrt{s} = 7$ TeV," *MUO-10-004* . 37

[33] **CMS** Collaboration, *Trigger Tutorial*. https://twiki.cern.ch/twiki/bin/view/CMSPublic/ WorkBookHLTTutorial. 38

[34] **CMS** Collaboration, "Electron Reconstruction in CMS," *CMS Note 2006/40* (2006) . 40

[35] G. Soyez, "The SISCone and anti-kt jet algorithms," `arXiv:0807.0021 [hep-ph]`. 41

[36] **CMS** Collaboration, "Particle Flow Event Reconstruction in CMS and Performance for Jets, Taus, and MET,". 42, 49

[37] **CMS** Collaboration, "Jet Plus Tracks Algorithm for Calorimeter Jet Energy Corrections in CMS," *CMS PASD JME-09-002* (2009) . 43, 47

[38] **CMS** Collaboration, "Jet Energy Corrections determination at 7 TeV,". 44

[39] D. E. and Groom, "Energy flow in a hadronic cascade: Application to hadron calorimetry," *Nuclear Instruments and Methods in Physics Research Section A: Accelerators, Spectrometers, Detectors and Associated Equipment* **572** no. 2, (2007) 633 – 653. `http://www.sciencedirect.com/science/article/pii/S0168900206023965`. 44

[40] D. Lincoln, G. Morrow, and P. Kasper, "A hidden bias in a common calorimeter calibration scheme," *Nuclear Instruments and Methods in Physics Research Section A: Accelerators, Spectrometers, Detectors and Associated Equipment* **345** no. 3, (1994) 449 – 452. `http://www.sciencedirect.com/science/article/pii/0168900294904979`. 45

[41] **CMS** Collaboration, "Determination of jet energy calibration and transverse momentum resolution in CMS," *Journal of Instrumentation* **6** no. 11, (2011) P11002. `http://stacks.iop.org/1748-0221/6/i=11/a=P11002`. 46, 47, 107

[42] V. Blobel, "Large-scale optimization with the limited-memory BFGS program LVMINI,". 46

[43] C. Autermann, C. Sander, P. Schleper, M. Schröder, and H. Stadie, "Measurement of the Full Jet Transverse Momentum Response Function in QCD Di-Jet Events," *CMS-AN-11-330* (2011) . 49, 103

[44] **CMS** Collaboration, "Search for New Physics with Jets and Missing Transverse Momentum in pp collisions at $\sqrt{s} = 7$ TeV," *arXiv:1106.4503v1* (2011) . 51, 54, 68

[45] **CMS** Collaboration, "Search for supersymmetry in all-hadronic events with missing energy,". 51, 99, 106

[46] **CMS** Collaboration, "Electron reconstruction and identification at $\sqrt{s} = 7$ TeV," `EGM-10-004`. 53

[47] RA2Classic, "Inclusive search for new physics at CMS with the jets and missing momentum signature," *CMS Analysis Note* (2011) . 55, 56, 59, 62

[48] R. Bellan, M. D'Alfonso, S. A. Koay, J. F. Low, S. Lowette, R. Rossin, J. Incandela, C. Bernet, and P. Janot, "Tail Investigations for the RA2 Analysis," *CMS-AN-10-383* (2010) . 55, 57, 58

[49] R. Schoefbeck *et al.*, "Fake missing transverse momentum in hadronic and leptonic SUSY searches," `CMS-AN-11-188`. 58

[50] HCAL Noise WG, HB&HE Noise Cleaning for 2011, JetMET meeting, CMS Physics Week, May 16, 2011. 58

[51] **CMS** Collaboration, "Missing transverse energy performance of the CMS detector," `arXiv:1106.5048 [physics.ins-det]`. 58

[52] "Geant4 - a simulation toolkit," *Nucl. Inst. Meth. A* **506** (2003) 250–303. 60

[53] "Geant4 - developments and applications," *IEEE 53* **1** (2006) 270–278. 60

[54] T. Sjöstrand, S. Mrenna, and P. Z. Skands, "PYTHIA 6.4 Physics and Manual; v6.420, tune D6T," *JHEP* **05** (2006) 026, `arXiv:hep-ph/0603175`. 60

[55] J. Alwall *et al.*, "MadGraph/MadEvent v4: The New Web Generation," *JHEP* **09** (2007) 028, `arXiv:0706.2334 [hep-ph]`. 60

[56] R. Bellan, M. D'Alfonso, S. A. Koay, S. Lowette, N. McColl, R. Rossin, and J. Incandela, "Data-Driven Prediction of the Hadronically Decaying Tau Background for the RA2 Inclusive Hadronic SUSY Search," *CMS-AN-10-402* (2010) . 65, 85, 101

[57] R. Bellan, M. D'Alfonso, S. A. Koay, S. Lowette, N. McColl, R. Rossin, and J. Incandela, "Data-driven Prediction with the Rebalance+Smear Method of the QCD Background for the RA2 Inclusive Hadronic SUSY Search," *CMS-AN-10-401* (2010) . 67, 101

[58] T. Schum, C. Autermann, C. Sander, and P. Schleper, "QCD background prediction by factorization for all-hadronic SUSY searches," *CMS-AN-10-204* (2010) . 67, 101

[59] **CMS** Collaboration, "Data-Driven Estimation of the Invisible Z Background to the SUSY MET Plus Jets Search," *CMS Physics Analysis Summary* **SUS-08-002** (2008) . 67, 101

[60] V. H. A. H. K. M. N. Adam, J. Berryhill, "Generic Tag and Probe Tool for Measuring Efficiency at CMS with Early Data," *CERN-CMS-NOTE-2009-111* . 81

[61] W. de Boer, "The Constrained MSSM Revisited," *arXiv:hep-ph/9611394v1* (1996) . 107

[62] A. Read, "Modified Frequentist Analysis of Search Results (The CL_S Method)," *CERN 2000-005* (2000) . 107, 115

[63] M. W.Beenakker, R.Hoepker, "PROSPINO: A Program for the Production of Supersymmetric Particles in Next-to-leading Order QCD," *arXiv:hep-ph/9611232v1* (1996) . 107

[64] "PDF4LHC Recommendations." `http://www.hep.ucl.ac.uk/pdf4lhc/PDF4LHCrecom.pdf`. 108

[65] **CMS** Collaboration, "Absolute Calibration of the CMS Luminosity Measurement: Summer 2011 Update," *CMS PAS EWK-11-001* (2011) . 108

[66] L. Randall and D. Tucker-Smith, "Dijet Searches for Supersymmetry at the LHC," *Phys. Rev. Lett.* **101** (2008) 101803. 111

[67] **CMS** Collaboration, "Search for supersymmetry in all-hadronic events with MT2," *CMS-PAS-SUS-11-005* (2011) . 111

[68] "Kinematical variables towards new dynamics at the LHC," *arXiv:1006.2727v2* (2011) . 111

[69] **CMS** Collaboration, "Search for supersymmetry in all-hadronic events with multijets and missing energy in pp collisions at $\sqrt{s} = 7$ TeV (title not final)," *To be published* (2012) . 114, 118

[70] H. B. X. T. E. Paige, D. Protopopescu, "ISAJET A Monte Carlo Event Generator for pp, $\bar{p}p$ and e^+e^- Reactions,". 116

[71] A. Draeger, "Determination of the $t\bar{t}$ and W+jet background in Searches for Supersymmetry at the CMS Experiment (title not final)," 2012. 118

[72] M. Papucci, J. T. Ruderman, and A. Weiler, "Natural SUSY Endures," `arXiv:1110.6926 [hep-ph]`. 122

[73] J. Ellis, K. A. Olive, and V. C. Spanos, "Galactic-Centre Gamma Rays in CMSSM Dark Matter Scenarios," *JCAP* **1110** (2011) 024, `arXiv:1106.0768 [hep-ph]`. 122

[74] LHC New Physics Working Group, "Simplified Models for LHC New Physics Searches," *(to appear)* **www.lhcnewphysics.org** (2011) . 122